

# Sliding Mode Control of Photovoltaic Energy Conversion Systems

Pradeep Kumar Sahu



Department of Electrical Engineering  
National Institute of Technology Rourkela

# Sliding Mode Control of Photovoltaic Energy Conversion Systems

*Dissertation submitted to the  
National Institute of Technology Rourkela*

*in partial fulfillment of the requirements*

*of the degree of*

***Doctor of Philosophy***

*in*

***Electrical Engineering***

*by*

***Pradeep Kumar Sahu***

(Roll Number: 511EE701)

*under the supervision of*

***Prof. Somnath Maity***



November, 2016

Department of Electrical Engineering  
National Institute of Technology Rourkela



Electrical Engineering  
National Institute of Technology Rourkela

---

November 11, 2016

## Certificate of Examination

Roll Number: *511EE701*

Name: *Pradeep Kumar Sahu*

Title of Dissertation: *Sliding Mode Control of Photovoltaic Energy Conversion Systems*

We the below signed, after checking the dissertation mentioned above and the official record book (s) of the student, hereby state our approval of the dissertation submitted in partial fulfillment of the requirements of the degree of *Doctor of Philosophy in Electrical Engineering* at *National Institute of Technology Rourkela*. We are satisfied with the volume, quality, correctness, and originality of the work.

---

Susovon Samanta  
*Member (DSC)*

---

Somnath Maity  
*Principal Supervisor*

---

Santanu Kumar Behera  
*Member (DSC)*

---

S. P. Singh  
*External Examiner*

---

Anup Kumar Panda  
*Chairman (DSC)*

---

Jitendriya Kumar Satapathy  
*Head of the Department*



Electrical Engineering  
National Institute of Technology Rourkela

---

**Prof. Somnath Maity**

Assistant Professor

November 11, 2016

## Supervisor's Certificate

This is to certify that the work presented in this dissertation entitled *Sliding Mode Control of Photovoltaic Energy Conversion Systems* submitted by *Pradeep Kumar Sahu*, Roll Number- *511EE701*, is a record of original research carried out by him under my supervision and guidance in partial fulfillment of the requirements of the degree of *Doctor of Philosophy in Electrical Engineering*. Neither this dissertation nor any part of it has been submitted for any degree or diploma to any institute or university in India or abroad.

---

Somnath Maity  
Principal Supervisor

*Dedicated  
to  
my late father*

# Declaration of Originality

I, *Pradeep Kumar Sahu*, Roll Number *511EE701* hereby declare that this dissertation entitled *Sliding Mode Control of Photovoltaic Energy Conversion Systems* presents my original work carried out as a doctoral student of NIT Rourkela and, to the best of my knowledge, it contains no material previously published or written by another person, nor any material presented for the award of any other degree or diploma of NIT Rourkela or any other institution. Any contribution made to this research by others, with whom I have worked at NIT Rourkela or elsewhere, is explicitly acknowledged in the dissertation. Works of other authors cited in this dissertation have been duly acknowledged under the sections “Reference” or “Bibliography”. I have also submitted my original research records to the scrutiny committee for evaluation of my dissertation.

I am fully aware that in case of any non-compliance detected in future, the Senate of NIT Rourkela may withdraw the degree awarded to me on the basis of the present dissertation.

November 11, 2016  
NIT Rourkela

*Pradeep Kumar Sahu*

# Acknowledgment

First of all, I would like to express my deep sense of respect and gratitude towards my supervisor Prof. Somnath Maity, who has been the guiding force behind this work. I want to thank him for introducing me to the field of Power Electronics Converter System and giving me the opportunity to work under him. He has been supporting and encouraging my research efforts during all my years at NIT Rourkela. His undivided faith in this topic and ability to bring out the best of analytical and practical skills in people has been invaluable in tough periods. Without his invaluable advice and assistance it would not have been possible for me to complete this thesis. I am greatly indebted to him for his constant encouragement and invaluable advice in every aspect of my research carrier. I consider it my good fortune to have got an opportunity to work with such a wonderful person.

I thank our H.O.D. Prof. J. K. Satpathy for the constant support in my thesis work. I am also grateful to my committee members: Prof. A. K. Panda, Prof. S. Ghosh, Prof. S. Samanta, and Prof. S. K. Behera for their interests, suggestions and kind supports for my research work. They have been great sources of inspiration to me and I thank them from the bottom of my heart.

I would also like to thank all faculty members, all my colleagues in Electrical Engineering Department; Susanta sir, Ashish, Jitendra, Prem, Sanjeet, and Anneya to provide me their regular suggestions and encouragements during the whole work.

At last but not the least, I offer my deepest gratitude to my wife Sandhya for her everlasting love, support, confidence and encouragement for all my endeavors. Without her, I may lose the motivation to work for my future. Finally, my special thanks go to my daughter Purvee for giving me such a joy during the tough times as a Ph.D. student. My family is my eternal source of inspiration in every aspect and every moment in my life.

November 11, 2016  
NIT Rourkela

*Pradeep Kumar Sahu*  
Roll Number: 511EE701

# Abstract

Increasing interest and investment in renewable energy give rise to rapid development of high penetration solar energy. The focus has been on the power electronic converters which are typically used as interface between the dc output of the photovoltaic (PV) panels and the terminals of the ac utility network. In the dual-stage grid-connected PV (GPV) system, the dc-dc stage plays a significant role in converting dc power from PV panel at low voltage to high dc bus voltage. However, the output of solar arrays varies due to change in solar irradiation and weather conditions. More importantly, high initial cost and limited lifespan of PV panels make it more critical to extract as much power from them as possible. It is, therefore, necessary one to employ the maximum power point tracking (MPPT) techniques in order to operate PV array at its maximum power point (MPP). A fast-and-robust analog-MPP tracker is thus proposed by using the concepts of Utkin's equivalent control theory and fast-scale stability analysis. Analytical demonstration has also been presented to show the effectiveness of the proposed MPPT control technique. After the dc stage, the dc-ac inverter stage is employed to convert dc power into ac power and feed the power into the utility grid. The dc-ac stage is realized through the conventional full-bridge voltage source inverter (VSI) topologies. A fixed frequency hysteresis current (FFHC) controller, as well as an ellipsoidal switching surface based sliding mode control (SMC) technique are developed to improve the steady state and dynamic response under sudden load fluctuation. Such a control strategy is used not only maintains good voltage regulation, but also exhibits fast dynamic response under sudden load variation. Moreover, VSI can be synchronized with the ac utility grid. The current injected into the ac grid obeys the regulations standards (IEEE Std 519 and IEEE Std 1547) and fulfills the maximum allowable amount of injected current harmonics. Apart from that, controlling issues of stand-alone and grid-connected operation PV have also been discussed. A typical stand-alone PV system comprises a solar array and battery which is used as a backup source for power management between the source and the load. A control approach is developed for a  $1-\phi$  dual-stage transformerless inverter system to achieve voltage regulation with low steady state error and low total harmonic distortion (THD) and fast transient response under various load disturbances. The SMC technique is employed to address the power quality issues. A control technique for battery charging and discharging is also presented to keep the dc-link voltage constant during change in load demand or source power. This battery controller is employed for bidirectional power flow between battery and dc-link through a buck-boost converter in order to keep the input dc voltage constant. The robust stability of the closed-loop



system is also analyzed. Finally, modeling and control of a  $1-\phi$  dual-stage GPV system has been analyzed. A small-signal average model has been developed for a  $1-\phi$  bridge inverter. The proposed controller has three cascaded control loops. The simulation results and theoretical analysis indicate that the proposed controller improves the efficiency of the system by reducing the THD of the injected current to the grid and increases the robustness of the system against uncertainties.

***Keywords:*** PV system, MPPT, VSI, dual-stage converter topology, SMC, stand-alone and grid-connected operation.

# Contents

<b>Certificate of Examination</b>	<b>ii</b>
<b>Supervisor’s Certificate</b>	<b>iii</b>
<b>Dedication</b>	<b>iv</b>
<b>Declaration of Originality</b>	<b>v</b>
<b>Acknowledgement</b>	<b>vi</b>
<b>Abstract</b>	<b>vii</b>
<b>List of Figures</b>	<b>xii</b>
<b>List of Tables</b>	<b>xvii</b>
<b>1 Introduction</b>	<b>1</b>
1.1 Motivation . . . . .	1
1.2 PV Power System . . . . .	3
1.2.1 Evolution of PV Cell and Module . . . . .	4
1.2.2 Grid-Connected PV System . . . . .	5
1.3 A Brief Introduction to the String-Inverter Topology . . . . .	8
1.4 Existing Inverter Topologies in GPV System . . . . .	9
1.4.1 Power Processing Stages . . . . .	10
1.4.2 Power Decoupling . . . . .	11
1.4.3 Types of Grid Interfacing . . . . .	12
1.4.4 AC PV Module . . . . .	13
1.5 Specification, Demand and Standards for GPV Systems . . . . .	14
1.6 Design Considerations of String-Inverter . . . . .	16
1.7 Objectives of the Research Project . . . . .	17

1.8	Major Contributions and Outline of the Dissertation . . . . .	18
<b>2</b>	<b>DC-DC Power Processing</b>	<b>22</b>
2.1	Mathematical Modeling of PV Cell . . . . .	22
2.2	DC-DC Converter Topologies . . . . .	25
2.3	Reviews on MPP Tracker . . . . .	30
2.4	Module-Integrated Analog MPP Trackers . . . . .	33
2.5	Sliding-Mode Controlled MPVS . . . . .	38
2.5.1	Existence Conditions Under Ideal Switching Surface . . . . .	39
2.5.2	Prediction of Fast-scale Stability Margin . . . . .	42
2.5.3	Design Guidelines . . . . .	45
2.5.4	Equivalent SMC and Dynamics of Equivalent Motion . . . . .	46
2.6	Performance Analysis and Its Experimental Validation . . . . .	48
2.6.1	Realization of ASMC-Based MPPT . . . . .	48
2.6.2	Performance Analysis . . . . .	50
2.7	Conclusion . . . . .	56
<b>3</b>	<b>DC-AC Power Processing</b>	<b>57</b>
3.1	1- $\phi$ Inverter Topologies . . . . .	57
3.2	Modulation Techniques for VSI . . . . .	59
3.2.1	1- $\phi$ Bridge Topology with Bipolar PWM . . . . .	60
3.2.2	1- $\phi$ Bridge Topology with Unipolar PWM . . . . .	61
3.2.3	LC Filter Design for 1- $\phi$ VSI . . . . .	62
3.3	Classical Control Methods for 1- $\phi$ VSI . . . . .	62
3.4	SMC-Based 1- $\phi$ VSI and Its Limitations . . . . .	66
3.5	Constant-Frequency SMC-Based 1- $\phi$ VSI . . . . .	67
3.5.1	Constant Frequency Operation . . . . .	68
3.5.2	Dynamics of 1- $\phi$ VSI and Its Mathematical Model . . . . .	69
3.5.3	Experimental Validation . . . . .	71
3.5.4	Performance Analysis . . . . .	73
3.6	Selection of an Ellipsoidal Switching Surface . . . . .	77
3.6.1	Dynamics of 1- $\phi$ VSI and Its Mathematical Model . . . . .	78
3.6.2	Performance Analysis . . . . .	79
3.7	Conclusion . . . . .	82
<b>4</b>	<b>Single -Phase Grid-Connected Inverter System</b>	<b>83</b>
4.1	1- $\phi$ GCI System . . . . .	83
4.1.1	Grid-Connected Filter Topologies . . . . .	84

4.2	State-of-the-Art of Current Controllers . . . . .	86
4.2.1	Proposed Control Scheme . . . . .	88
4.3	SMC in Grid-Connected Inverter System . . . . .	89
4.3.1	Dynamics of 1- $\phi$ GCI System and Equation of the SS . . . . .	90
4.3.2	Existence Condition . . . . .	91
4.3.3	Stability Condition . . . . .	92
4.4	Performance Analysis . . . . .	92
4.4.1	Stand-Alone Mode of Operation . . . . .	93
4.4.2	Grid-Connected Mode of Operation . . . . .	95
4.4.3	Seamless Transfer Mode of Operation . . . . .	98
4.5	Conclusion . . . . .	99
<b>5</b>	<b>Dual-Stage Grid-Connected Photovoltaic System</b>	<b>100</b>
5.1	1- $\phi$ Standalone PV System . . . . .	100
5.1.1	Battery Modeling . . . . .	101
5.1.2	Control Strategies . . . . .	102
5.1.3	Small Signal Stability Analysis . . . . .	105
5.1.4	Performance Analysis . . . . .	107
5.2	1- $\phi$ Grid-Connected PV System . . . . .	112
5.2.1	Two-stage Architecture . . . . .	112
5.2.2	System Control Description . . . . .	112
5.2.3	Modeling of 1- $\phi$ GPV System . . . . .	113
5.2.4	Closed-Loop Control Design . . . . .	115
5.2.5	Performance Analysis . . . . .	119
5.3	Conclusion . . . . .	122
<b>6</b>	<b>Conclusion</b>	<b>123</b>
6.1	Summary of Contributions . . . . .	123
6.2	Future Research Directions . . . . .	125
	<b>Bibliography</b>	<b>126</b>
	<b>Dissemination</b>	<b>138</b>
	<b>Dissemination of Work</b>	<b>139</b>

# List of Figures

1.1	Overview of PV inverters. (a) Centralized topology. (b) String topology. (c) Multi-string topology. (d) Module-integrated topology. . .	6
1.2	System diagram of a string-inverter. . . . .	9
1.3	Three types of power processing stages. (a) Single-stage. (b) Dual-stage. (c) Three-stage. . . . .	10
1.4	Grid-connected inverter. (a) Line-frequency-commutated CSI. (b) Diode-clamped multi-level VSI. (c) VSI with high frequency PWM switching. . . . .	13
2.1	Basic PV cell model. . . . .	23
2.2	(a) $i-v$ curve, and (b) $p-v$ curve at different irradiation level. . . . .	24
2.3	(a) $i-v$ curve, and (b) $p-v$ curve at different temperature level. . . . .	24
2.4	Buck converter for PV system. . . . .	26
2.5	Buck converter circuit for (a) on-state, and (b) off-state operation in CCM. . . . .	26
2.6	Boost converter for PV system. . . . .	28
2.7	Boost converter circuit for (a) on-state, and (b) off-state operation in CCM. . . . .	29
2.8	Buck-Boost converter for PV system. . . . .	30
2.9	The schematic showing the series architecture with a string of two MPVS and zooming view of analog MPP tracker. . . . .	34
2.10	The representative characteristics of $\dot{v}$ making $V_{mpp}$ as an attractor. . .	36
2.11	Switching flow diagram of proposed ASMC. . . . .	37
2.12	Hysteritic flow of buck-type MIC for $i_o = 4.8A$ . The other parameters value used are given in Table 5.1. . . . .	38
2.13	Trajectory evolution of ASMC-based MPVS showing the switching and sliding motion for $G = 1000 \text{ W/m}^2$ , $T_c = 25^\circ \text{ C}$ , and $i_o = 4.8 \text{ A}$ . The other parameters value used are given in Table 5.1. . . . .	41

2.14	Performances of boost-type MIC under enhanced existence region $\Pi$ (represented by shadowed region). The parameters value are: $L = 140$ mH, $C = 0.1$ $\mu$ F, and $i_o = 2.3$ A. . . . .	42
2.15	Representative bifurcation diagram showing the fast-scale instabilities of buck-type MIC for $L = 140$ $\mu$ H, $C = 1000$ $\mu$ F, and $i_o = 5.45$ A. Here $T$ is taken as the bifurcation parameter. . . . .	46
2.16	Photograph of indoor test set-up of the PV module. . . . .	49
2.17	Schematic diagram of indoor test set-up. . . . .	50
2.18	(a) The condition for less transient oscillation under sudden irradiation variation from 1000 to 400, and then, from 400 to 30 W/m <sup>2</sup> ; and corresponding experimental validation for irradiation fluctuations: (b) from 30 to 400; and (c) from 400 to 30 W/m <sup>2</sup> . CH 1: $p$ (18 W/div), CH 2: $v$ (10 V/div). All other parameters are same as in Figure 2.13. . . . .	51
2.19	Tracking performance under sudden change of $G$ . . . . .	53
2.20	The dynamic response showing the comparison of coupling effects between Figure 2.9 and P&O based control algorithm for $i_o = 4.8$ A. Here $G_1$ and $G_2$ represent the solar insulations for first and second module, denoted by M-1 and M-2 respectively. . . . .	54
2.21	(a) Representative diagram showing the transient performances of $P_{in}$ and $P_o^d$ (without any cross-coupling effects) for $i_o = 4.8$ A and $R_{eq} = 0.02$ $\Omega$ ; and (b) its experimental confirmation. CH 1 is the clock pulse and CH 2 is the input power $P_{in} \approx 9$ W/div. . . . .	55
3.1	Schematic diagram of inverter topologies: (a) VSI; (b) CSI. . . . .	58
3.2	PWM techniques for VSI: (a) bipolar; (b) unipolar. . . . .	61
3.3	Schematic diagram showing: (a) hysteresis function; (b) the state trajectory in the vicinity of sliding surface $S = 0$ . . . . .	67
3.4	The proposed FFHC-controlled 1- $\phi$ inverter. . . . .	68
3.5	Generation of binary switching pulses $S_1, S_2$ over one half cycle, and the switching sequences of $S_3, S_4$ are complementary of power switches $S_1, S_2$ respectively. . . . .	69
3.6	Laboratory set-up. . . . .	71
3.7	Steady state behavior of $v_o$ and $i_o$ for a non-linear load. (a) Proposed FFHC controller. (b) PWM voltage controller proposed in [1]. While (c) and (d) are the corresponding harmonic spectrum of the output voltage $v_o$ . . . . .	73
3.8	Non-linear load according to IEC62040 standards. . . . .	74

3.9	Steady state response of $v_o$ and $i_o$ . (a) $R$ load. (b) $RL$ load. (c) $RC$ load. (d) non-linear load. . . . .	74
3.10	Comparison of transient response between the proposed FFHC-controller and PWM voltage controller [1] under step load change from no-load to full load: (a) output voltage $v_o$ ; (b) load current $i_o$ . . . . .	75
3.11	Transient output voltage response of the proposed FFHC-controller under nonlinear load change from no load to full load condition. . . . .	76
3.12	Comparison of transient response between the proposed FFHC-controller and PWM voltage controller [1]. The output voltage waveforms under step load change from full-load to no load condition. . . . .	76
3.13	The proposed FFSMC-controlled 1- $\phi$ inverter. . . . .	77
3.14	Steady state response at the rated load. (a) Phase plane plot under proposed ellipsoidal switching surface. (b) Time plot of the of the output voltage and load current. . . . .	80
3.15	Experimental results for $v_0$ and $i_0$ in steady state. (a) $R$ load. (b) Non-linear load. . . . .	81
3.16	The system trajectory under load fluctuation. (a) Hitting in the existence region. (b) Hitting in the non-existence region. . . . .	81
3.17	Transient response of the output voltage and load current of the proposed controller under step load change from : (a) no-load to full load; (b) full load to no-load. . . . .	81
4.1	1- $\phi$ grid-interactive inverter system. . . . .	84
4.2	Overall control diagram of a 1- $\phi$ grid-connected inverter system. . . . .	89
4.3	Laboratory set-up for grid-connected inverter system. . . . .	92
4.4	Stand-alone mode with a resistive load. (a) Steady-state load voltage $v_0$ , 180° shifted reference $v_{ref}$ . (b) Load current $i_0$ . . . . .	93
4.5	Stand-alone mode with the IEC62040 non-linear load. (a) Steady-state load voltage $v_0$ , 180° shifted reference $v_{ref}$ . (b) Load current $i_0$ . . . . .	94
4.6	Experimental results of $v_0$ and $i_0$ in stand-alone mode for: (a) $R$ -load; (b) non-linear load. . . . .	94
4.7	Transient response of load voltage $v_0$ , and load current $10*i_0$ for a step load change from open circuit to 20 $\Omega$ , and back. . . . .	95
4.8	Steady state response in the grid-connected mode. (a) Load current $i_0$ with local load voltage $v_0$ . (b) Grid current $i_2$ with the grid voltage $v_g$ . . . . .	96

4.9	Transient response of the proposed controller on the absence of the local load in the grid-connected mode to a step change in $I^*$ . (a) Grid-current $i_2$ , the reference current $i_{\text{ref}}$ , and the current error $e_i$ . (b) Local load voltage $v_0$ , the reference voltage $v_{\text{ref}}$ and the voltage tracking error $e_v$ . . . . .	96
4.10	Transient response in the grid-connected mode for the step load change from no-load to full load ( $R=20 \Omega$ ) and back. (a) Grid current $i_2$ , its reference $i_{\text{ref}}$ , and the tracking error current $e_i$ . (b) Load current $i_0$ , local load voltage $v_0$ with its reference $v_{\text{ref}}$ , and the tracking error voltage $e_v$ . . . . .	97
4.11	Seamless transfer response from stand-alone to grid-connected mode at $t = 0.085$ s. (a) Grid current $i_2$ , its reference $i_{\text{ref}}$ , and the tracking error current $e_i$ . (b) Local load voltage $v_0$ with its reference $v_{\text{ref}}$ , and the tracking error voltage $e_v$ . . . . .	98
4.12	Seamless transfer response from grid-connected to stand-alone mode at $t = 0.105$ s. (a) Grid current $i_2$ , reference current $i_{\text{ref}}$ , and its tracking error current $e_i$ . (b) Local load voltage $v_0$ , reference voltage $v_{\text{ref}}$ , and tracking error voltage $e_v$ . . . . .	98
5.1	Standalone PV system with battery load. . . . .	101
5.2	Equivalent circuit of a battery. . . . .	101
5.3	PV module with analog MPPT control. . . . .	103
5.4	Control of bidirectional buck-boost converter. . . . .	104
5.5	Control of $1-\phi$ inverter. . . . .	105
5.6	Control block diagram: (a) bidirectional buck-boost converter; (b) inverter. . . . .	106
5.7	Bode diagram: (a) current loop ( $L_{i1}$ ); (b) voltage loop ( $L_{v1}$ ) of buck-boost converter. . . . .	107
5.8	Bode diagram: (a) current loop ( $L_{i2}$ ); (b) voltage loop ( $L_{v2}$ ) of inverter. . . . .	108
5.9	Steady state performance. (a) Output voltage $v_0$ . (b) Load current $i_0$ of inverter. . . . .	109
5.10	Steady state performance at nominal condition. (a) DC-link voltage $V_{\text{dc}}$ . (b) SOC of BSS. . . . .	109
5.11	Transient performance under load variation. (a) Output voltage $v_0$ . (b) Load current $i_0$ . . . . .	110
5.12	Transient performance under load variation. (a) DC-link voltage $V_{\text{dc}}$ . (b) SOC of BSS. . . . .	110



5.13	Transient performance under solar irradiance variation. (a) Output voltage $v_0$ . (b) Load current $i_0$ . . . . .	111
5.14	Transient performance under solar irradiance variation. (a) DC-link voltage $V_{dc}$ . (b) SOC of BSS. . . . .	111
5.15	Schematic diagram of a two-stage 1- $\phi$ GPV system. . . . .	113
5.16	Control scheme for the considered GPV system. . . . .	115
5.17	(a) Grid current control diagram. (b) DC-link voltage control diagram .	117
5.18	Bode plot: (a) current control loop with PI controller; (b) dc-link voltage control loop with PI controller. . . . .	118
5.19	Steady-state current waveforms in inverter stage. (a) Inverter side inductor current $i_1$ . (b) Injected grid current $i_2$ with grid-voltage. . . .	119
5.20	% THD of injected grid current $i_2$ at different power level. (a) Rated output power. (b) 50% of the rated output power. . . . .	119
5.21	Current injected into the grid $i_2$ at different power level. (a) 25% of the rated output power. (b) 50% of the rated output power. . . . .	120
5.22	Transient response of the GPV system. (a) Step change of 0 to 50% of the rated power. (b) Step change of 50% to 100% of the rated output power. . . . .	121
5.23	Transient performance under solar irradiation change. (a) DC-link voltage. (b) Injected grid current $i_2$ and grid voltage $v_g$ . . . . .	121

# List of Tables

2.1	Specification of ASMC based modular PV system for $G = 1000 \text{ W/m}^2$ , and $T_c = 25^\circ\text{C}$ . . . . .	38
2.2	Dynamics of all three MIC architectures and their representation in the form of: $\frac{dx}{dt} = f + gu$ , where $x = [v \ i \ v_o]^T$ . . . . .	39
2.3	System and input matrices $A_i$ and $B_i$ . . . . .	44
2.4	Major Characteristics of MPPT Techniques . . . . .	52
2.5	$\eta$ (%) of series configuration for different $G_1$ ( $\text{W/m}^2$ ) when $i_o = 4.8 \text{ A}$ and $R_{eq} = 0.02 \ \Omega$ . . . . .	55
4.1	steady-state response in grid-connected mode of operation . . . . .	95
5.1	Key Parameters for stand-alone mode . . . . .	108
5.2	Key Parameters for grid-connected mode . . . . .	120

# Chapter 1

## Introduction

### 1.1 Motivation

Over the past few decades, distributed generation (DG) has gained lots of attraction due to the environmentally-friendly nature of renewable energy, the plug-and-play operation of new generation units, and its ability to offer low installation cost to meet the challenges of the electricity market [1–8]. DG units provide power at the point of the load center, which minimizes the losses during power transmission and improves the power quality to the loads. Furthermore, it can also be used as a backup source under the absence of grid.

Photovoltaic modules (PV) [9], wind turbines [10], fuel cells [11], and Micro turbines [12] are used as the sources for the DG units. The DG system powered by the PV source is commonly used, for its low installation and running cost. Presently, the energy supplied by the PV source is approximately 1% of the world energy consumption. Over the past few years, solar power sources demand has grown consistently due to the following factors: 1) increasing efficiency of solar cells; 2) manufacturing technology improvement; 3) economies of scale; and 4) can be installed everywhere. The above factors are making PV system a good candidate to be one of the most important renewable energy sources of the future. This energy source increased at a rate of 20-40% per year in the last few years [13]. Moreover, the modular PV panel configuration of dimension 1 m<sup>2</sup> has an average power ratings of hundreds of watts/panel, broadly adopted by the end consumer. Now all over the world the largest PV power plant is more than 100MW. Furthermore, the output of PV arrays is effected by solar irradiation and weather conditions. More importantly, limited lifespan and high initial cost of PV panels make it more critical to extract as much

power from them as possible. Therefore, maximum power point tracking (MPPT) technique should be realized to accomplish maximum efficiency of PV arrays. Several algorithms have been developed to achieve MPPT technique.

The PV generation can be generally divided into two types: stand-alone systems and grid-connected systems. Since PV modules are easily transported from one place to another, it can be operated in stand-alone mode in remote areas where the grid is not reachable or is not economical to install. This system can also be suitable for telecommunications units, rural electricity supply, and also auxiliary power units for emergency services or military applications. Most PV systems were stand-alone applications until mid-90. A typical stand-alone PV system comprises of a solar array and a storage device. The storage devices include batteries, flywheels, super-capacitors, pumped hydroelectric storage and super-conducting magnetic energy storage devices [14], [15]. Since the solar energy is not possible throughout the day, a storage device is needed as a backup device in order to make the electricity available whenever it is needed. Batteries are commonly used in PV system as a storage device. But the major drawback of the battery in stand-alone PV systems is its cost factor and the bulky size. So the battery needs to be properly designed to obtain the optimal efficiency from the PV system.

Another possibility to take advantage of the PV system is injecting the PV power directly into the existing utility grid. In most parts of the industrially developed world grid electricity is readily available and can be used as a giant battery to store all the energy produced by the PV cells. The PV power first supply to the local load and the rest surplus power is feeding into the grid for the use of other customers. As a result, the burden on the conventional generation units (e.g. thermal power plant) is reducing. When the PV power is not sufficiently available (at night or on cloudy days), then the utility grid can provide power from conventional sources. Removing the battery from the PV system not only make the system economical but also increases its reliability. Generally, the lifetime of a PV cell is more than 20 years, whereas a battery lasts for at most five years and also needs periodic maintenance [16].

A grid-connected photovoltaic (GPV) system comprises a group of energy transducers, i.e., PV panels and dc-dc converter which converts dc power from PV panel side voltage to required dc bus voltage. While a dc-ac converter is used as a power interfacing between the dc PV panels and the ac grid. The dc-ac power processing stage is achieved by feedback controlled inverter systems. This inverter must guarantee that it will inject the current into the grid at unit power factor with the lowest harmonic distortion level. Therefore, PV inverters have an enormous impact on the performance of PV grid-tie systems. One of the most active area of research

for GPV system deals with the way in which the elements of the GPV inverter, PV panels and power converter stage or stages are arranged to transfer the PV power to the utility grid efficiently [17]. Among all configuration "string-inverter" [18] is a suitable candidate, where each string is connected to one inverter and inject power to the grid. Since new strings can be easily added to the system to increase its power rating, system modularity therefore can be maximized. Due to its broadly use and the possibility to easily add other power converter stages, this configuration has been chosen as the power conditioning unit considered in this work.

The control strategy of the dc-ac inverter that interfaces the PV array with the utility grid needs to achieve the following control objectives in order to assure an efficient energy transfer:

- The control strategy applies to the PV module so as to track the MPP for maximizing the energy capture. This function must be made at the highest possible efficiency, over a wide power range, due to the morning-noon-evening and winter-summer variations.
- The efficient conversion of the input dc power into an ac output current which has to be injected into the grid. The current injected into the grid must obey the international standards, such as the IEEE Std. 519 [19] and the IEEE Std. 1547 [20], which state the maximum allowable amount of injected current harmonics.

The motivations of this research project are to address the different power processing stages briefly, i.e., dc-dc stage and dc-ac stage. A proper grid synchronization technique is selected for connecting the PV system with the utility grid. Then respective controllers are designed to ensure the requirement for operating at the MPP imposed by the PV module and requirements for the grid connection specified by international standards.

## 1.2 PV Power System

From the functional perspective point of view solar power systems can be divided into two parts: PV panels, that capture the solar irradiation and transform it into electrical energy; and power conditioning components, like dc-dc converters, dc-ac inverters, controllers, etc., which convert the variable voltage dc power into dc or ac power as per the load requirements.

### 1.2.1 Evolution of PV Cell and Module

Various PV cell technologies by using different materials are available on the present PV market. Research has been focused on PV cells and materials as it includes almost half of the system cost. The PV cell technologies are categorized into three generations based on the manufacturing process and commercial maturity.

The first generation solar cells are based on silicon wafers including mono-crystalline silicon and multi-crystalline silicon. Mono-crystalline cells have more efficiency than multi-crystalline cells, but its manufacturing cost is high. These PV cells have an average efficiency of 12% to 14%. These types of solar cells dominate the PV market due to their good performance, long life and high stability. These are mainly mounted on rooftops. However, they are relatively expensive and require a lot of energy in production.

The second generation solar cells are focused on amorphous silicon thin film, Copper-Indium-Selenide and Copper-Indium-Gallium-Diselenide thin film, and Cadmium-Telluride thin film, where the typical performance is 10 to 15%. The efficiencies of these PV cells are less than first generation. These thin films can be developed on flexible substrates. As an advantage of thin film solar cells, these can be developed on large areas up to 6 m<sup>2</sup>. However, wafer-based solar cell can be only produced in wafer dimensions. The thin film PV cells are also commonly used in the recent market.

The third Generation solar cells include nanocrystal-based solar cells, polymer-based solar cells, dye-sensitized solar cells, and concentrated solar cells. These are the novel technologies which are promising but are still under development. Most developed this solar cell types are dye-sensitized and concentrated solar cell. Dye-sensitized solar cells are based on dye molecules between electrodes. Electron-hole pairs occurred in dye molecules and transported through nanoparticles  $TiO_2$ . Although the efficiency of these PV cells is very low, their cost is also very low. Their production is smooth concerning other technologies.

Even though all the exciting progress in the cell technologies around the world, PV cells based on crystalline silicon are commercially used in the market. A cluster of the PV cells connected in series forms a PV module. The PV modules are mechanically robust enough to come with a 25 year limited warranty and a guarantee of 1% power degradation per year. Crystalline silicon modules can be categorized into mono-crystalline and polycrystalline, also referred as multi-crystalline, silicon type cells. They consist of front surface glass, encapsulate, 60 to 72 interconnected PV cells, a back sheet and a metal frame. The standard front surface glass is a low cost

transparent tempered low iron glass with self-cleaning properties. This type of glass is strong, stable under ultraviolet radiation and water and gas impervious. Ethylene vinyl acetate (EVA) is commonly used as encapsulant material. It helps to keep the whole module bonded together. EVA is optically transparent and stable under high temperature and UV radiation. Generally, EVA is placed between a front glass surface and PV cell, and between back sheet and PV cell. The back sheet is typically made of Tedlar, which provides protection against moisture and gas ingress. The module frame is usually made of aluminum. It is believed that these PV modules would continue to dominate the PV market for at least another decade [21]. This belief is further strengthened by the recent plummeting of the cost of silicon PV modules.

### 1.2.2 Grid-Connected PV System

The PV energy generated from sunlight is captured by PV modules. The power produced by the PV modules are dc electrical power. Integrating the dc power from the PV modules into the existing ac power distribution network can be achieved through grid-tie inverters. The inverters must guarantee that the PV modules are operating at MPP, which is the operating condition where the most energy is captured. Another function for inverters is to control the current injected into the ac grid at the same phase with the grid voltage at the lowest harmonic distortion levels. Therefore, PV inverters have an enormous impact on the performance of GPV systems. Depending on different levels of MPPT implementation for PV modules, four PV inverter topologies are reported [22], [23], [24].

#### I. Centralized Topology

The topology shown in Figure 3.1(a) is based on centralized inverters, which interfaced a large number of modules to the grid [25]. It is commonly used for large PV systems with the high output power of up to several megawatts. In this topology, a single inverter is connected to the PV array. The main advantage of the centralized topology is its low cost as compared to other topologies as well as the ease maintenance of the inverter. However, this topology has low reliability as the failure of the inverter will stop the operation of PV system. Moreover, there is a considerable amount of power loss in the cases of mismatch between the modules and partial shading, due to the use of one inverter for tracking the MPP [26], [27].

#### II. String Topology

The string inverter (see Figure 3.1(b)) is an improved version of the centralized

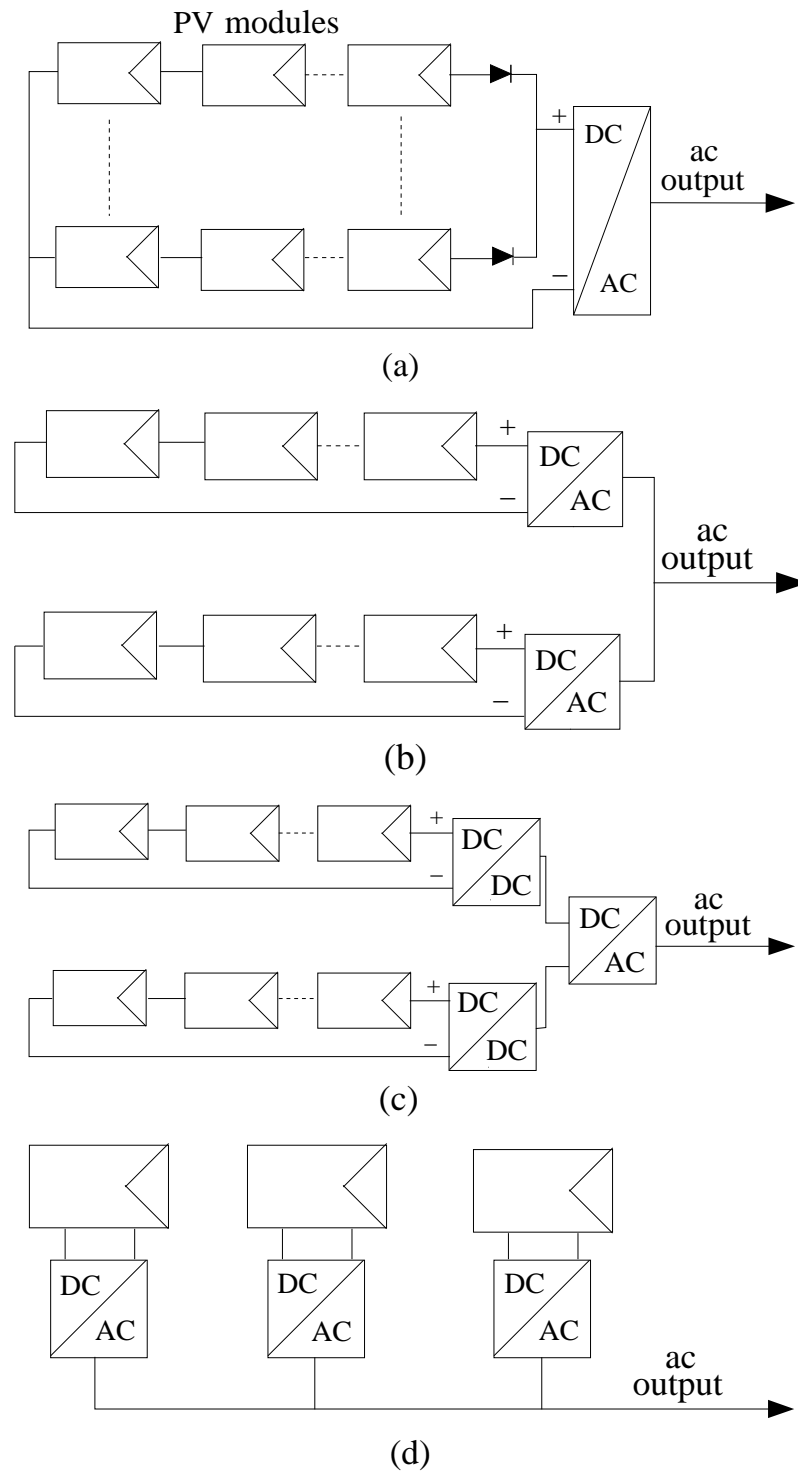


Figure 1.1: Overview of PV inverters. (a) Centralized topology. (b) String topology. (c) Multi-string topology. (d) Module-integrated topology.



inverter. In this topology, each string is connected to one inverter [27], [18] and therefore the system's reliability is enhanced. The input voltage may be high enough to avoid voltage amplification. Here, the losses due to partial shading are minimized because each string can operate at its own MPP. The string topology increases the flexibility in the design of the PV system as new strings can be easily integrated to the existing system to increase its power rating. Generally, each string can have a power rating of up to 3-4 kW. This technology offers improved performance compared to the past central topology in the following ways:

- (a) Distributed MPP tracking leads to increase in the overall efficiency compared to the centralized inverter. Moreover, the cost of manufacturing and thus the sale price is reduced due to mass production.
- (b) It provides the possibility of up-scaling the system due to the modular structure.
- (c) It is more user-friendly because of its straight forward structure with Plug-and-Play feature.
- (d) It is based on forced-commutated dc-ac converters employing IGBTs, resulting in low harmonic content and thus high power quality.

### III. Multi-String Topology

The multi-string inverter (see Figure 3.1(c)) is an advanced development of the string-inverter, where several strings are interfaced with their own dc-dc converter and then, to a common dc-ac inverter [24], [28]. This is beneficial as compared to the centralized inverter system since each string can be controlled separately. The consumer may start his/her own PV power plant with a few modules. Further enlargements are easily done because a new string can be connected into the existing system. A flexible design with high efficiency is hereby obtained. Although multi-string type offer an improvement compared with centralized type, they still undergo from some disadvantages as high capital cost associated with procurement and installation.

### IV. Module-Integrated Topology

The module integrated type inverters shown in Figure 3.1(d) are also known as micro-inverters, and the output power range is commonly inbetween 200 W and 300 W. Each PV panel has a single inverter fixed at the back. The output of micro-inverters are connected together to convert raw dc power from PV panel to

ac power and inject power into the grid, thus no high voltage dc cable is needed as centralized type inverters.

Since micro-inverters can perform a dedicate PV power harvest for every single PV panel, the misleading problems caused by shading, dirt, dust, or other possible non-uniform changes in irradiations and temperatures are reduced compared with other types inverters. Moreover, micro-inverters have low dc-link voltage, thus when failure cases occurred it is easy to repair or replace the broken part. During this process little affection will happen on the whole power generation system. These plug-and-play inverters are simple in maintenance, easily installed, and possible in mass production [28], [29], [30]. In addition they offer greater flexibility by allowing the use of panels with different specifications, different ratings, or produced by different manufacturer. Now-a-days, these inverters would be the development trend of PV system design.

### 1.3 A Brief Introduction to the String-Inverter Topology

In order to achieve high dc-link voltage, the PV system employs the string inverter topology due to its advantages over the central inverter topology. If the dc voltage level is very high before the inverter, then there is no need of the dc-dc power stage, otherwise, a dc-dc converter can be used to boost it. For this topology, each string has connected with its own inverter and therefore the requirement of string diodes is eliminated leading to reduction in total lossess of the system. This topology allows individual MPPT for each string; hence, the reliability of the system is enhanced due to the fact that the system is no longer dependent on only one inverter compared to the central inverter topology. The mismatch losses are also minimized, but not eliminated. This leads this topology increases the overall efficiency, with reduction in cost due to the mass production.

The external connections and internal structure of the string-inverter topology are shown in Figure 1.2. It consists of two major parts: a power processing part and a power control part. The power processing part is connected to a PV module on the input side. The PV module output is fed to the power circuit, which converts the dc into ac required by the utility. The power circuit may be single stage or two stages. As the fast switching waveforms of the present day inverter technology would generate high frequency electromagnetic noise, an low pass passive filter is needed between the

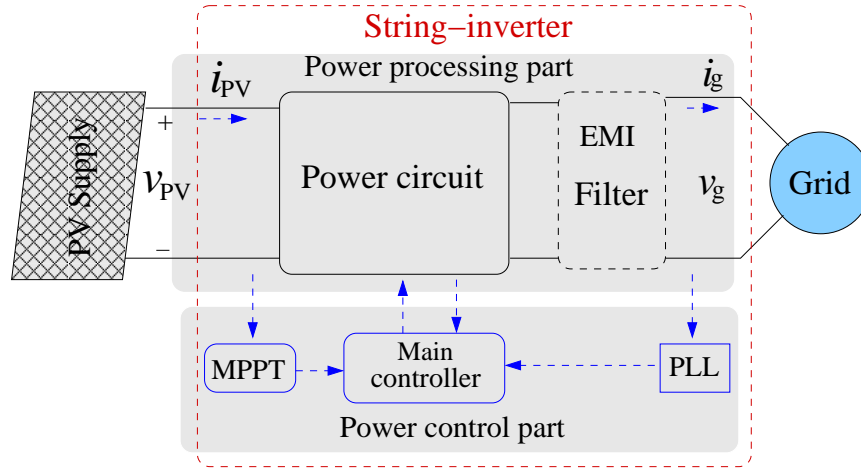


Figure 1.2: System diagram of a string-inverter.

inverter and the utility to prevent high frequency noise currents from entering the grid and causing interference to other systems connected to the same utility.

The power control part is divided into three function blocks based on the requirements of the PV panel and grid connection. Among them, MPPT is used to obtain the maximum power from the PV panel as the panel's output characteristics changes with environmental conditions. The phase lock loop (PLL) synchronization block plays a crucial role in grid-connected PV system. It helps in synchronizing the inverter output voltage with the grid voltage. Detailed requirements and specifications are listed in several national and international standards concerning the interconnection of distributed generation systems with the grid. Receiving the signals from MPPT and grid through PLL, the main controller directly controls the inverter to obtain a sinusoidal output current in phase with the grid voltage and with a low Total Harmonics Distortion (THD).

As an interface between PV system and the ac grid, the power circuit of a sting-inverter needs to cater to the requirements from both sides. It needs to have; 1) MPPT function to match with the PV module, and 2) high voltage boost and dc/ac conversion capability to match with the grid. These requirements are further explained in the later section.

## 1.4 Existing Inverter Topologies in GPV System

For the GPV system, each string is connected to one inverter, and hence the reliability of the system is enhanced. Inverter placed inbetween PV module and output side grid

mainly performs three functional operations such as; boost the input voltage, dc-ac voltage inverting, and MPPT operation. There are different inverters topologies are reported in the literature. The topologies are classified on the basis of number of power processing stages, location of power decoupling capacitors with and without transformer connection, and the types of grid interfacing units.

### 1.4.1 Power Processing Stages

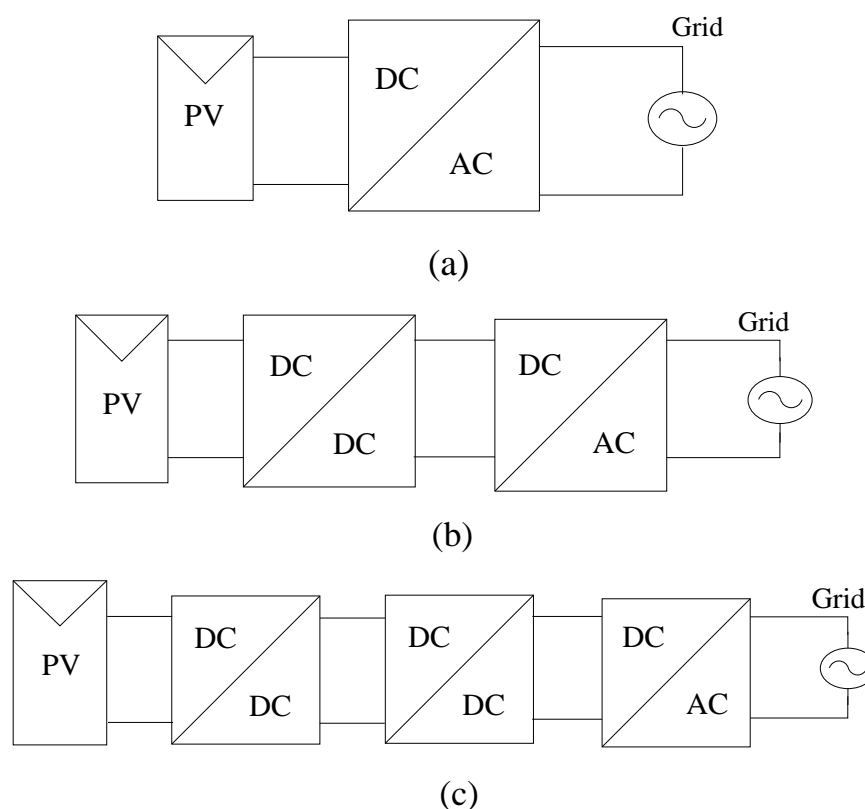


Figure 1.3: Three types of power processing stages. (a) Single-stage. (b) Dual-stage. (c) Three-stage.

The first grouping is the number of cascaded power processing stages. These types of configuration are used for a string-inverter. Three classes of power processing stages are shown in Figure 1.3. The inverter shown in Figure 1.3(a) is a single-stage inverter which must handle all functions itself like - MPPT, grid current control, and voltage amplification applications. As three functions have to be implemented on a single stage, the controller need to be much more complicated [18], [31]. Several single stage inverter topologies with suitable control schemes have been reported in literature [32].

Their applications as GPV systems are still very limited, especially in the high power applications.

Figure 1.3(b) shows a dual-stage inverter model, where dc-dc converter incorporated inbetween the MPPT operation and the voltage amplification. Based on the voltage conversion classification, benefit from the two stages is that the dc voltage boosting function and dc-ac voltage inverting function could be decoupled. Whereas based on the power-transfer consideration, bus voltage balance function and the MPPT function would be separated so that the circuit and controller design would be much more simpler. The dual-stage inverters are dominate in the GPV system nowadays. Depending on the dc-ac inverter control, the output of the dc-dc converters is either a pure dc voltage or the dc-dc converter's output current is modulated to track a rectified sine wave. In the former case, the dc-ac inverter is regulating the grid current by using a pulse width modulation (PWM) technique or bang-bang controller. While in the latter, the dc-ac inverter is switching at line frequency, and the dc-dc converter takes care of the current control. If the nominal power is low, then a high efficiency can be achieved in the latter case. On the other hand, if the nominal power is high, it is advisable to operate the grid-connected inverter in PWM mode. The main advantage of this method is that it has a better control of each PV module [33], [34].

The three-stage inverters are implemented (see Figure 1.3(c)) with the two dc-dc converters and a dc-ac inverter. The first dc-dc converter stage is used to produce a constant low dc voltage. The second dc-dc converter stage is used to provide the high voltage gain as well as isolation, and the third dc-ac inverter stage converts the dc power into ac power and injects it into the grid [28], [35]. The three-stage inverter has the best reliability as compared to the single and dual- power processing stages. However, it also has the poor efficiency because the number of energy processing stages are more.

## 1.4.2 Power Decoupling

Power decoupling is generally obtained by using an electrolytic capacitor to mitigate the power ripple effect at the PV-module side. As the operational lifetime of the capacitor is the primary limiting factor, it should be therefore kept as small as possible and preferably replaced by film capacitors. Based on the location of the decoupling capacitor, three decoupling techniques are adopted: 1) PV-side decoupling; 2) dc-link decoupling; and 3) ac-side decoupling [30]. The required decoupling capacitor is given by

$$C = \frac{P_{PV}}{2\omega_g V_c \Delta V} \quad (1.1)$$

where  $P_{PV}$  is the PV modules' nominal power,  $V_c$  is the capacitor voltage, and  $\Delta V$  is the ripple voltage. From (1.1) it can be calculated that a parallel capacitor of 2.4  $\mu\text{F}$  is required across the PV module for  $V_{MPP} = 35 \text{ V}$ ,  $\Delta V = 3 \text{ V}$ , and  $P_{MPP} = 160 \text{ W}$ . However, if the capacitor is located at the dc link, it is sufficient to use 33  $\mu\text{F}$  at 400 V with a ripple voltage of 20 V for the same PV module. In this work, dc-link decoupling technique is used due to high PV nominal voltage.

### 1.4.3 Types of Grid Interfacing

Figure 1.4 shows three, out of many, possible grid interfacing inverters [22], [24]. The topology shown in Figure 1.4(a) is a line-frequency-commutated current-source inverters (CSIs). The current into the stage is already modulated or controlled to a rectified sinusoidal waveform and the task for the circuit is simply to recreate the sine wave and feed it into the grid. The zero-voltage switching (ZVS) and zero-current switching (ZCS) are employed, and thus only conduction losses of the semiconductors present.

The topology shown in Figure 1.4(b) is a diode clamped three-level half-bridge VSI (also called multilevel VSIs), which can generate 3, 5, 7.... fixed voltage levels across the inductor and grid. The main advantages are the switching frequency of each transistor can be reduced and also the harmonic distortion in the output voltage of the inverter is less as compare to the other inverter topologies. However the limitations of this topology are its complex structure and switching schemes. Therefore reviewing the above grid interfacing topologies, it is concluded that three level full bridge VSI is suitable for this work.

Lastly, the topology shown in Figure 1.4(c) is a three-level full-bridge inverter, which can produce a grid current by using the positive or negative or zero dc-link voltage. The output voltage of the inverter generated by this strategy has double switching frequency, as a results the filter size will be reduced. It also avoids the internal reactive power flow due to the freewheeling action of two anti-parallel diode. On the other hand, the two level full-bridge VSI can generate two fixed voltage level and requires twice dc-link voltage and double switching frequency in order to achieve the same performance as the three-level VSI. The output inductor current has high current ripples, leading to deteriorate the power quality of the inverter. Another limitation of this method is that the internal reactive power is produced, as the current freewheeling action happens through the anti parallel diodes to the dc-link capacitors.

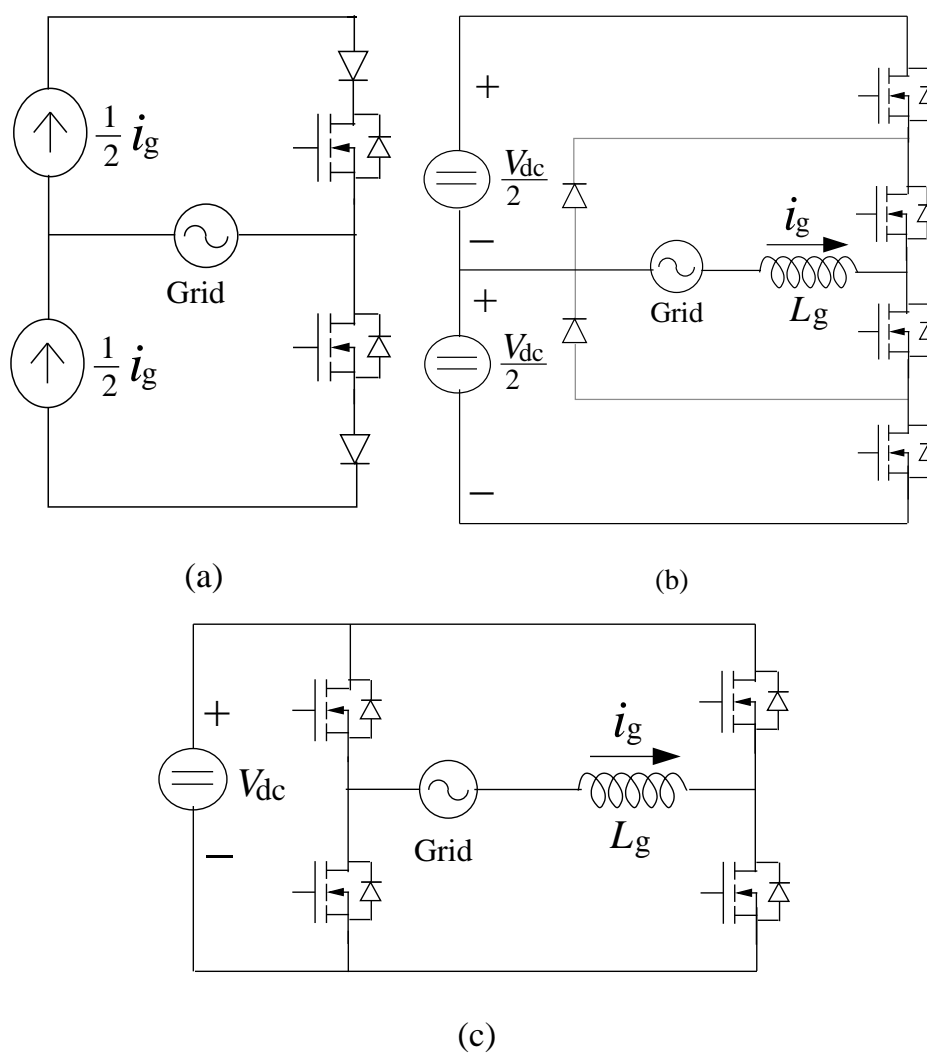


Figure 1.4: Grid-connected inverter. (a) Line-frequency-commutated CSI. (b) Diode-clamped multi-level VSI. (c) VSI with high frequency PWM switching.

The controlled pulses for the switches in the VSI and the reference for the grid-current waveform are mostly based on measured grid voltage or zero-crossing detection. But the above methods are not suitable under the distorted grid condition [36]. The above problem can be solved by using a phase-locked loop (PLL), as it collects the grid voltage phase information and generates a pure sinusoidal reference current for the grid.

#### 1.4.4 AC PV Module

AC PV module is also known as the PV panel integrated with a micro-inverter as shown in Figure 3.1(d). The output ac power of a PV module could be directly

connected to a utility grid. The concept was first suggested by Caltech's Jet Propulsion Laboratory [37] in the 1970s. From the 1990s, this technology of ac module is developed rapidly with the support from the government. With many advantages over central inverter systems, the ac PV module is treated as the future development trend of PV solar power systems. The rated ac power of a PV module could be in the range of 100W or even less. Thus, the minimum system could be as small as 100W or even less. With required power size increasing, more and more ac modules could be integrated to the existing system. The system capacity could be increased to any desired power range. So these are more suitable for both residential PV system and PV farm system. With the flexible system size, the ac PV module has significant market potential.

## 1.5 Specification, Demand and Standards for GPV Systems

Inverter interfacing to the GPV system should have two primary tasks. One is to operate the PV system at the MPP. The other task is to inject a sinusoidal current into the grid with unity power factor. The above two functions are broadly discussed here.

### I. Demands Defined by the Grid

The utility companies must maintain an approved standard for the grid-connected DG system. Here, the present international standard IEEE-1547 [20] and the future standard IEC-61727 [19] are worth considering. These measures involve with issues like detection of stand-alone operation, power quality, and grounding. Detection of stand-alone operation is essential for the inverter, as it take appropriate measures to protect equipment. Under stand-alone operation, the grid is disconnected from the inverter so that it will supply power to the local loads. The detection methods are commonly classified into two categories, such as active and passive. Since this work is focused on the seamless transfer method, so that the above stand-alone detection methods will not be discussed. The IEEE-1547 [20] standards have limitations on the maximum allowable injected dc current into the grid to avoid saturation of the distribution transformers [38]. The range of the dc current is about 0.5% to 1% of the rated output current. This problem can be solved by connecting a line-frequency transformer between the grid and the inverter. Assuming that



the grid voltage and grid current are free from harmonics and both are in phase. Then, the instantaneous power injected to the grid is given by

$$p_g = 2P\sin^2(\omega_g t) \quad (1.2)$$

where  $P$  is the average power,  $\omega_g$  is the angular grid frequency, and  $t$  is the time.

## II. Demands Defined by PV Modules

The inverters must ensure that the PV module(s) is operated at the MPP so that maximum energy can be captured from the module(s). This is achieved by an MPP tracker. It also takes into account that the voltage ripple appears at the PV module(s) terminals should be sufficiently small, as it operates around the MPP without considerable fluctuation. The ripple voltage amplitude and the utilization ratio has a relationship, given as [22]

$$\Delta V = \sqrt{\frac{(2U_{pv} - 1) P_{MPP}}{3\alpha V_{MPP} + \beta}} \quad (1.3)$$

where  $\Delta V$  is the ripple voltage amplitude,  $U_{pv}$  is the utilization factor which is the ratio between the generated average power to the calculated MPP power,  $V_{MPP}$ , and  $P_{MPP}$  are the PV voltage and power at MPP,  $\alpha$  and  $\beta$  are the coefficients representing a second-order Taylor approximation of the current. It is calculated that 98% utilization ratio can be achieved at the ripple voltage amplitude less than 8.5%. As seen in (1.2), the pulsating power of double grid frequency is injected to the grid, so a power decoupling device must require for the inverter.

## III. Demands Defined by the User

Finally, the owner (the user) also has to say few words. The users demand a low-cost, reliable inverter topology, a high efficiency over a wide variation of the input voltage and input power, as both the variables depend on the solar irradiation and ambient temperature. The user also demands long operational lifetime warranty of 10 to 15 years at an efficiency of 75%, and a material and service warranty of 5 years. But the electrolyte capacitor used in the inverter as a power decoupling device between the PV module and utility grid [39] is the principal limiting component. The operational lifetime of an electrolytic capacitor is given by [40]

$$T_{OT} = T_{OT,0} 0.2^{\left(\frac{T_0 - T_h}{\Delta T}\right)} \quad (1.4)$$

where  $T_{OT}$  is the operational lifetime,  $T_{OT,0}$  is the lifetime at  $T_0$ ,  $T_h$  is the hotspot temperature, and  $\Delta T$  is the rise temperature. However, the operational lifetime of the capacitor can be improved when the inverter are placed indoors.

From the above discussion, it can be observed that inverter plays a significant role in the grid-connected PV system. Such a design of the inverter is given in the next section.

## 1.6 Design Considerations of String-Inverter

Based on the previous analysis and discussion (see Section 1.2.2) of the PV power generation systems, the string-inverter topology is selected to establish the PV system in this thesis. Since the performance of this inverter is determined by the factors such as; isolation, efficiency, reliability, and power density, these factors should be kept in mind for designing of an inverter.

- **Isolation:** In the grid-connected system, isolation is required in PV installation. The isolation is realized through a transformer. But the use of transformers, system becomes bulky, heavy, and expensive. Even though significant size and reduction in weight can be obtained with high frequency transformer, the use of transformer still deteriorates the efficiency of the entire PV system. Therefore, transformerless PV systems are commonly used to overcome these issues. They are smaller, lighter, lower in cost, and highly efficient [41].
- **Efficiency:** The efficiency of the overall system is determined by PV panel efficiency, MPPT performance and inverter conversion efficiency. The PV panel efficiency is determined by selecting one of the PV cell technology as discussed in Section 1.2.1, where MPPT is the prime component for tracking the maximum power of PV panel continuously under changing environmental condition (i.e., solar irradiance and temperature). The MPPT performance or tracking efficiency is assessed with static and dynamic condition. The commercial inverter MPPT efficiency is always greater than 98%. The inverter conversion efficiency is a weighed conversion efficiency that considers several operating conditions [42]. The inverter conversion efficiency is the crucial factor from the investor point of view.
- **Power Density and Reliability Issues:** The power density is an important factor to decrease the volume and cost of the inverter. Since the number of modules in a string is connected to a single inverter (see Figure 3.1(b)), the volume is preferred to be small. Most commercial PV modules are guaranteed to perform at specified levels of output for 20 to 25 years [43]. Integrating the inverter to the PV module necessitates that they both must have matched

expected lifetimes so that the inverter should also have a lifetime for 20 to 25 years.

Based on these above factors, a few design guidelines can be given for string-inverters as:

1. Out of single, dual, and three-stage inverters, a dual-stage inverter structure is suitable because of its better efficiency with high-quality (low THD) ac output voltage.
2. Selection of proper switching technique which would improve the inverter conversion efficiency as well as the power density.
3. Considering isolation requirement, as low-frequency transformer is not only large but also power consuming, so the transformerless topology should be selected in the inverter design.
4. The capacitance of system is preferred to be the smaller and better to improve the reliability.

## 1.7 Objectives of the Research Project

This research work aims at broadly developing new control algorithms for the PV system interface that guarantee stable and high power quality injection under the network disturbances and uncertainties. Although the advantages of dual-stage string-inverters have been recognized as a suitable one, wide adoption of GPV system still presents many challenges. This research work is focused on addressing these challenges with the following objectives.

- **Improved MPPT Performance**

To maximize the output power of a PV system, continuously tracking the MPP of the system is necessary. The main challenges for MPPT of a solar PV array include: 1) how to track an MPP quickly, 2) how to stabilize at an MPP, and 3) how to make a smooth transition from one MPP to another under sharply changing weather conditions. In general, designing a fast and robust MPPT controller (with high tracking performance) for the GPV system is a challenging task. In order to effective design and development of solar PV systems, it is important to investigate and compare the performance, and advantages or disadvantages of conventional MPPT techniques used in the solar PV industry,

and develop a new MPPT technique for fast and reliable extraction of solar PV power.

- **Power Quality and Efficiency Issues**

A PV system can be operated in stand-alone mode or grid-connected mode. Maintaining good voltage regulation and achieving fast dynamic response under sudden load fluctuation are extremely important in stand-alone PV systems. Moreover, the THD of inverter output voltage should be within the limit even for nonlinear loads. In the grid-connected mode of operation, it is important to inject a low THD current from PV system to grid at unity power factor. Nowadays, research is focused to achieve low THD for the local load voltage and the injected grid current simultaneously. Growing demand for maximized energy extraction from PV sources have stimulated substantial technology development efforts towards high-efficiency PV grid-connected inverters.

## 1.8 Major Contributions and Outline of the Dissertation

The following are the most significant contribution of this thesis:

1. This research work proposes a fast and robust analog-MPP tracker (also called as analog sliding-mode controller (ASMC)) which is implemented and designed by using the concepts of Utkin's equivalent control theory and fast-scale stability analysis. The main objectives of applying such concepts are to provide the control support for the MPPT system which are required for 1) guaranteed stability with high robustness against the parameters uncertainties, and 2) fast dynamic responses under rapidly varying environmental conditions. This cannot be met by conventional digital or analog MPPT controllers without continuously tuning the controller parameters and complex controller architecture. Thus, the choice of this analog solution is quite attractive because of its low cost and capability of easy integration with a conventional dc-dc converter in the integrated circuit (IC) form, so that plug-and-play operation for many low power residential PV applications can be easily achieved.
2. Maintaining good voltage regulation and achieving fast dynamic response under sudden load fluctuation are extremely important in stand-alone PV systems. In this work, a fixed frequency hysteresis current (FFHC) controller is proposed,

which is implemented on the basis of sliding mode control (SMC) technique and fixed frequency current controller with a hysteresis band. This has been verified and compared with the carrier based pulse width modulated (PWM) voltage controller under the same load fluctuation. The proposed method is then applied to a prototype 1kVA, 110V, 50Hz 1- $\phi$  voltage source inverter (VSI) system. The results show that the dynamic response is quite faster than that of widely used PWM-controlled inverter systems. Moreover, the THD of inverter output voltage is less at standard nonlinear load IEC62040-3.

3. A PV system can be connected to the utility grid, injecting power into the grid besides providing power to their local loads. In this work, a cascaded SMC strategy is proposed for a grid-connected inverter system to simultaneously improve the power quality of the local load voltage and the current exchanged with the grid. The proposed controller also enables seamless transfer operation from stand-alone mode to grid-connected mode and vice versa. The proposed method is then applied to 1-kVA, 110V, 50Hz grid-connected 1- $\phi$  VSI system. The results show that the steady-state response and the dynamic response are quite attractive.
4. Finally, a typical stand-alone PV system comprises of a solar array and a storage device i.e., battery. In this mode of operation, the battery is used as a backup source for power management between the source and the load. Lead-acid battery is used in high power PV applications due to its low cost and availability in large size. The modeling of a lead-acid battery by using the equivalent circuits are discussed here. Three independent control loops are proposed to control the standalone PV system; MPPT control loop for extracting maximum power from PV module, battery control loop for bidirectional power flow between battery and dc-link through buck-boost converter to keep the input dc voltage constant and inverter control loop for maintaining good voltage regulation and achieving fast dynamic response under sudden load fluctuations. Similarly, a cascaded sliding mode control is proposed for GPV system to regulate the current from PV system to the grid at a lower THD level.

The dissertation will be organized as following:

**Chapter-1** gives a brief introduction of the PV system. The renewable energy sources have gained lots of attraction due to the environmentally-friendly nature, and the plug-and-play operation. Among various renewable energy sources, solar energy is commonly used, for its low installation and running cost. It is extremely suitable

for large-scale power generation. The PV system consists of two major parts: a power processing part and a power control part. The power processing part have been analyzed carefully, which is the objective of this thesis. Based on the considerations of efficiency, power density, galvanic isolation and reliability, several restrictions are reviewed to guide the particular design of the inverter.

**Chapter-2** provides the brief study of dc-dc power processing stage. The dc-dc converter plays a major role in dual stage PV system in converting dc power from PV panel at low voltage to high dc bus voltage. Out of various topologies, conventional non-isolated dc-dc converters have been studied. A novel MPPT with fast tracking performance and guaranteed stability with high robustness against the parameters uncertainties is proposed to track the maximum power from the PV modules. The feasibility of the proposed MPPT method is proved mathematically. Finally, the analytical results have been validated with the help of simulations and experiments.

**Chapter-3** provides the study of dc-ac power processing stage. A brief introduction is given on dc-ac inverter topologies. To improve the inverter efficiency, the modulation technique should be employed. Thus, a review of the modulation techniques on inverters is given. The stand-alone mode of operation with a fixed dc supply will be considered here. Maintaining good voltage regulation and achieving fast dynamic response under sudden load fluctuation are vital for a dc-ac inverter system. The SMC is proposed to meet the above requirements. Simulation and experiment results verify the theory analysis.

**Chapter-4** provides the grid integration of the PV system. In this chapter, the dc source is interfaced with utility grid through a single-phase inverter. It is important to inject a low THD current from PV system to grid at unity power factor. This can be achieved by using a phase lock loop (PLL), which collects the grid voltage phase information and produce the reference current for the Inverter. Moreover, the analysis and design of a single-phase inverter system including inductor-capacitor-inductor (LCL) filter and the phase-lock loop is discussed here. A cascaded SMC controller has been designed to meet the above power quality issues as well as to achieve the seamless transfer operation. Simulation and experiment results also verify the theory analysis.

**Chapter-5** provides the GPV operation, which is formed by combining all the power processing stages, discussed in the previous chapters. The PV system can either be connected in standalone mode or grid-connected mode. A typical stand-alone PV system comprises of a solar array and a storage device i.e., battery. The modeling of a commonly used battery, i.e., lead-acid battery by using the equivalent circuits are discussed in this chapter. Separate controllers are proposed for the both mode of

operation to address the power quality issues discussed in **Chapter-1**.

**Chapter-6** summarizes the whole thesis and describes the future work developed.

# Chapter 2

## DC-DC Power Processing

The dc-dc converter plays an important role in dual-stage PV system in converting dc power from PV panel at low voltage to high dc bus voltage. The input side of the dc-dc converter is connected with the PV source, which leads a wide range of input voltage fluctuation due to change in operating condition of the PV cells. The function of the converter is to keep the output voltage constant. Again the output power of the PV source is continually affected by the environmental factors like irradiation and temperature. The MPPT is used to control dc-dc converter such that the power extracted from PV panel is maximized. The mathematical modeling of PV cell, review of various dc-dc converter topologies, and Implementation of a fast tracking MPPT will be discussed in this chapter.

### 2.1 Mathematical Modeling of PV Cell

Nowadays, PV cells are manufactured based on the p-n junction crystalline silicon materials. The behavior of PV cells can be approximated by a common diode equation. The basic PV cell model is presented in Figure 2.1, which is a p-n junction diode in parallel with a constant current source [21]. This single diode model can also be used to find out the electrical behavior of  $N$  series PV cells. Here,  $i_{PV}$  represents the light induced current,  $R_{sh}$  and  $R_s$  are the shunt and series resistance respectively. The parallel resistance  $R_{sh}$  accounting for current leakage through the cell, around the edge of the device, and between contacts of different polarity. The series resistance  $R_s$  causes an extra voltage drop between the junction voltage and the terminal voltage of the solar cell. The current  $i_{PV}$  is proportional to the solar radiation (insolation) and the resistances represents the various losses. The current flowing through the diode



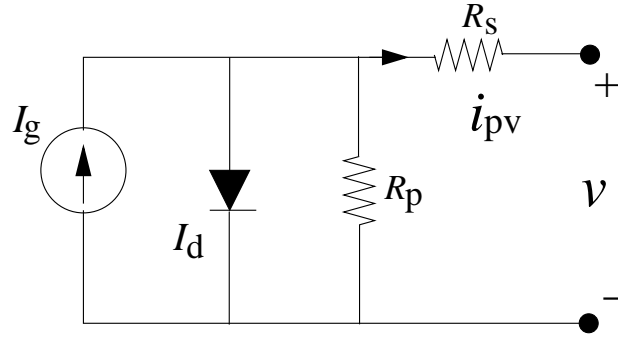


Figure 2.1: Basic PV cell model.

$I_d$  can be derived from an ideal p-n junction diode equation as [21]

$$I_d = I_{\text{sat}} \left[ \exp \left( \frac{v_{\text{pv}} + i_{\text{pv}} R_s}{\eta N V_T} \right) - 1 \right] \quad (2.1)$$

where  $\eta$  is the ideality factor which depends on the fabrication process and semiconductor material of the cell,  $I_{\text{sat}}$  is the reverse saturation current of the on-junction, and  $V_T$  is the thermal voltage of the diode junction which is given by

$$V_T = \frac{kT}{q} \quad (2.2)$$

Here,  $k$  is the Boltzmann's constant ( $1.38065 \times 10^{-23} \text{ J/K}$ ),  $T$  represents the cell's temperature, and  $q$  is the electron's charge ( $1.6 \times 10^{-19} \text{ C}$ ). As the value of series resistance  $R_s$  is very low and the value of shunt resistance  $R_{\text{sh}}$  is very high, so both can be ignored. Based on (2.1) and (2.2) the mathematical model of solar cell can be described by

$$i_{\text{PV}} = I_g - I_{\text{sat}} \left[ \exp \left( \frac{v_{\text{pv}}}{\eta N V_T} \right) - 1 \right] \quad (2.3)$$

The safe operating voltage and current of the cell can be calculated from the open circuit and short circuit conditions respectively. The short-circuit current is the maximum current flowing when the voltage is set to zero for a given temperature and irradiation. This gives  $I_{\text{sc}} = I_g$  (see the equation (2.3)).

Similarly the open circuit voltage can be calculated for a given temperature and irradiation by setting the cell current is equal to zero:

$$V_{\text{OC}} = \frac{kT}{q} \ln \frac{I_g + I_{\text{sat}}}{I_{\text{sat}}} \quad (2.4)$$

The output power of the PV cell is given by multiplying the voltage and current which belongs to the  $i$ - $v$  curve. For the high efficiency operation, it is desired to

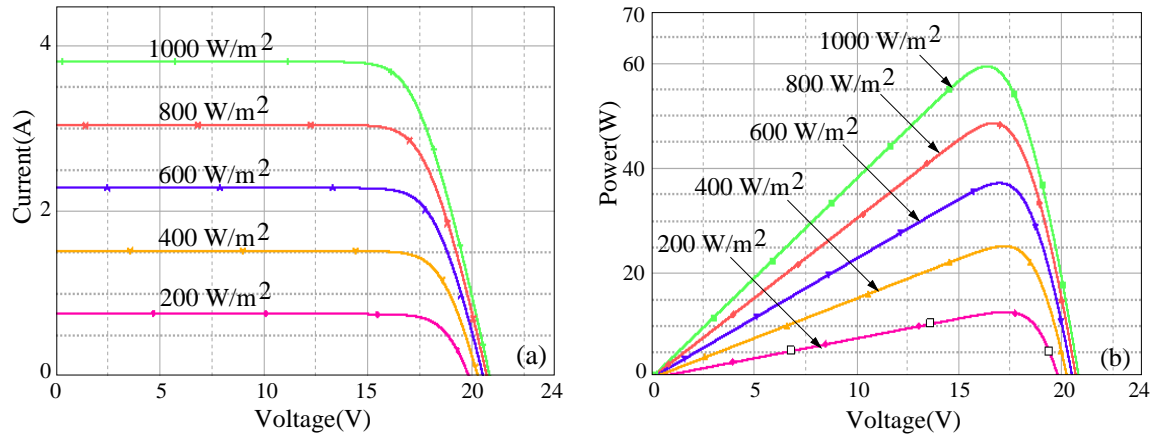


Figure 2.2: (a)  $i-v$  curve, and (b)  $p-v$  curve at different irradiation level.

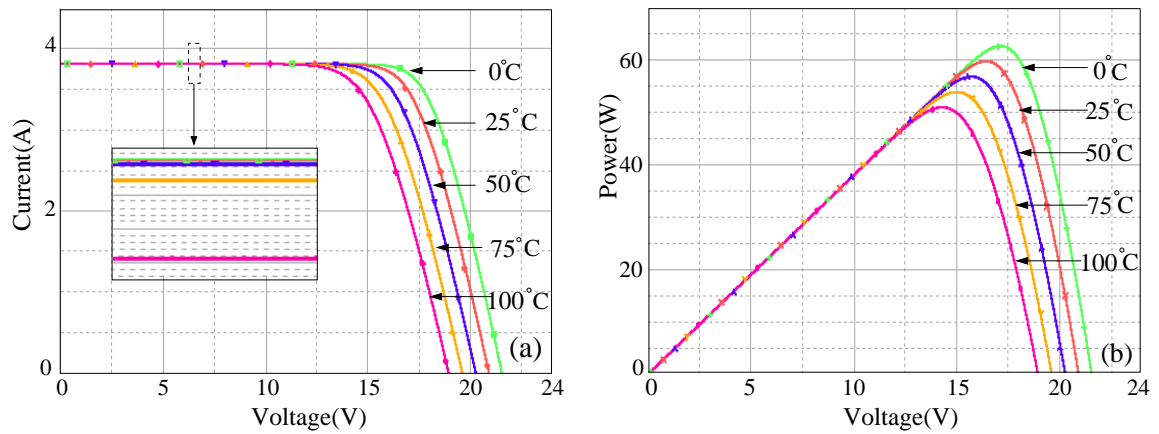


Figure 2.3: (a)  $i-v$  curve, and (b)  $p-v$  curve at different temperature level.

extract maximum power from the PV cell. The maximum power point (MPP) for a solar cell is given by

$$P_{\text{MPP}} = V_{\text{MPP}} \times I_{\text{MPP}} \quad (2.5)$$

where  $V_{\text{MPP}}$  and  $I_{\text{MPP}}$  are the voltage and current corresponding to MPP.

The PV panel parameters are given in Table 5.1. Figures 2.2 and 2.3 show the constitutive curves of a PV panel defined by (2.3) for various values of temperature and solar incident irradiance. Both the curve imply that during one day the maximum power point of a PV cell changes with change in solar irradiance and temperature.

## 2.2 DC-DC Converter Topologies

Grid-connected PV system with varying the solar irradiation, the voltage appeared across the PV panel may be higher or lower than the ac grid voltage. This leads to both step-up or step-down operation depending upon the input voltage. The dc-dc converters are used to performance the above operations. On the broad sense, these converters are classified into two topologies: a) isolated dc-dc converters [44], [45] and b) non-isolated converters [46], [47].

In the isolated converter, the output voltage can be controlled by using a transformer. However, a too large transformer will lead to a large leakage inductor. As a result, the voltage stress of the switch will be increased, whereas the efficiency of the converter is degraded [48], [49], [50]. Hence, the non-isolated converters are commonly used in the industries because of low conduction loss, simple structure with good response speed, and low cost [51]. So the conventional non-isolated dc-dc converters are used in this dissertation as dc power stage. Based on the relative magnitudes of supply and load voltages, dc-dc converters can be classified into three broad categories; buck converter, boost converter, and buck-boost converter.

### I. Buck Converter

The buck converter produces an output voltage which is always less than the input voltage. This converter is also known as the step-down converter. The buck converter with the resistive load is shown in Figure 2.4. For buck converter presented here is presumed that is working in continuous-conduction mode (CCM), i.e., the inductor current ( $i$ ) never falls to zero. The system consists of an input capacitor  $C$ , a diode  $D$ , a low pass filter with inductor  $L$ , and capacitor  $C_0$ , a controllable switch  $S$ , controlled by a MPPT controller, which will be discussed briefly later. The filter capacitor is assumed to be very high so that no current will flow through it. For an ideal switch, and the PV input voltage  $v$ , the instantaneous output  $v_0$  voltage depends upon the switch positions. The relationship between the input and output voltage can be expressed in terms of the switch duty ratio [45]

$$d = \frac{v_0}{v} = \frac{t_{\text{on}}}{T} \quad (2.6)$$

where  $t_{\text{on}}$  and  $T$  are the on time and the switching time period. The buck converter can be treated as a transformer where turn ratio is changed by changing the switch duty ratio  $d$ .

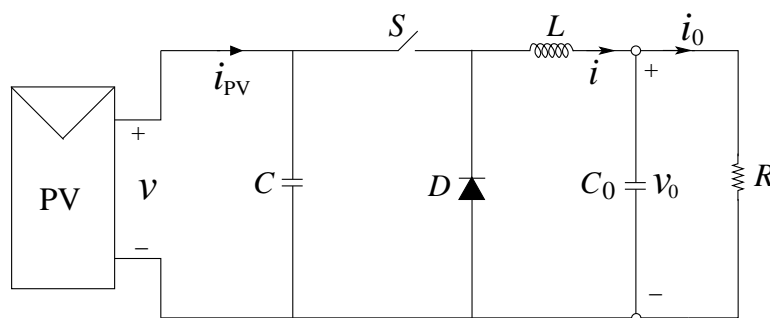


Figure 2.4: Buck converter for PV system.

The behavior of the circuit during on and off-state can be derived by applying the Kirchoff's laws. The equivalent circuits for the above two switching operations are shown in Figure 2.5. Here,  $u$  is the binary control pulses of the buck converter with duty-ratio  $d$ . During the on-state, when the switch  $S$  is closed as shown in Figure 2.5(a), the following set of differential equations describing the system's dynamical behavior are obtained as

$$\frac{dv}{dt} = \frac{i_{PV}}{C} - \frac{i}{C} \quad (2.7)$$

$$\frac{di}{dt} = \frac{v}{L} - \frac{v_0}{L} \quad (2.8)$$

$$\frac{dv_0}{dt} = \frac{i}{C_0} - \frac{v_0 - i_0}{C_0} \quad (2.9)$$

where  $i_0$  is the load current.

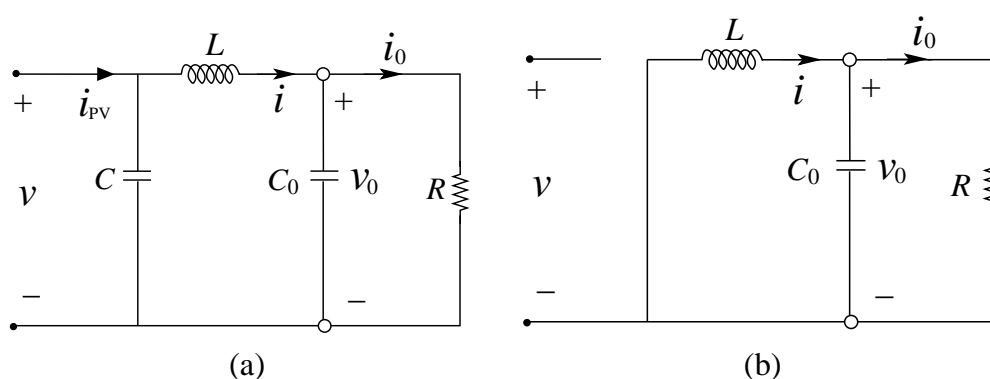


Figure 2.5: Buck converter circuit for (a) on-state, and (b) off-state operation in CCM.

During the off-state, when the switch  $S$  is opened as shown in Figure 2.5(b),

then

$$\frac{dv}{dt} = \frac{i_{PV}}{C} \quad (2.10)$$

$$\frac{di}{dt} = -\frac{v_0}{L} \quad (2.11)$$

$$\frac{dv_0}{dt} = \frac{i}{C_0} - \frac{v_0 - i_0}{C_0} \quad (2.12)$$

If  $u$  is the control signal for controlling the switch  $S$ , then (2.7)-(2.12) can be rewritten as

$$\frac{dv}{dt} = \frac{i_{PV}}{C} - \frac{i}{C}u \quad (2.13)$$

$$\frac{di}{dt} = \frac{v}{L}u - \frac{v_0}{L} \quad (2.14)$$

$$\frac{dv_0}{dt} = \frac{i}{C_0} - \frac{v_0 - i_0}{C_0} \quad (2.15)$$

The dynamics of the buck converter can be written in state space form as

$$\frac{dx}{dt} = f + gu \quad (2.16)$$

$$\text{where } x = \begin{bmatrix} v \\ i \\ v_0 \end{bmatrix}, f = \begin{bmatrix} \frac{i_{PV}}{C} \\ \frac{x_3}{L} \\ \frac{x_2}{C_0} - \frac{x_3 - i_0}{C_0} \end{bmatrix}, g = \begin{bmatrix} \frac{x_2}{C} \\ \frac{x_1}{L} \\ 0 \end{bmatrix}, \text{ and } u = \begin{bmatrix} 1 \\ 0 \end{bmatrix}.$$

A dc-dc buck converter and an MPPT control circuit are required to provide the controlled switching pulses to the converter so that it forces the operating point of the PV system close to the desired value.

## II. Boost Converter

The boost converters are commonly used to extract the maximum power from the PV array. These converters produce an output voltage which is higher than the input voltage. When the PV voltage is insufficient, the PV voltage can be boosted with the use of the boost converter. The basic circuit design of a boost converter is shown in Figure 2.6. The boost converter absorbs and supplies energy from PV array to the load with the help of four components which are an inductor, a controlled switch, a diode, and an output capacitor. The output voltage depends on the switch duty ratio. The relationship between the input and output voltage can be expressed as [45]

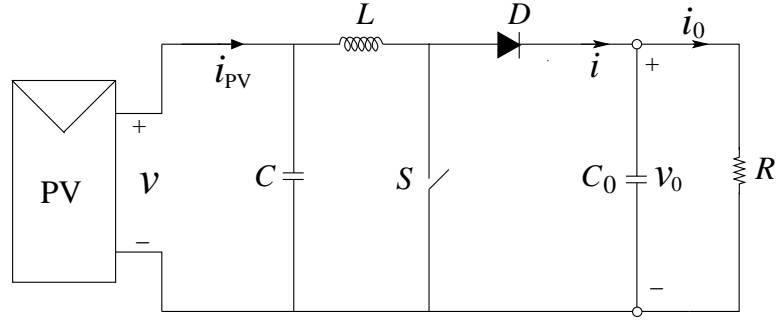


Figure 2.6: Boost converter for PV system.

$$\frac{v_0}{v} = \frac{t_{\text{on}}}{T} = \frac{1}{1-d} \quad (2.17)$$

where  $t_{\text{on}}$  and  $T$  are the on time and switching period respectively. The value of the inductor and the switching are selected in such a way that boost converter is operated in CCM.

The equivalent circuits of the buck converter for two switching operations (on and off-state) are shown in Figure 2.7. Here  $u$  is the binary control pulses of the boost converter with duty-ratio  $d$ . During the on-state, when the switch  $S$  is closed as shown in Figure 2.7(a), the following set of differential equations describing the system dynamical behavior are obtained as

$$\frac{dv}{dt} = \frac{i_{\text{PV}}}{C} - \frac{i}{C} \quad (2.18)$$

$$\frac{di}{dt} = \frac{v}{L} \quad (2.19)$$

$$\frac{dv_0}{dt} = -\frac{v_0 - i_0}{C_0} \quad (2.20)$$

where  $i_0$  is the load current.

During the off-state, when the switch  $S$  is opened as shown in Figure 2.7(b), then

$$\frac{dv}{dt} = \frac{i_{\text{PV}}}{C} - \frac{i}{C} \quad (2.21)$$

$$\frac{di}{dt} = \frac{v}{L} - \frac{v_0}{L} \quad (2.22)$$

$$\frac{dv_0}{dt} = \frac{i}{C_0} - \frac{v_0 - i_0}{C_0} \quad (2.23)$$

If  $u$  is the control signal for controlling the switch  $S$ , then (2.18) to (2.23) can

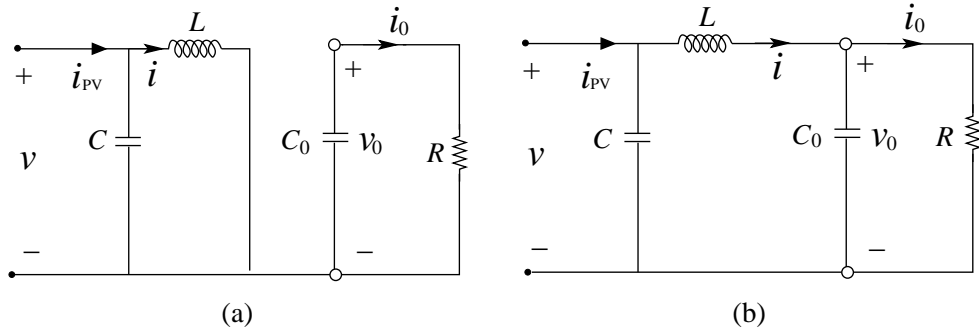


Figure 2.7: Boost converter circuit for (a) on-state, and (b) off-state operation in CCM.

be rewritten as

$$\frac{dv}{dt} = \frac{i_{PV}}{C} - \frac{i}{C} \quad (2.24)$$

$$\frac{di}{dt} = \frac{v}{L} - \frac{v_0}{L}(1-u) \quad (2.25)$$

$$\frac{dv_0}{dt} = \frac{i}{C_0}(1-u) - \frac{v_0 - i_0}{C_0} \quad (2.26)$$

The dynamics of the buck converter can be written in state space form as

$$\frac{dx}{dt} = f + gu \quad (2.27)$$

$$\text{where } x = \begin{bmatrix} v \\ i \\ v_0 \end{bmatrix}, f = \begin{bmatrix} \frac{i_{PV} - i}{C} \\ \frac{x_1 - x_3}{L} \\ \frac{x_2}{C_0} - \frac{x_3 - i_0}{C_0} \end{bmatrix}, g = \begin{bmatrix} 0 \\ \frac{x_3}{L} \\ \frac{x_2}{C_0} \end{bmatrix}, \text{ and } u = \begin{bmatrix} 1 \\ 0 \end{bmatrix}.$$

A dc-dc boost converter and a MPPT control circuit are required to provide the controlled switching pulses to the converter so that it forces the operating point of the PV system close to the desired value.

### III. Buck-Boost Converter

The buck-boost converter is capable of producing an output voltage, which is higher or lower voltages to the supply voltage. Several commonly used buck-boost converter topologies are reported in [52]. The output voltage across the load is controlled by continuously adjusting the duty ratio of the power switch as shown in Figure 2.8. In the steady state condition, the output voltage

of the buck-boost converter is given by [45]

$$\frac{v_0}{v} = \frac{d}{1-d} \quad (2.28)$$

where  $v_0$  is the average output voltage,  $v$  is the input PV voltage,  $d$  is the duty ratio of the power switch. Thus, the output voltage can be regulated to higher or lower than the source voltage through properly control the operating duty ratio for the power switch. The dynamics of the buck-boost converter can be derived

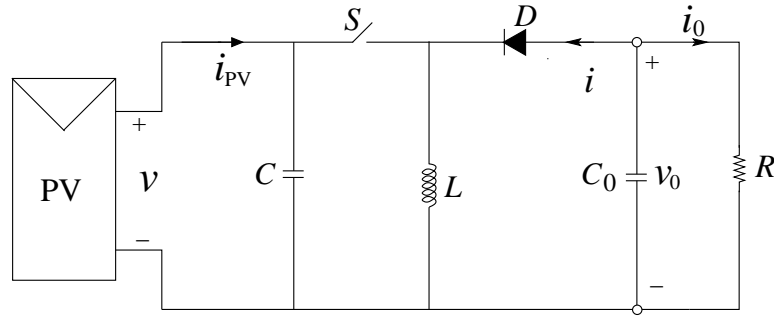


Figure 2.8: Buck-Boost converter for PV system.

in the state space form as

$$\frac{dx}{dt} = f + gu \quad (2.29)$$

$$\text{where } x = \begin{bmatrix} v \\ i \\ v_0 \end{bmatrix}, f = \begin{bmatrix} \frac{i_{PV}}{C} \\ \frac{x_3}{L} \\ \frac{-x_2}{C_0} - \frac{x_3 - i_0}{C_0} \end{bmatrix}, g = \begin{bmatrix} \frac{-x_2}{C} \\ \frac{x_1 - x_3}{L} \\ \frac{-x_2}{C_0} \end{bmatrix}, \text{ and } u = \begin{bmatrix} 1 \\ 0 \end{bmatrix}.$$

## 2.3 Reviews on MPP Tracker

In typical residential photovoltaic (PV) applications, PV systems are composed of a number of series-connected modules arranged in parallel, and they usually suffer from a current mismatch between different modules due to manufacturing variability, dirt accumulation, or partial shading of the array [53]. In this architecture, any source of cell current mismatch or nonuniform shading will cause the overall system output power to be reduced since the current in the string is limited by the weakest module. While modules used today typically employ bypass diodes that limit the negative



effect of partial shading and help protect the panels [54], it is still the case that shading effect has a significant negative impact on any solar PV installations. The module-integrated converter (MIC), the so called micro-converter concept has been exploited to address this problem by operating each module at its unique maximum power point (MPP) and providing separate dc-dc conversion for each module [55–57]. Through dc-dc converters, localized control of module current and voltage can be achieved, and each module can operate at its independent MPP to improve the energy extraction of the overall system.

However, designing a fast and robust PV MPP tracking (MPPT) controller (with high tracking efficiency) for such MIC is a challenging task for power electronics practitioners [58]. Over the past decades, many efforts have been devoted to this research area and reviews are available now on this subject [58–61] and references therein. In most of cases, investigations are primarily based on standard P&O algorithms, constant-frequency (CF) pulse-width modulated (PWM) operation, and small-signal averaging technique or transfer function based stability analysis. However, averaging is only an approximated procedure to obtain the low-frequency behavior of the actual switching model of the dc-dc converters. The averaged model was failed to predict many fast-scale instabilities (e.g., subharmonic oscillations and chaotic behavior) that may develop in the current and voltage waveform at clock frequency, causes high conduction loss and excessive switching stress [62]. This shortcoming is due to elimination of the discontinuous effect of the real converter system and ignoring the microscopic dynamics inside the switching cycle (see [63] and refs. therein) as well as the quantization effects [64], which is inherently induced in all digitally controlled MPPT systems [65]. Because of this approximation, the traditional use of averaging-based analysis technique and also P&O algorithm cannot always extract the best optimized performances in terms of fast and robust dynamic performances, steady-state oscillations, and tracking efficiency. The optimized performances of P&O based MPPT controller depend largely on amplitude and frequency of the perturbations applied to the switching converter [66]. It is therefore necessary to apply a more advanced controller as well as the fast-scale stability analysis technique (bifurcation analysis) in order to achieve such specific performances.

It has, however, been recently reported that dynamic responses of a MPP tracker can be improved by combining the different mode of controllers like sliding and constant-frequency PWM [67] or hysteresis controller [68–71] with relatively costly A/D and D/A converters. As a consequence of this combination, the sliding-mode controller (SMC) essentially utilizes a CF-switching (CFS) control law to force the state trajectory from any initial position onto a specified surface in the state space,

called the switching or sliding surface (SS), and maintain it on this surface for all subsequent time. The main features of the *ideal* sliding mode (SM) are the robustness against the parameters fluctuations. Despite these unique advantages of ideal one, the controllers reported earlier completely rely on smooth averaged models of the dc-dc switching converters and the control is only valid on a reduced-order SS. However, in real life power electronics converter systems, SM actually occurs not on its discontinuity surface, but within the vicinity of that discontinuity or within a boundary layer surrounded by multiple switching surfaces, like hysteresis control [68–71]. In such situation, the control components may take up values which are different from the equivalent control law, therefore, result in a richer set of motions on the sliding manifold [72]. The existence of a unique sliding motion can only be determined successfully using the notion of Utkin’s equivalent control or Filippov continuation method if the fast-scale dynamics is stable. The mathematical proof of this concept has already been developed earlier in multi-scale hybrid dynamical systems (HDSs) [73]. Since the switching converters used in PV systems come under this class of systems [63, 74], the equivalent equation of motion derived from Utkin’s theory may not be always successful to predict the existence of a unique solution or robustness. It can only be successfully used when the long-time averaging of fast-scale oscillations becomes zero, in other words, when the capacitor voltage and the inductor current waveforms during the steady-state operation are periodic in nature [73].

In view of this, this work proposes a fast and robust analog-MPP tracker [also called as analog sliding-mode controller (ASMC)] which is implemented and designed by using the concepts of Utkin’s equivalent control theory and fast-scale stability analysis. The main objectives of applying such concepts are to provide the control support for the MPPT system which are required for 1) guaranteed stability with high robustness against the parameters uncertainties, and 2) fast dynamic responses under rapidly varying environmental conditions. This cannot be met by conventional digital or analog MPPT controllers without continuously tuning the controller parameters and complex controller architecture [58, 75]. Thus, the choice of this analog solution is quite attractive because of its low cost and capability of easy integration with a normal dc-dc converter in integrated circuit (IC) form, so that plug-and-play operation for many low power residential PV applications [55, 76] can be easily achieved. Moreover, since the proposed analog controller inherently acts like a CF hysteresis controller [68, 69], it retains all of the properties of an *ideal* SMC, that is, simplicity in practical realization, good dynamic response with high robustness, and less overshoot in the output module voltage. In addition, it provides a relatively larger bandwidth to eliminate the low-frequency limit cycle oscillation [65], and reduces the cross-coupling

effects which is normally occurred in series-connected converters systems [77].

## 2.4 Module-Integrated Analog MPP Trackers

In this section, the architecture shown in Figure 2.9 is considered in order to introduce the proposed modular MPP trackers. It consists of two PV modules which are interconnected with two nonautonomous switching converters, and each of them comprising of an input capacitor  $C$ , a low-pass filter with inductor  $L$  and capacitor  $C_o$ , a diode  $D$ , and a controllable switch  $S$ , governed by an analog MPPT controller without imposing any external control or perturbation. The output of the dc-dc converters are connected in series and put in parallel to dc bus (input of a dc-ac converter), represented by means of a Thevenin model [70, 78]. Mathematically, the output voltage  $V_{\text{bus}}$  and corresponding throughput power  $P_o$  of such series-connected converters system can be expressed as a sum of all modular MPPT controllers [56, 79], such that

$$V_{\text{bus}} \approx \sum_{k=1}^2 v_o^k \quad \text{and} \quad P_o = i_o \sum_{k=1}^2 v_o^k; \quad \text{since} \quad R_{\text{eq}} \approx 0. \quad (2.30)$$

Here  $i_o$  is the averaged load current and  $v_o^k$  is the output voltage of the  $k$ -th dc-dc converter, which is dynamically coupled with other converters' output voltage. In a system like (2.30), every disturbance induced on the output voltage, by the other MPVSs and/or by the inverter, directly propagates on the modules' output voltage. This may lead to instability or dynamic performance degradation [77, 79, 80]. In [80], authors demonstrated that if the MPPT controller is fast enough, any disturbances in the closed-loop system do not significantly affect the operation of a single MPVS. This is also true for inverter system. Since fast controller with larger loop-gain has better output disturbance rejection capability than that of slower one [81], therefore it can avoid the propagation of low frequency perturbation to the PV module side (see ref. [82]). However, this mandatory requirement makes the achievement of a fast and stable controlled converter system (in terms of fast- and slow-scale stability) which is really a difficult task.

This paper thus promises to deal the complete stability analysis of proposed analog MPVS in order to achieve fast and robust dynamic responses. The system under this control logic is excellent in tracking effectiveness and rapid dynamic responses [83]. In addition, it inherently makes the MPP as an attractor of the system. Irrespective of any initial voltage, the controller always forces the system's state trajectories to

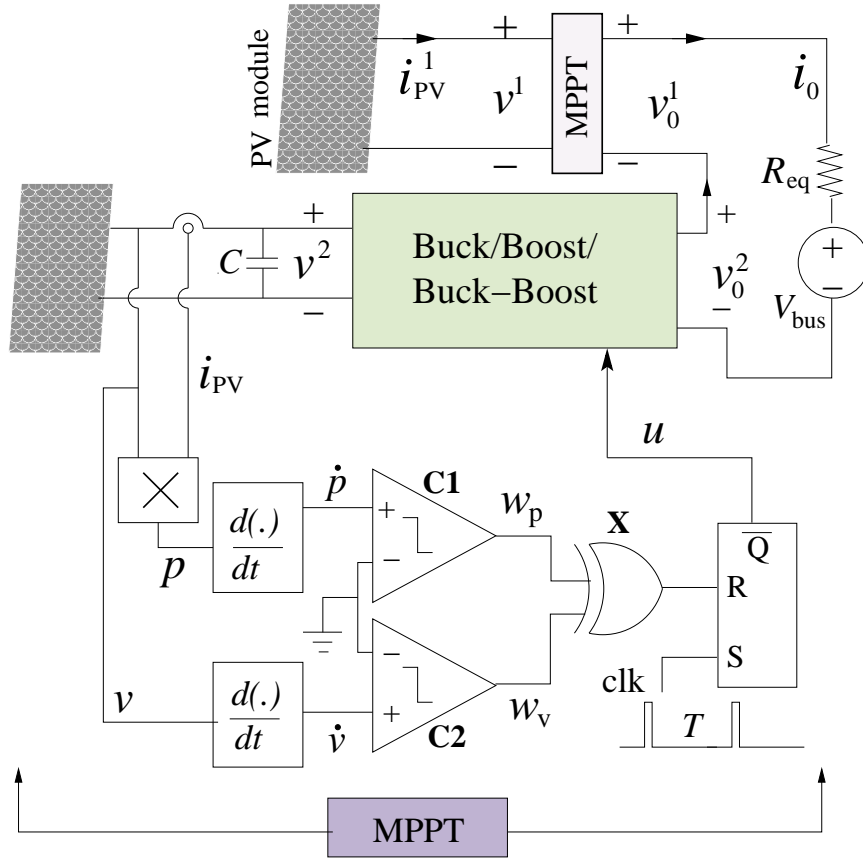


Figure 2.9: The schematic showing the series architecture with a string of two MPVS and zooming view of analog MPP tracker.

travel towards the MPP satisfying the conditions (see Figure 2.10):

$$\frac{\partial p}{\partial v} = \begin{cases} > 0 & \text{if } (v - V_{mpp}) < 0 \\ = 0 & \text{if } (v - V_{mpp}) = 0 \\ < 0 & \text{if } (v - V_{mpp}) > 0 \end{cases} \quad (2.31)$$

where  $v$  is the PV module output voltage,  $p$  is the module power, and  $V_{mpp}$  is the voltage corresponds to MPP  $P_{max}$ . The conditions (2.31) ensure that depending on the value of power gradient  $\partial p/\partial v$ , the voltage across the input capacitor  $v$  will be increased or decreased towards  $V_{mpp}$ . If  $v < V_{mpp}$ , then its rate of change should be positive. Otherwise, if  $v > V_{mpp}$ , then  $v$  is forced to fall and hence its rate change should be negative. But if  $v = V_{mpp}$ , the voltage  $v$  is held fixed. The rate of change of  $v$  should be zero. The simplest functional form that would confirm these objectives,

i.e.,

$$\frac{dv}{dt} = \begin{cases} > 0 & \text{if } (v - V_{\text{mpp}}) < 0 \\ = 0 & \text{if } (v - V_{\text{mpp}}) = 0 \\ < 0 & \text{if } (v - V_{\text{mpp}}) > 0 \end{cases} \quad (2.32)$$

can be expressed in terms of  $dv/dt$  as,

$$\frac{dv}{dt} = -\gamma(v - V_{\text{mpp}}) \quad (2.33)$$

where  $\gamma$  is the positive number associated with dynamic response of the controller [83]; the larger the  $\gamma$ , the faster the dynamic response <sup>1</sup>. The graphical representation of (2.33) is shown in Figure 2.10. It is observed that because (2.31) and (2.32) have similar forms, a simple control law can be deduced by making

$$\frac{dp}{dt} = \frac{\partial p}{\partial v} \frac{dv}{dt} \quad (2.34)$$

$$\dot{v} \propto \frac{\partial p}{\partial v} = \alpha \frac{\partial p}{\partial v} \quad (2.35)$$

where  $\alpha > 0$  is a constant. Now, after substituting (2.34) into expression (2.35) and using the switching logic (2.31) and (2.32), one can easily obtain the control law and the control algorithm which are given by

$$\frac{\partial p}{\partial v} = \dot{p}/\dot{v} \quad (2.36)$$

$$\begin{aligned} \dot{v} &= \alpha \dot{p} / \frac{\partial p}{\partial v} \\ &= \alpha \dot{p} / \dot{v} \end{aligned} \quad (2.37)$$

In practice, realization of such an algorithm  $\dot{v} = \alpha \dot{p} / \dot{v}$  is slightly difficult due to presence of an algebraic loop. Since  $v$  appears on both sides, it would manifest high frequency oscillation. One requires an analog divider circuit which is again undesirable. Moreover, divider circuit causes many other imperfect operations and even singularity problem when  $v$  becomes zero (in this case, it happens only when  $v = V_{\text{mpp}}$ ). While by rearranging the desired control algorithm into the form  $\dot{v}^2 = \alpha \dot{p}$  does not help either. In fact, squaring of  $v$  not only destroys the vital information of its sign, but also causes the singularity problem at MPP. In [83], authors showed that the problem of singularity can be resolved by redefining the above control law (2.36)

---

<sup>1</sup>However, any function complying with (2.32) would fulfill the objective of (2.31) and (2.32), which are indeed in similar forms.

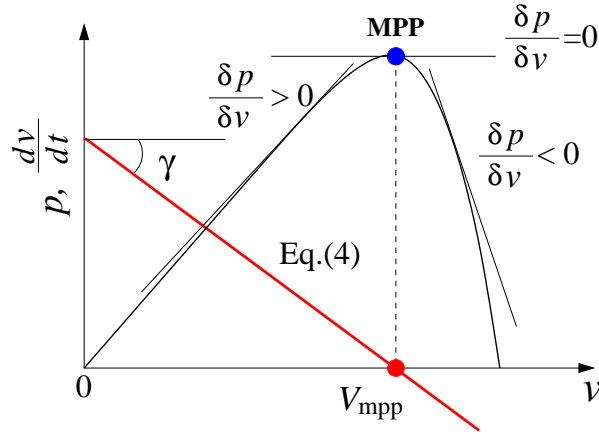


Figure 2.10: The representative characteristics of  $\dot{v}$  making  $V_{\text{mpp}}$  as an attractor.

as

$$\frac{\partial p}{\partial v} := \text{sign}(\dot{p}/\dot{v}) \equiv \frac{\text{sign}(\dot{p})}{\text{sign}(\dot{v})} \equiv \text{sign}(\dot{p})\text{sign}(\dot{v}) \quad (2.38)$$

$$\Rightarrow \text{sign}(\dot{v}) = \text{sign}(H) = \begin{cases} +1 & \text{if } H < 0 \\ -1 & \text{if } H > 0. \end{cases} \quad (2.39)$$

Here, the expressions (2.38)-(2.39) indicate that in spite of zero-division the nonlinear function  $\text{sign}(\cdot)/\text{sign}(\cdot)$  can be reformulated as a function of multiplication  $G(\cdot) = \text{sign}(\cdot)\text{sign}(\cdot)$  which are realized by a couple of comparators  $\mathbf{C}_1$ ,  $\mathbf{C}_2$  followed by an exclusive-OR gate  $\mathbf{X}$  [see Figure 2.9]. The comparators are used to evaluate the sign of  $G(\cdot)$  by producing binary signals ( $w_p, w_v$ ) whose value is 0 if  $\dot{p} < 0$  or 1 if  $\dot{p} > 0$ ; or, 0 if  $\dot{v} < 0$  or 1 if  $\dot{v} > 0$ . Multiplication of these binary signals using X-OR gate is further used to generate required switching signals of the control law (2.39). It essentially contains the information whether  $v$  should be increased or decreased to approach MPP. Since  $\text{sign}(\cdot)$  function in (2.39) has a discontinuity at the MPP, one cannot expect an equilibrium point at steady-state, rather the system dynamics is governed by very high switching frequency. This results in excessive switching losses and also reduces the life-time of the semiconductor devices.

Although such high switchings can be easily restricted by incorporating latch circuit into the controller, but its presence makes single discontinuity switching surface  $H$  into a CFS  $\Delta$ -neighborhood chatter box, or switching box  $S_B = \{v: V_{\text{mpp}} - \Delta \leq v < V_{\text{mpp}} + \Delta; t < T, \Delta > 0\}$ , surrounded by multiple SSs  $H = (v - V_{\text{mpp}})$  and external clock pulse having time period  $T$ . The switching flow diagram of such control algorithm is shown in Figure 2.11. It represents that depending on the initial value of the input capacitor voltage  $v(0)$ , MIC may operate into two modes: one when  $v$  is outside the

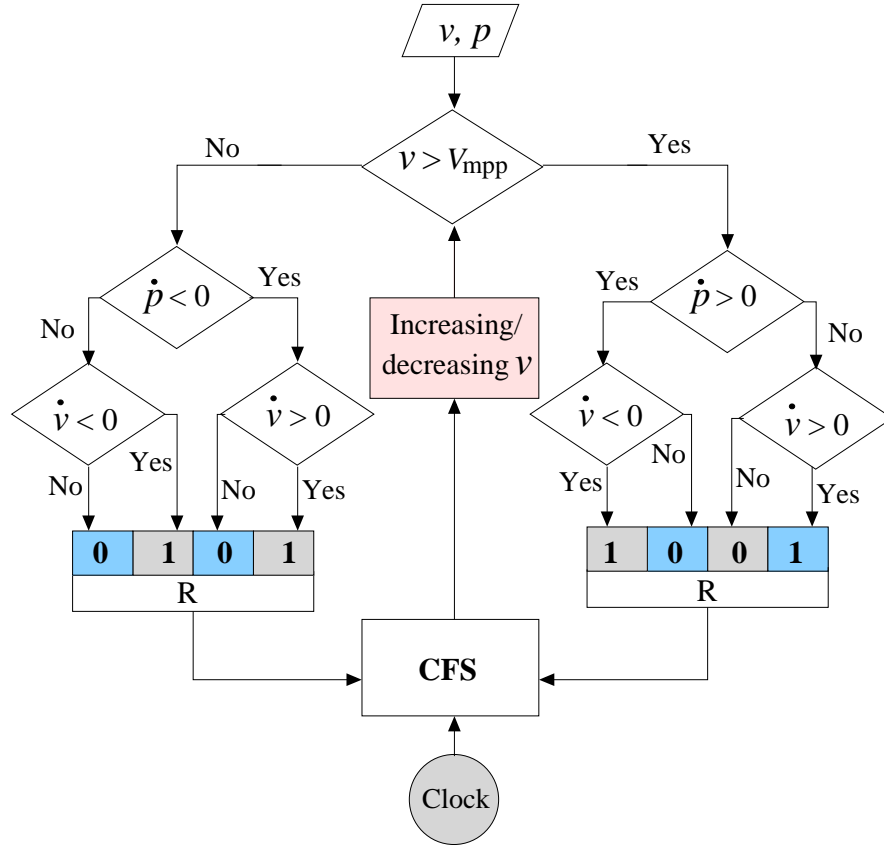


Figure 2.11: Switching flow diagram of proposed ASMC.

boundary layers and the other when it is inside. At the beginning of every clock pulse, we determine whether the capacitor voltage  $v_n = v|_{t=nT}$  ( $n$  is a positive integer number) is within the boundary of  $S_B$  or not. If it is inside, at start of the clock period,  $u = 0$ , i.e., the switch  $S$  is turned off, capacitor voltage  $v$  raises. When  $v$  reaches a peak value  $V_{mpp}$ ,  $u = 1$ , i.e., the  $S$  is turned on. The input voltage  $v$  then starts falling and follows the same dynamics until next clock pulse is arrived. While, if  $v_n$  is outside of  $S_B$ , the switch  $S$  is turned on when  $V_{mpp} < v_n$  and turned off when  $v_n < V_{mpp}$ .

Hence, for an arbitrary initial position the controller

$$u = \begin{cases} 1 & H < 0 \\ 0 & H > 0 \end{cases} \text{ if } v \text{ is outside} \quad (2.40)$$

$$u_{eq} \text{ if } v \text{ is inside}$$

drives the trajectories to reach into  $S_B$  in finite time  $t_s > 0$ . Once they reach, a hysteretic flow inside the switching box starts, and an equivalent motion continues to move toward the steady-state periodic orbit rather than equilibrium point. The

Table 2.1: Specification of ASMC based modular PV system for  $G = 1000 \text{ W/m}^2$ , and  $T_c = 25^\circ\text{C}$

Converter	PV array
$L = 1.0 \text{ mH}$ , $C = 100 \text{ } \mu\text{F}$ ,	$I_{sc} = 3.8 \text{ A}$ , $V_{oc} = 21.1 \text{ V}$ ,
$C_0 = 1000 \text{ } \mu\text{F}$	$K_V = -0.80 \text{ V/K}$ , $K_I = 0.0065 \text{ A/K}$
$T = 20 \text{ } \mu\text{s}$	$V_{mpp} = 17.1 \text{ V}$ , and $I_{mpp} = 3.5 \text{ A}$ .

representative diagram of (2.40) and corresponding hysteretic flow of the buck-type switching converter, for example, is shown in Figure 2.12.

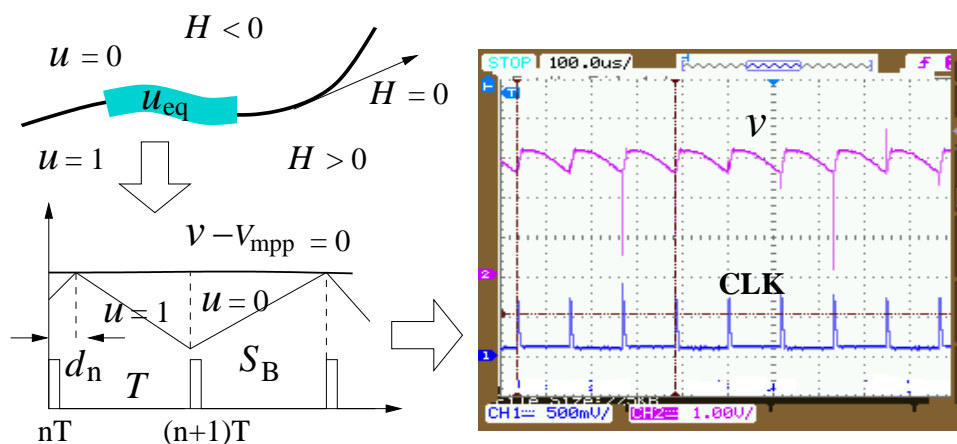


Figure 2.12: Hysteretic flow of buck-type MIC for  $i_o = 4.8\text{A}$ . The other parameters value used are given in Table 5.1.

## 2.5 Sliding-Mode Controlled MPVS

In the past, it has been reported that the equivalent motion of HDSs (characterized by piecewise smooth system with right-hand side discontinuities) can be determined successfully by using the notion of Utkin's equivalent control or Filippov continuation method [72]. For a single discontinuous SS there exists a unique solution of equivalent dynamics and the sliding motion obtained from these methods are the same. However with boundary layers control (2.40), the sliding motion inside the chattered-box only



Table 2.2: Dynamics of all three MIC architectures and their representation in the form of:  $\frac{dx}{dt} = f + gu$ , where  $x = [v \ i \ v_o]^T$

Buck converter	Boost converter	Buck-boost converter
$\dot{x}_1 = \frac{i_{pv}(x_1)}{C} - \frac{x_2}{C}u$ $\dot{x}_2 = \frac{x_1}{L}u - \frac{x_3}{L}$ $\dot{x}_3 = \frac{x_2}{C_0} - \frac{x_3 - i_o}{C_0}$	$\dot{x}_1 = \frac{i_{pv}(x_1)}{C} - \frac{x_2}{C}$ $\dot{x}_2 = \frac{x_1}{L} - \frac{x_3}{L}(1-u)$ $\dot{x}_3 = \frac{x_2}{C_0}(1-u) - \frac{x_3 - i_o}{C_0}$	$\dot{x}_1 = \frac{i_{pv}(x_1)}{C} - \frac{x_2}{C}u$ $\dot{x}_2 = \frac{x_1}{L}u + \frac{x_3}{L}(1-u)$ $\dot{x}_3 = \frac{x_2}{C_0}(u-1) - \frac{x_3 - i_o}{C_0}$
$f = \begin{bmatrix} \frac{i_{pv}(x_1)}{C} \\ \frac{x_3}{L} \\ \frac{x_2}{C_0} - \frac{x_3 - i_o}{C_0} \end{bmatrix}, \quad g = \begin{bmatrix} \frac{x_2}{C} \\ \frac{x_1}{L} \\ 0 \end{bmatrix}$	$f = \begin{bmatrix} \frac{i_{pv}(x_1) - x_2}{C} \\ \frac{x_1 - x_3}{L} \\ \frac{x_2}{C_0} - \frac{x_3 - i_o}{C_0} \end{bmatrix}, \quad g = \begin{bmatrix} 0 \\ \frac{x_3}{L} \\ \frac{x_2}{C_0} \end{bmatrix}$	$f = \begin{bmatrix} \frac{i_{pv}(x_1)}{C} \\ \frac{x_3}{L} \\ -\frac{x_2}{C_0} - \frac{x_3 - i_o}{C_0} \end{bmatrix}, \quad g = \begin{bmatrix} -\frac{x_2}{C} \\ \frac{x_1 - x_3}{L} \\ -\frac{x_2}{C_0} \end{bmatrix}$

exists when the fast-scale dynamics is stable [63, 73]. In this case, when the fast-scale oscillations of the input capacitor voltage ripple inside  $S_B$  are periodic.

### 2.5.1 Existence Conditions Under Ideal Switching Surface

Based on the aforementioned concepts, the analysis and design of proposed MPVS are investigated. The investigations are performed on the basis of full-order state-space model of MIC system [77, 78] and an ideal SSs  $H := \partial p / \partial v = 0$  (where  $\Delta \rightarrow 0$ ). From dynamical system point of view, MICs operating in continuous-conduction-mode (CCM) can be characterized by sets of 3-dimensional (3-D) differential-algebraic-equations (DAEs) with right-hand side discontinuity (for detail see Table 2.2) as

$$\frac{dx}{dt} = f + gu = \begin{cases} f_1 & \forall u = 0 \\ f_2 & \forall u = 1 \end{cases} \quad (2.41)$$

where  $u$  is the discontinuous control signal governed by (2.40). While the nonlinear PV array current  $i_{pv}(x_1)$  is defined as

$$i_{pv}(x_1) = I_{sc} - I_{sat} [\exp(x_1/aV_T) - 1] \quad (2.42)$$

with panel saturation and short-circuit current  $I_{\text{sat}}$  and  $I_{\text{sc}}$ , diode ideality constant  $a$ , and thermal voltage  $V_T$  with series and parallel resistance  $r_s \approx 0$ ,  $r_p \approx \infty$ , respectively. Having obtained the system description (2.41), next step is to design the controller, so that, control law  $u$  will direct the state trajectory towards the desired operation. In this case, it is appropriate to have a SMC law (2.40) that will adopt the switching function  $H$ , defined by

$$H := \frac{\partial p}{\partial x_1} = i_{\text{pv}}(x_1) - \frac{x_1 I_{\text{sat}}}{aV_T} \exp\left(\frac{x_1}{aV_T}\right) = 0. \quad (2.43)$$

The objective is that, from any arbitrary initial position  $x(0)$ , it will drive the system trajectory on either side of the SS  $H = 0$ . The trajectory is said to be in sliding mode if the motion within the vicinity of  $H$  is maintained and consequently directed towards the steady-state equilibrium point. In other words, it can also be stated that SMC is performing its control decision by utilizing the sliding plane  $H = 0$  as a reference path, on which trajectory will be attracted and eventually converged towards the equilibrium to achieve the desired steady-state operation satisfying the inequality conditions:

$$\lim_{H \rightarrow 0^+} \frac{dH}{dt} < 0, \quad \text{and} \quad \lim_{H \rightarrow 0^-} \frac{dH}{dt} > 0. \quad (2.44)$$

The conditions (2.44) are known as the SM reachability or existence conditions [69,84]. For an ideal SM-controlled MICs, these conditions can be easily derived from the time derivative of SS  $\frac{dH}{dt} = \nabla H \frac{dx}{dt}$  and then substituting this value into (2.44). From (2.43),  $\nabla H$  can be evaluated as

$$\nabla H = \left[ x_1 \frac{\partial^2 i_{\text{pv}}}{\partial x_1^2} + 2 \frac{\partial i_{\text{pv}}}{\partial x_1} \quad 0 \quad 0 \right] = [F(x_1) \quad 0 \quad 0]$$

where

$$F(x_1) = \left[ -\frac{I_{\text{sat}}(2aV_T + x_1)}{(aV_T)^2} \exp\left(\frac{x_1}{aV_T}\right) \quad 0 \quad 0 \right]$$

is only a function of PV module voltage with nonzero steady-state value. Substituting it into (2.44), and using (2.41) and (2.43) one can easily obtain the boundary conditions for both buck and buck-boost converters as

$$\mathbf{\Pi}_1 := i_{\text{pv}} - x_2 < 0; \quad \text{and} \quad \mathbf{\Pi}_2 := i_{\text{pv}} > 0. \quad (2.45)$$

While for boost converter, it can be obtained as

$$\mathbf{\Pi}_1 := i_{\text{pv}} - x_2 < 0; \quad \text{and} \quad \mathbf{\Pi}_2 := i_{\text{pv}} - x_2 > 0. \quad (2.46)$$

The conditions (2.45)-(2.46) are essentially interpreted as a region, requirement for the system trajectories to be oriented towards the sliding surface  $H$  from both

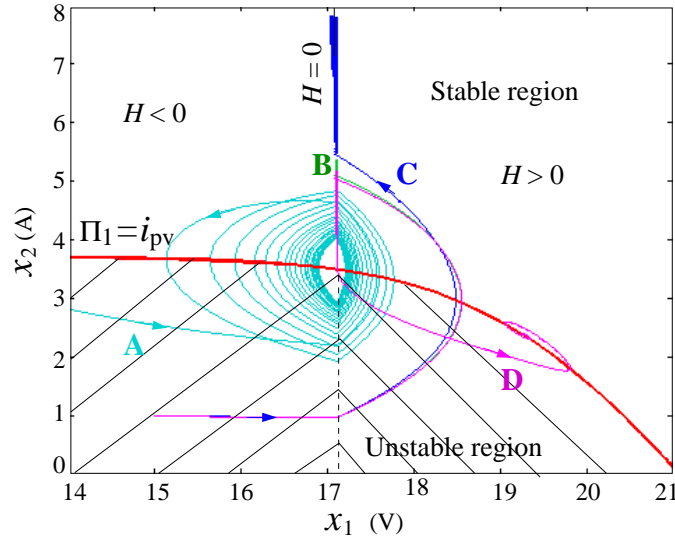


Figure 2.13: Trajectory evolution of ASMC-based MPVS showing the switching and sliding motion for  $G = 1000 \text{ W/m}^2$ ,  $T_c = 25^\circ \text{ C}$ , and  $i_o = 4.8 \text{ A}$ . The other parameters value used are given in Table 5.1.

sides. It is called as a stable region. In that region two vector fields  $f_1$  and  $f_2$  of (2.41) are pushing in opposite directions, so that states of the system  $x$  are forced to stay on the boundary and slide on it. While in case of an unstable region (i.e., if (2.45) or (2.46) does not satisfy) there will be a switching. The trajectories in one state-space region  $H < 0$  approaching transversely the switching boundary  $H = 0$ , cross it and enter into the adjacent region  $H > 0$ . The representative diagram of all possible trajectory evolutions of three switching converters is shown in Figure 2.13. It is important to note that, due to lack an existence region of the boost converter (2.46), trajectory (denoted by **A**) starting from any initial position travels towards the equilibrium point. Around that point, it starts oscillating in between two neighboring state-space regions with low frequency switchings and slightly high ripple magnitude. It can, however, be greatly improved by directly sensing of the inductor current (see trajectory **A** of Figure 2.13). As discussed in [85], MPPT technique employing SMC is generally more stable and robust when inductor current and input capacitor voltage are considered as the state variables. Based on this concept and redefining SS as  $H := \frac{\partial p}{\partial x_1} = x_2$ , the boundary conditions for such region  $\Pi$  derived from (2.41) and (2.44) can be defined as

$$\Pi_1 := x_1 > 0 \quad \text{and} \quad \Pi_2 := x_1 - x_3 < 0 \quad (2.47)$$

which is larger than that of region (2.46). While in case of buck and buck-boost

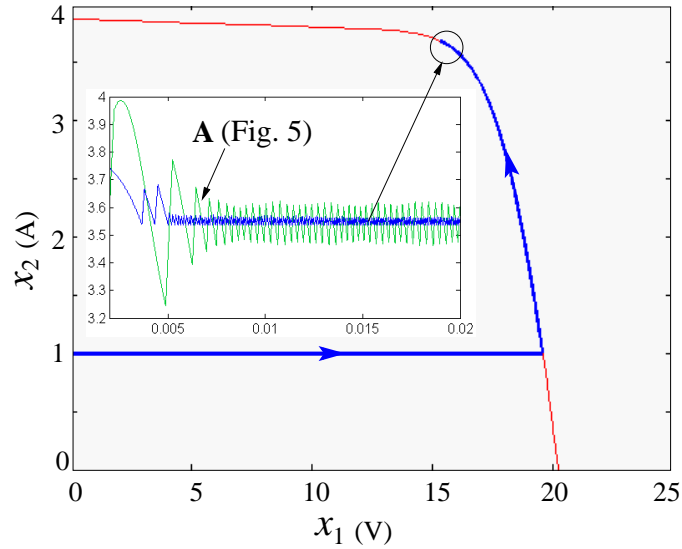


Figure 2.14: Performances of boost-type MIC under enhanced existence region  $\mathbf{\Pi}$  (represented by shadowed region). The parameters value are:  $L = 140 \text{ mH}$ ,  $C = 0.1 \text{ } \mu\text{F}$ , and  $i_o = 2.3 \text{ A}$ .

converters, trajectories **B** and **C** (denoted by green and blue curves) without satisfying (2.45), are intersecting the SS  $H = 0$  in finite time. Once they satisfy, just after the first intersection sliding motion starts and trajectories **B** and **C** continue to move towards the equilibrium points. The solution of each motion is unique if switching frequency  $f_s$  inside the chatter-box is ideally infinity. However, since in reality, such assumption is not true, the equivalent dynamics of motion derived from Utkin’s theory may not be always successful to predict the existence of a unique solution [73]. As reported before, it can only be successfully used if the long time average value of fast-scale oscillation is zero or the MIC systems are stable in fast time-scale.

## 2.5.2 Prediction of Fast-scale Stability Margin

In order to investigate such dynamics of MPVS, it is necessary to estimate the fast-scale stability margin at clock speed. It is also necessary to estimate the range of tunable or external parameters that will ensure without onset of chaos. The stability analysis using “complete one cycle fundamental solution matrix” — called monodromy matrix was addressed earlier, to solve this problem [86]. In this approach, the stability of a periodic orbit is determined by using the state transition matrices for the segments of the orbits lying in the individual subsystems, and the transition matrices across the switching — called saltation matrix. Once the monodromy matrix is obtained,

the eigenvalues of that matrix determine the stability of the periodic orbit to small perturbation.

To apply this concept, we derive an approximate chattered dynamics inside the switching box  $S_B$  by successively linearizing (2.42) around the MPP as

$$i_{\text{pv}} = I_{\text{mpp}} - \beta (x_1 - V_{\text{mpp}}) \quad (2.48)$$

and

$$\beta = \left. \frac{di_{\text{pv}}}{dx_1} \right|_{x_1=V_{\text{mpp}}} \approx \frac{I_{\text{mpp}}}{V_{\text{mpp}}} \quad (2.49)$$

And then, substituting it into (2.41) to form a set of 2-D linear time-invariant (LTI) subsystems <sup>2</sup> as

$$\frac{dx}{dt} = \begin{cases} M_1 : A_1 x + B_1 & \forall nT < t < d_n T + nT \\ M_2 : A_2 x + B_2 & \forall d_n T + nT < t < (1+n)T \end{cases} \quad (2.50)$$

where  $d_n$  is the steady-state duty ratio (see Figure 2.12), and  $A_i$  and  $B_i$  are the corresponding system and input matrices respectively, as shown in Table 2.3. Having obtained (2.50) if one assumes  $t = nT$  is a switching instant, then the monodromy matrix over complete one cycle  $T$  can be expressed as the composition of state transition matrices over the two phases of evolutions  $M_1$  and  $M_2$ , and two saltation matrices for the switching from  $M_1$  to  $M_2$  ( $\mathbf{S}_1$ ) and back to  $M_1$  ( $\mathbf{S}_2$ ) as [86]:

$$\mathbf{M} = \mathbf{S}_2 \Phi_2 \mathbf{S}_1 \Phi_1 \quad (2.51)$$

where  $\Phi_1 = e^{A_1 d_n T}$  and  $\Phi_2 = e^{A_1 (1-d_n) T}$  are the state transition matrices.  $\mathbf{S}_1$  and  $\mathbf{S}_2$  are the saltation matrices represented by

$$\mathbf{S}_1 = \mathbf{I} + \left. \frac{[(A_2 - A_1)x + (B_2 - B_1)] \nabla H}{\nabla H(A_1 x + B_1) + \frac{dH}{dt}} \right|_{t=d_n T}, \quad (2.52)$$

and  $\mathbf{S}_2 = \mathbf{I}$ , an identity matrix. However, to evaluate such matrices one needs to know the duty ratio  $d$  and corresponding state vectors at the switching instant  $t^* = d_n T$ . This can be accurately obtained by using the Newton-Raphson method. Alternatively one can use any standard simulator to obtain the stable behavior, from which the information about both  $d_n$  and  $x^*|_{t=d_n T}$  can be extracted. However,

---

<sup>2</sup>Since in local neighborhood of MPP the chattered dynamics is much faster than  $x_3$ , it is therefore reasonable to consider  $x_3 = V_o$  and  $dx_3/dt = 0$ .

Table 2.3: System and input matrices  $A_i$  and  $B_i$ 

Buck : $A_1 =$	$\begin{bmatrix} \frac{-\beta}{C} & 0 \\ 0 & 0 \end{bmatrix}$	, $A_2 =$	$\begin{bmatrix} \frac{-\beta}{C} & -1 \\ \frac{1}{L} & 0 \end{bmatrix}$	, $B_1 = B_2 =$	$\begin{bmatrix} \frac{2I_{\text{mpp}}}{C} \\ -\frac{V_o}{L} \end{bmatrix}$
Boost : $A_1 = A_2 =$	$\begin{bmatrix} \frac{-\beta}{C} & \frac{-1}{C} \\ \frac{1}{L} & 0 \end{bmatrix}$	, $B_1 =$	$\begin{bmatrix} \frac{2I_{\text{mpp}}}{C} \\ -\frac{V_o}{L} \end{bmatrix}$	, $B_2 =$	$\begin{bmatrix} \frac{2I_{\text{mpp}}}{C} \\ 0 \end{bmatrix}$
Buck-boost : $A_1 =$	$\begin{bmatrix} \frac{-\beta}{C} & 0 \\ 0 & 0 \end{bmatrix}$	, $A_2 =$	$\begin{bmatrix} \frac{-\beta}{C} & \frac{-1}{C} \\ \frac{1}{L} & 0 \end{bmatrix}$	, $B_1 =$	$\begin{bmatrix} \frac{2I_{\text{mpp}}}{C} \\ \frac{V_o}{L} \end{bmatrix}$
$B_2 = \left[ \frac{2I_{\text{mpp}}}{C} \quad 0 \right]^T$					

from aforementioned LTI state-space representation the duty-ratio information can be extracted easily by solving  $M_1$ , as

$$d_n = \underbrace{\frac{C}{\beta T} \ln(1 + \Delta x_1)}_{\text{buck and buck-boost}}, \text{ and } d_n = \underbrace{\frac{C}{\beta T} \frac{\Delta x_1}{(1 - x_2^*/I_{\text{mpp}})}}_{\text{boost}}; T \ll 1 \quad (2.53)$$

where  $x_2^*$  is the lower limit of steady-state inductor current,  $\Delta x_1 = (V_{\text{mpp}} - x_{1n})/V_{\text{mpp}}$  is the normalized input capacitor ripple with  $x_1^* = V_{\text{mpp}}$ , and  $x_1|_{t=nT} = x_{1n}$ . While in calculating  $\mathbf{S}_1$ , the switching function is  $H = x_1 - V_{\text{mpp}}$ , so that the normal is  $\nabla H = [1 \ 0]$  and the time derivative is  $dH/dt = 0$ . Substituting these expressions into (2.52), we obtain the saltation matrix of buck converter

$$\mathbf{S}_1^{\text{buck}} = \begin{bmatrix} 1 - x_2^*/I_{\text{mpp}} & 0 \\ C/\beta L & 1 \end{bmatrix}. \quad (2.54)$$

Similarly, for boost and buck-boost converters it can be easily evaluated as

$$\mathbf{S}_1^{\text{boost}} = \begin{bmatrix} 1 & 0 \\ 0 & 1/(1-D) \end{bmatrix} \quad (2.55)$$

and

$$\mathbf{S}_1^{\text{buck-boost}} = \begin{bmatrix} 1 - x_2^*/I_{\text{mpp}} & 0 \\ C(1-D)/\beta L & 1 \end{bmatrix} \quad (2.56)$$

where  $D = V_0/V_{\text{mpp}}$ . Once the salutation matrix and corresponding duty-ratios are known, one can easily calculate the monodromy matrix from (2.51). The monodromy matrix represents the linearized system integrated around the periodic orbits and hence, its eigenvalues

$$\lambda_{1,2} = \|\mathbf{M}\| \quad (2.57)$$

represent the Floquet multipliers. If they lie within the unit circle (i.e.,  $\lambda_{1,2} < 1$ ), the orbit is stable and that can be ensured as follows.

### 2.5.3 Design Guidelines

Here  $\Delta x_1$  and  $\beta$  are the known parameters and their exact values can be substituted directly into (2.53) for inspection. However, for designing the circuit parameters such as  $C$ ,  $L$ , and  $T$ , it is necessary to consider their maximum or minimum values for ensuring the abidance of nominal period-1 operation. Since at nominal operation  $\Delta x_1 \ll 1$  is always held, therefore baseline design guideline for choosing such  $C$  and  $T$  should be  $C/\beta T \gg 1$ , preferably be in the hundred. However  $T$  should not be chosen too high to avoid undesirable high frequency artifacts such as switching noise that may cause interfere with controller. In such situation,  $C$  may be used in conjunction with  $T$  to achieve a large value of  $C/\beta T$ , so that the condition  $d_n := \frac{C}{\beta T} \ln(1 + \Delta x_1) < 1$  is satisfied. While in case of  $L$ , one should choose its value sufficiently large in order to ensure the CCM operation (i.e.,  $x_2^* > 0$ ) and the stability condition (2.57). Based on the above guidelines, we select all the components value and investigate the dynamic behavior of the MIC by calculating  $d_n$  and  $\mathbf{S}_1$ , thereby the  $\lambda_{1,2}$  of the monodromy matrix. It is found that (say, for buck converter)  $d_n$  just before the instability at  $T \approx 59 \mu\text{s}$  is 0.3711, and corresponding eigenvalues are  $-0.9941$  and  $0.3692$  — implies the orbit is stable, and that is closely matched with the numerically obtained bifurcation diagram as shown in Figure 2.15. It also shows that for a low value of  $T$ , the system exhibits stable period-1 orbit. However, as the value of  $T$  increases, it becomes unstable at  $T \approx 60\mu\text{s}$  through a smooth period-doubling bifurcation. For

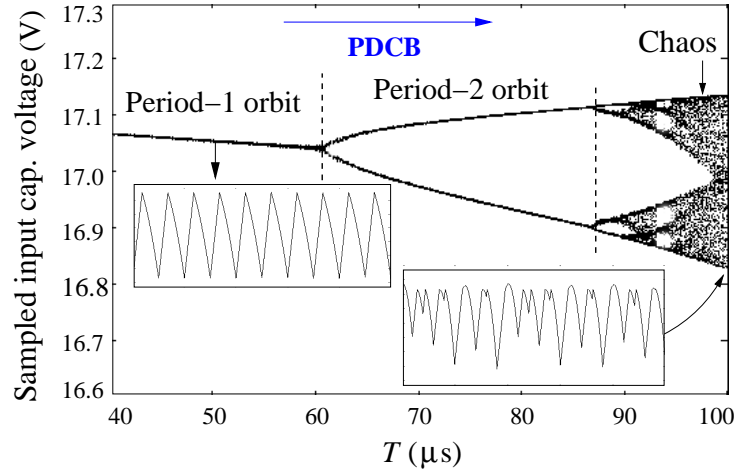


Figure 2.15: Representative bifurcation diagram showing the fast-scale instabilities of buck-type MIC for  $L = 140 \mu\text{H}$ ,  $C = 1000 \mu\text{F}$ , and  $i_o = 5.45 \text{ A}$ . Here  $T$  is taken as the bifurcation parameter.

further increment of clock period  $T$ , period-2 orbit bifurcates again, and finally leads to a chaotic orbit through a series of period-doubling-cascade bifurcation (PDCB) in close succession — where the application of Utkin’s equivalent control theory is not valid [73]. Moreover, it is important to note that, although such control concept is applicable for high periodic orbits, but it needs a multi-parametric bifurcation diagram to ensure the domain of existence of a periodic operation, which is again undesirable. Therefore, we only consider the period-1 mode of operation for safe operating condition, and that can be explicitly obtained from (2.53)-(2.57). In such situation, Filippov’s method and Utkin’s equivalent control concept can be successfully used to derive the equivalent dynamics of the motion. The idea behind such concepts is that in the vicinity of the sliding surface the velocity vector is always tangential to the sliding surface and the resulting equivalent dynamics of (2.41) is only governed by a smooth control law without any discontinuity [72].

#### 2.5.4 Equivalent SMC and Dynamics of Equivalent Motion

Based on this principle, the equivalent dynamics can be determined by replacing the discontinuous control  $u \in (0, 1)$  to an equivalent continuous one  $u_{\text{eq}}$ , which is derived from  $\frac{dH}{dt} = 0$  as

$$u_{\text{eq}} = -[\nabla H g]^{-1} \nabla H f$$



where  $\nabla Hg$  is the nonsingular square matrix. After substituting  $u_{eq}$  into (2.41), the equivalent dynamics of buck, boost, and buck-boost converters are obtained as

$$\frac{dx}{dt} = \begin{cases} \left[ \begin{array}{cc} 0 & \frac{x_1 i_{pv} - x_2 x_3}{x_2 L} \quad \frac{x_2 - i_0}{C_o} \end{array} \right]^T \\ \left[ \begin{array}{ccc} \frac{i_{pv} - x_2}{C} & 0 & \frac{x_1 x_2 - x_3 i_o}{x_3 C_o} \end{array} \right]^T \\ \left[ \begin{array}{cc} 0 & \frac{i_{pv}(x_1 - x_3)}{x_2 L} + \frac{x_3}{L} \quad \frac{i_{pv} - x_2 - i_0}{C_o} \end{array} \right]^T \end{cases} \quad (2.58)$$

which is a nonlinear function of  $x_1$ . Once there is a nonlinearity, there may exist more number of feasible equilibrium points and system may converge to some undesirable operating points. For example, see curve **D** of Figure 2.13. Theoretically, such equilibrium points and their domain of attractions could be successfully eliminated by properly designing the MPVSs, and also identifying their stable operating regions using stable- and unstable manifolds-based large-signal stability analysis [87]. This paper however deals to design the system by satisfying existence condition (2.45). It is found that if the equivalent sliding motion inside the stable region, does not cross the limiting boundary  $\Pi_1 = i_{pv}$  as  $t \rightarrow \infty$  (i.e., if the existence condition is not violated), then the system is stable. This can occur only when inductor current  $x_2$  (for buck converter load current  $i_o$ ) becomes just greater than that of the MPP current  $I_{mpp} = i_{pv}|_{mpp}$ , i.e.,

$$\mathbf{\Pi} : x_2 \geq I_{mpp}. \quad (2.59)$$

The condition (2.59) is quite general and true for all switching converters, when there exists a finite existence region defined by (2.45) and (2.46). However, due to different converters' topological configurations and switching function formulation, the stability region satisfying the aforementioned existence condition may also vary. For instance, the buck converters are conditionally stable and that stability region (also called MPP region [56]) is strongly limited by their minimum loading condition  $I_o = I_{mpp}$ . This can also be verified by solving (2.58) as  $(X_2/i_{pv})|_{mpp} = (X_1/X_3) > I_{mpp}$ , where  $X = [X_1 \ X_2 \ X_3]^T$  are steady-state equilibrium point. Although such limitation can be solved by using buck-boost converters (since  $I_{mpp} < X_2 := (1 - X_1/X_3) i_{pv} < I_{mpp}$ ), but they requires extra hardware circuitries to invert their output voltages. While the main disadvantages of noninverting buck-boost topology are the increased number of controllable switches and inductors [56], more complex control solution [71], and the achievable conversion efficiency, which is typically lower than the buck or boost converter for the same rating. In contrast, the boost converter is an attractive choice

because of its ability to increase the output voltage (requiring fewer panels for a given desired output voltage), but main disadvantage is its limited operating region. The output current of boost converter can never be higher than the input current, the range over which current mismatch can be addressed is severely limited [53, 55, 88]. Regardless of the control algorithms used it is always true for boost converters, and it can also be easily validated from reduced-order dynamics (2.58) as  $X_2 = (X_3/X_1)I_o \leq I_o$ , where  $X_2|_{\text{mpp}} := I_{\text{mpp}}$ .

Therefore, it can be concluded that the aforementioned concepts provide a simple way for the circuit designer to select the parameters for successful operation of ASMC. Given certain specifications, the designer would first roughly set the range of circuit parameters and load in a conventional way based on (2.58). This gives the desired slow time-scale stability and transient performance, but will not guarantee that the system will be stable on a fast time-scale. In order to ensure the nominal period-1 operation, it will be necessary to calculate the range of storage elements and switching frequency for which the period-1 orbit will remain stable. The designer will have to ensure that the circuit parameters simultaneously satisfy the conditions (2.57) and (2.59). Once it is satisfied, the equivalent motion (2.58) always exists and solution of that motion is unique.

## 2.6 Performance Analysis and Its Experimental Validation

### 2.6.1 Realization of ASMC-Based MPPT

To investigate the effectiveness in terms of efficiency and dynamic performances, the concept has been analyzed numerically as well as experimentally (see Figure 2.16 and 2.17) using buck-type MIC. The synchronous buck topology enables both high switching frequency (important for low cost, small size) and high efficiency, it does not contribute any voltage gain (which would reduce the number of panels that must be series connected). In most utility-based and residential installations, however, there are a sufficient number of PV panels to provide for the inherent stacking of voltages without requiring the additional step-up from the power converter. When not tasked with providing additional voltage step-up, the power stage can be optimized for cost, size, and efficiency [55].

Nevertheless, the control law  $\text{sign}(\dot{v})\text{sign}(\dot{p})$  of (2.38), which is applicable for

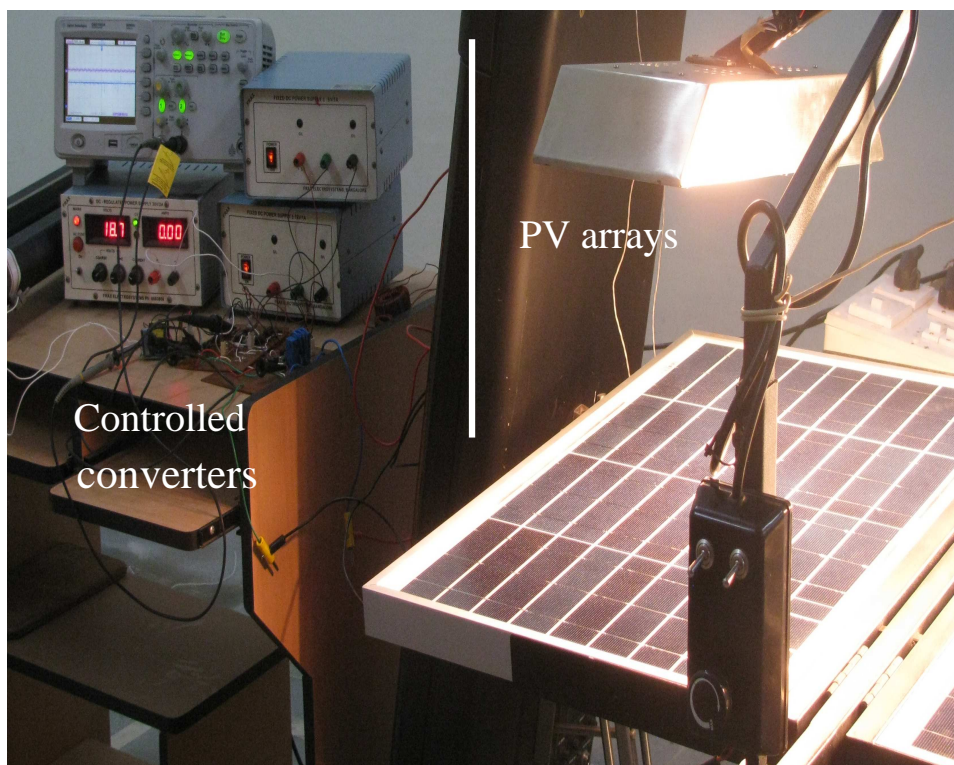


Figure 2.16: Photograph of indoor test set-up of the PV module.

all converter topologies can be implemented by applying only a few commonplace analog components. The signals after sensing are successively fed to an analog multiplier **AD633** which is utilized to assess the array power  $p = vi_{pv}$  and then, to a differentiator which is realized by a first-order high pass filter with an arbitrarily chosen time constant  $T_d \approx 100\mu s$  (since perfect differentiators cannot be realized in practice). Note that, its output yields only an approximation to the true time derivative of both  $p$  and  $v$ . Moreover, instead of using  $\pm 1$  to represent the sign of  $\dot{p}$  or  $\dot{v}$ , it is more convenient in practice to use the boolean 0/1. A comparator **LM311** is used to evaluate the sign of  $\dot{p}$  by producing a binary signal  $w_p$ , whose value is 0 if  $\dot{p} < 0$  or 1 if  $> 0$ . The array voltage  $v$  is also treated likewise and produces a second binary signal  $w_v$ . The multiplication of these signals (using XOR gate **4070BC**) gives another binary signal which would indicate whether  $v$  should be increased or decreased in order to converge upon the MPP. If its output is 0, then  $v$  should be increased, else if 1, then  $v$  should be decreased. This is obtained by feeding the sampled output of XOR-gate to a D-type latch **74LS74** so that the output of the latch circuit provides a signal that makes a decision to close or open the switch only at regular intervals. Moreover, the latch circuit minimizes the effects of unavoidable interference generated by the converter's switching action, and likewise prevents the

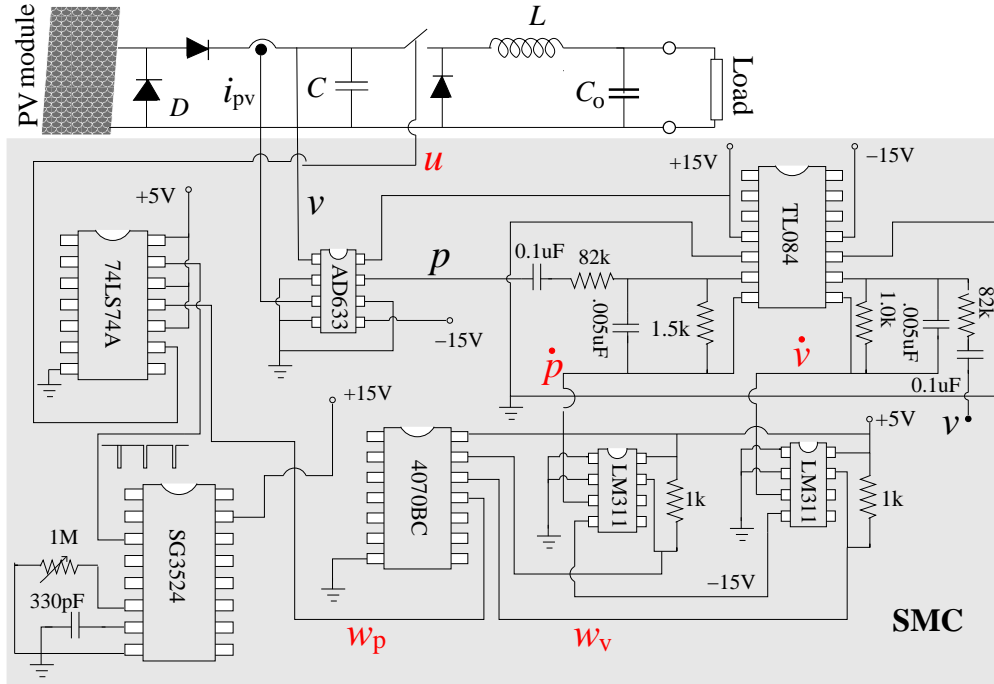


Figure 2.17: Schematic diagram of indoor test set-up.

high frequency chattering within the switching box  $S_B$ . Thus, the controller acts as a  $\Delta$ -neighborhood SMC (see Section 2.4).

## 2.6.2 Performance Analysis

In an ideal SMC, the total time taken to complete both the SM operation phase and the reaching phase is known as settling time  $t_s$  [84]. Depending on the magnitude of load and irradiation fluctuations, the capacity of  $C$ ,  $L$ , and  $C_o$ , the time taken for  $x$  to track from any point on  $H = 0$  to the steady-state equilibrium may vary. Under parameter fluctuation, the resulting  $t_s$  will be small if  $x$  reaches SS within the existence region  $\Pi$ . This can be explained by a representative phase-plane diagram as shown in Figure 2.18(a).

Here, for irradiance  $G = 1000 \text{ W/m}^2$  and an arbitrary initial condition  $x$  eventually hits  $H$ , inside the existence region  $\Pi_{1000}$  in finite time and slides along the surface. Once we change  $G$  from 1000 to 400 and then to  $30 \text{ W/m}^2$  successively, the trajectory suddenly starts from a different initial position (which is the final value of the previous states) and reaches  $H = 0$ , inside the region  $\Pi_{400}$  and  $\Pi_{30}$  respectively. Since it reaches the switching surface within the existence regime, one could expect a less oscillatory dynamic responses during the reaching phase, and that can be evaluated from (2.41),

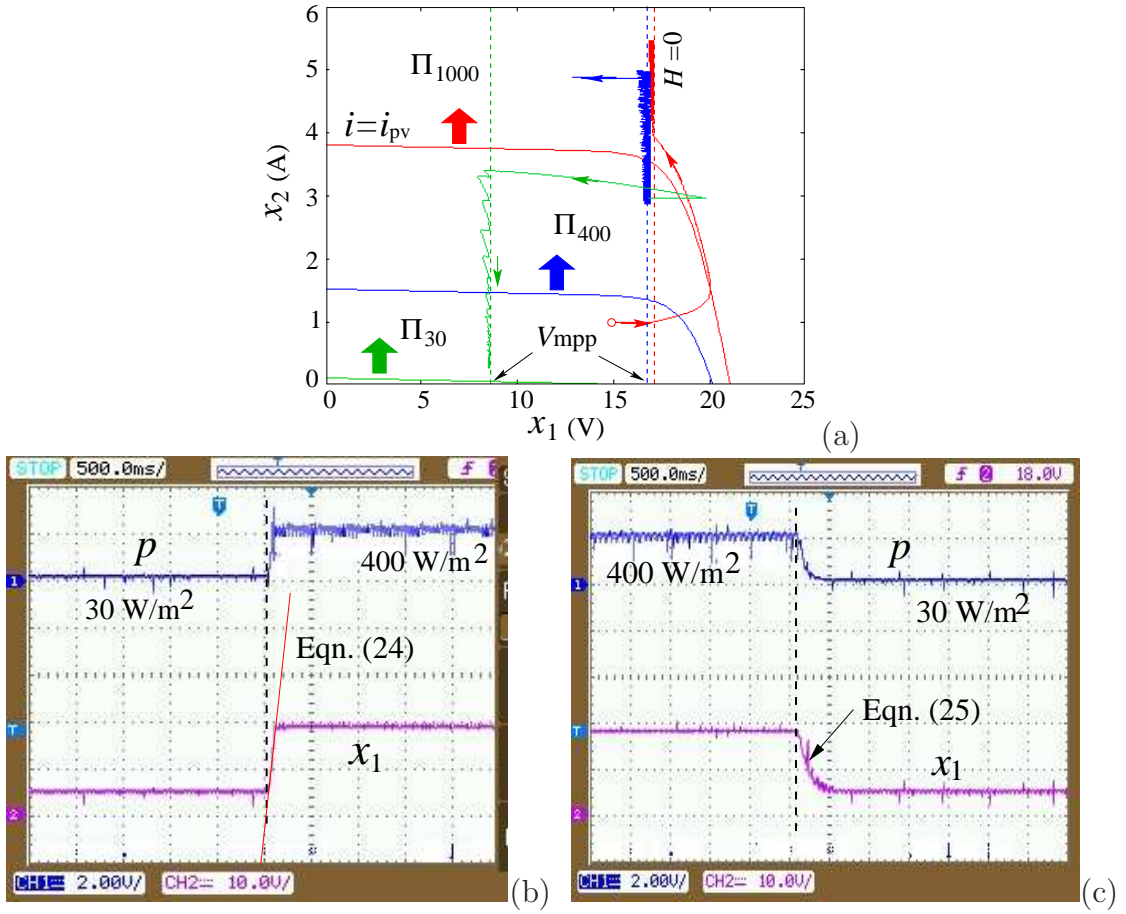


Figure 2.18: (a) The condition for less transient oscillation under sudden irradiation variation from 1000 to 400, and then, from 400 to 30 W/m<sup>2</sup>; and corresponding experimental validation for irradiation fluctuations: (b) from 30 to 400; and (c) from 400 to 30 W/m<sup>2</sup>. CH 1:  $p$  (18 W/div), CH 2:  $v$  (10 V/div). All other parameters are same as in Figure 2.13.

as

$$x_1 = \frac{i_{pv}(G + \Delta G) - i_{pv}(G)}{C}t \quad (2.60)$$

where  $\Delta G$  is the step-up irradiation fluctuation. While for step-down irradiance, trajectory evolution from one attracting region to another is governed by third-order dynamical equation <sup>3</sup>

$$C_o L \frac{d^3 x_1}{dt^3} + \frac{L}{R_{eq}} \frac{d^2 x_1}{dt^2} + \left(1 + \frac{C_o}{C}\right) \frac{dx_1}{dt} + \frac{1}{C R_{eq}} x_1 = \frac{V_{bus}}{R_{eq}} + i_{pv} \quad (2.61)$$

with roots of the characteristic equation  $s_{1,2,3} = -1/R_{eq}C_o, \pm j\sqrt{(1/LC)}$  for  $C_o \gg C$ .

<sup>3</sup>Here load current  $i_o$  is approximated as  $(v_o - V_{bus})/R_{eq}$  [78].

Table 2.4: Major Characteristics of MPPT Techniques

Methods	Tracking Factor	Convergence Time	Steady-State Oscillation	CT and Implementation	Accurate?
P&O [66]	Good	Varies	Varies	Less, Simple	Yes
Adaptive P&O [58]	Very good	Fast	Less	More, Complex	Yes
PI-based P&O	Excellent	Varies	Varies	More, Medium	Yes
InC [89]	Good	Medium	Less	More, Medium	Yes
Load $i_o/v_o$ maximization [90]	Good	Fast	Varies	More, Medium	No
RCC [91]	Good	Varies	Less	Nil, Simple	Yes
Adaptive RCC [75]	Excellent	Fast	Less	More, Complex	Yes
<b>Proposed ASMC</b>	<b>Excellent</b>	<b>Very Fast</b>	<b>Less</b>	<b>Nil, Simple</b>	<b>Yes</b>

Moreover, for  $\frac{1}{2\pi}\sqrt{1/LC} \gg T$ , since the natural frequency of oscillation of MPVS is almost constant as compared to an external clock pulse  $T$ , therefore trajectory will be converged exponentially as  $x_1(t) = x_1(0)e^{-t/ReqC_0}$ . This has also been experimentally confirmed by obtaining the continuous-time waveforms of both  $p$  and  $x_1$  as shown in Figure 2.18(b) and (c). The experimental results are captured by considering a single MPVS with a varying irradiance ranging from 40% to 3% of nominal irradiance  $G = 1000 \text{ W/m}^2$ . The classical P&O algorithm and analog ripple correlation control (RCC) [91] techniques with local resistive load  $2 \Omega$  are considered to compare the tracking performance for equal irradiation fluctuation, because of their simplicity and easy to implement. Figure 2.19 shows that under sudden irradiation fluctuation and CCM operation the ASMC-based MPP tracker not only exhibits a smaller maximum peak over- and under-shoot without losing the steady-state performance or robustness of the system, but also takes less than 2 ms to settle, which is quite faster than that of adaptive P&O algorithm with step-size  $\Delta d$  [58]. In the past, various digital as well as analog MPPT techniques and their comparative studies have been reported [58, 92, 93]. The careful observations (see Table 2.4) on such techniques reveal that the adaptive and PI-based P&O techniques are beneficial for their high-quality tracking factor (TF), smaller ripple voltage in steady-state, good transient performance, and medium complexity of implementation. Nevertheless, since they are implemented in the digital domain (in a microcontroller or FPGA platform), they therefore require more computation time (CT) and results in the closed-loop system to exhibit quantization-induced limit cycle oscillations [65]. Moreover, analog RCC [91] techniques used to delivered maximum available power in the steady-state is also not suitable enough (see Figure 2.19). Since the MPP of PV system will vary as solar insolation varies, it is not guaranteed that RCC can

exhibit critically damping behaviors under rapidly changing environmental conditions. Recently adaptive RCC technique [75] has demonstrated fast convergence and high performance under rapidly changing weather conditions, but the implementation of this technique can still be undesirably complex. While the proposed ASMC-based MPPT technique is very easy to implement in the analog domain, absolutely free from processing delay and quantization effect, and the cross-coupling effects in case of series-connected converters configuration. Also, it can swiftly converges to the desired MPP with fast dynamic response and guaranteed stability without incorporating any extra hardware complexity.

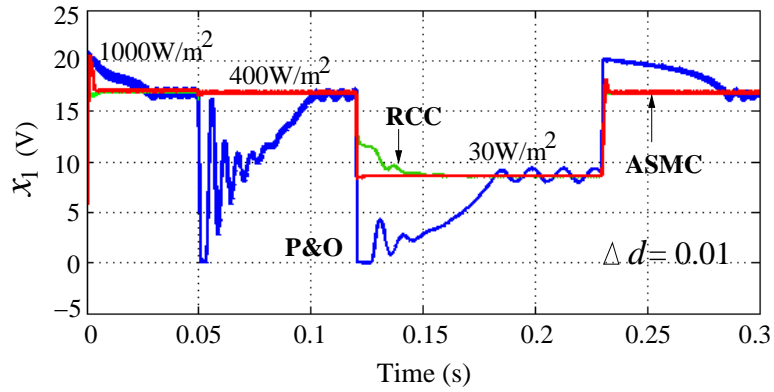


Figure 2.19: Tracking performance under sudden change of  $G$ .

In order to address these, let us look at (2.30) and (2.59). Here, the inequality condition (2.59) necessarily provides the sufficient condition for an asymptotic stability of the single MPVS. For a fixed value of output voltage and maximum input power  $P_{in}|_{mpp} = x_1 \dot{i}_{pv}|_{mpp}$  [see Figure 2.9(b)], the stable steady-state operation of each MPVS is strongly limited by its minimum loading condition  $I_o \leq I_{mpp}$ . One cannot operate it satisfactorily over a wide load range. Therefore, in order to balance the input power with its load power, MPVS may operate at some equilibriums which are not the desired MPP [87] (see curve **D** of Fig. 2.13). However, this can be easily reduced by a series-connected MPVSs architecture [55, 56]. In fact, minimum load current shared by each converter in series configuration will be reduced further than that of single MPVS since  $V_{bus} = \sum_1^k V_{rmo}^k > V_o^k$  (see Section 2.4). Thus, it essentially interprets as an expanded load range, requirement for the each system's state trajectory or input capacitor voltage to be directed towards respective sliding surface  $H^k = (x_1^k - V_{mpp}^k)$  and satisfies the existence condition (2.59). Once they satisfy, one can expect a stable steady-state operation with fast dynamic response. Moreover, the input voltages of individual modules  $v^k$  converge to  $V_{mpp}^k$  and remain unaltered over a wide range load variation. Because of this operation proposed MPP tracker forces the MPVS to

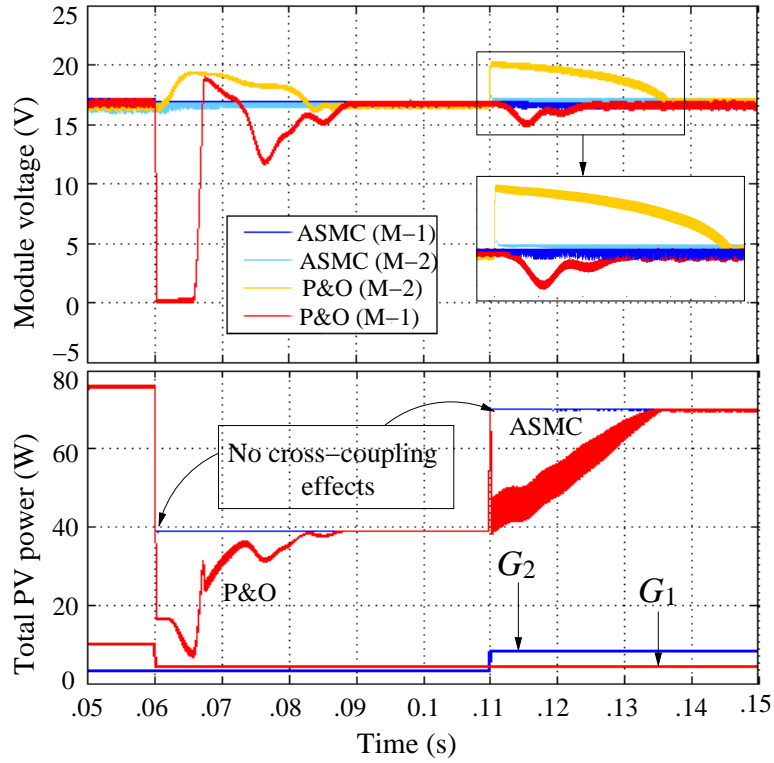


Figure 2.20: The dynamic response showing the comparison of coupling effects between Figure 2.9 and P&O based control algorithm for  $i_o = 4.8$  A. Here  $G_1$  and  $G_2$  represent the solar insulations for first and second module, denoted by M-1 and M-2 respectively.

operate as a voltage source having a small output impedance, and thus gives an insight clue about the cause of reduced cross-coupling effects. The cross-coupling effects are an undesired property of cascaded converter systems, causing reduction in the system power output and dynamic performances [77, 79]. In [77], the authors showed that the reduction of tracking performance due to cross-coupling effects can be significantly improved if the individual converters are closely operated as an ideal voltage source. The mathematical proof of such concept has also been reported therein. With this view, we simulate the series-connected MPVSs and observe the cross-couplings effects by introducing an irradiance sequence ( $G_1$  from 1000 to 500 and  $G_2$  from 400 to 800  $\text{W}/\text{m}^2$ ) into PV modules attached to each converter, while keeping the other parameters' value fixed. Figure 2.20 shows that due to slow tracking response of classical P&O algorithm, the dynamic performance of MPPT system under sudden irradiance fluctuation in one module is greatly affected by other one. While in the case of ASMC technique there are no visible cross-coupling effects. The resulting response



in the input voltages of the converters is not affected by the disturbance caused by any changes in other PV module's irradiance. Thus, it improves the energy yield of the system.

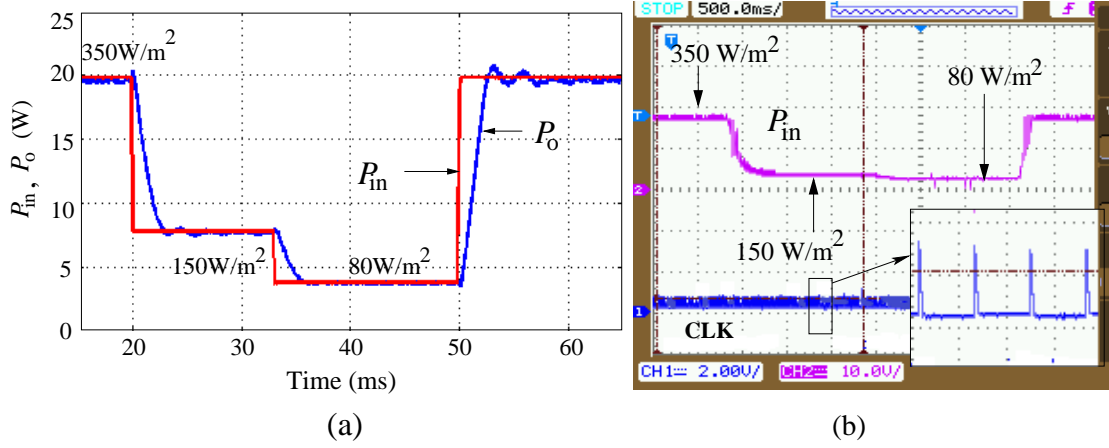


Figure 2.21: (a) Representative diagram showing the transient performances of  $P_{in}$  and  $P_o^d$  (without any cross-coupling effects) for  $i_o = 4.8$  A and  $R_{eq} = 0.02$   $\Omega$ ; and (b) its experimental confirmation. CH 1 is the clock pulse and CH 2 is the input power  $P_{in} \approx 9$  W/div.

Table 2.5:  $\eta$  (%) of series configuration for different  $G_1$  (W/m<sup>2</sup>) when  $i_o = 4.8$  A and  $R_{eq} = 0.02$   $\Omega$

$G_1$	1000	850	700	550	400	250	50
$\eta$	97.52	97.28	96.68	96.66	96.60	96.11	92.76

Moreover, since the efficiency of the overall system is determined by stable steady-state behavior and transient response of MPPT efficiency [70], therefore, the highest possible efficiency can only be achieved if the existence condition (2.59) is satisfied. With this view, system dynamics are analyzed and also validated experimentally over a wide range of rapidly fluctuating irradiances. The test has been performed in indoor by considering a string of two series-connected MPVSSs, and each of them is artificially illuminated by different levels irradiances  $G_1 = 350$  and  $G_2 = 40$  W/m<sup>2</sup> (measured by Pyrometer). We then successively change the insolation level  $G_1$  from 350-to-150-to-80, and back to 350 W/m<sup>2</sup> without varying  $G_2$ . Figure 2.21(a)

and (b) reveal that proposed ASMC-based series architecture not only tracks the true MPP of each module efficiently, but is also able to locate and extract the maximum available power from the PV array under any mismatching conditions (see Table 2.5). One cannot achieve it, simply by iteratively changing the duty ratio of individual dc-dc converter under such rapidly changing inhomogeneous solar irradiances.

## 2.7 Conclusion

In this chapter, an analog circuitry based fast and robust MPP tracker is proposed for buck, boost, and buck-boost-type modular PV systems. Based on the condition of SM in HDSs, the exact mathematical models for all such converter systems were derived. Discussion on the modeling and analysis were done to design and extract the best optimized performances (in terms of steady-state and transient responses with improved overall systems' efficiency) using the concepts of equivalent control law and fast-scale stability analysis. These are experimentally verified by taking an example of buck-type MIC and compared with P&O based algorithm. The results demonstrate that under sudden irradiation fluctuations, the tracking performances of analog MPP tracker employing SMC is not only faster than the reference one, but also exhibits less steady-state oscillations with reduced cross-coupling effects. One drawback of this method is that if the converter's switching frequency varies, it is required to redesign the high pass filter circuit which is used to obtain the time derivatives of module current and voltage. Moreover, hardware realization of boost-type tracker and also its use in cascaded converters architecture is a subject of the future investigation.

# Chapter 3

## DC-AC Power Processing

In dual-stage GPV systems, after boosting the voltage from low PV module voltage to a high dc bus voltage, the dc-ac inverter stage is employed to convert dc power into ac power and feed the power into the utility grid. In low or medium-scale applications, the galvanic isolation is not required, if the ground leakage current is under a certain limit. There are a lot of inverter topologies are reported based on output power, the total current harmonics and the cost. The different topologies of the inverter with their proper switching technique will be discussed in this chapter. The stand-alone mode of operation with a fixed dc supply will be considered here. Since, maintaining good voltage regulation and achieving fast dynamic response under sudden load fluctuation are extremely important for a dc-ac inverter system; two current control schemes will therefore be discussed to address the above power quality issues.

### 3.1 1- $\phi$ Inverter Topologies

Single-phase inverters are mostly used in the domestic sector. The majority of such inverter systems can have up to 5kW and are roof mounted. Based on the input supply, the 1- $\phi$  dc-ac inverter topologies can be divided into two groups: voltage source inverter (VSI), and current source inverter (CSI), which are shown separately in Figure 3.1 [94], [95]. VSI are commonly used for low or medium power level of dc-ac power conversion, whereas CSI is used for the high power applications. A large inductor is connecting in series with the dc bus voltage which makes CSI bulky and expensive. As a series diode is connected with the main switches in CSI topologies to block the reverse voltage which may also increase the conduction losses. Due to these drawbacks, CSI has limited applications. On the other hand, VSI is the dominant

topology in PV system due to the following advantages:

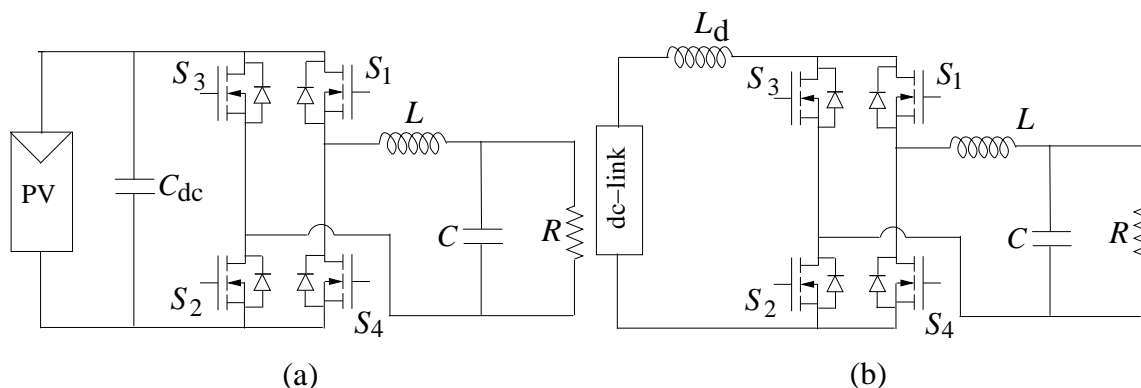


Figure 3.1: Schematic diagram of inverter topologies: (a) VSI; (b) CSI.

- VSI uses self-commutating switching circuit.
- As a capacitor is connected in between PV output and inverter, so it handles the output current regulation and dc bus voltage regulation.
- The output voltage waveform is mostly remaining unchanged by the load.
- Broad power level applications.
- Efficiency can be improved by using proper switching techniques.

Based on the commutation process, most of the inverter topologies are either line frequency-commutated inverters or self-commutated inverters [94], [95]. Generally, line frequency-commutated inverter uses a sinusoidal signal to generate the ac output. These are commonly used due to the efficient power conversion and low cost. But the drawbacks with this configuration are the poor power quality of the output voltage and have a power factor between 0.6 and 0.7 [95]. On the other hand, self-commutated inverters are commonly used because it can operate at high switching frequency, which produces a low THD output voltage. Moreover they are robust and cheap.

Single-phase half bridge and full bridge inverter topologies are commonly used in PV system as the dc-ac power processing stage. In half bridge inverter topology, two equal capacitors are connected back-to-back across the dc input, so that a voltage of  $E$  (supply voltage) appear across each capacitor. Both the switches are operated in the complementary mode so that the output voltage varies from  $-E$  to  $+E$ . The  $LC$  low pass filter is used at the output of the inverter to minimize the high switching harmonics. On the other hand, a full bridge inverter is also known as H-bridge inverter

consists of two half bridge inverters. The output voltage of this inverter is twice that of the half-bridge inverter, which implies that for the same power, the current rating in the former case is half of the later. These topologies are used in high power applications. So, a 1- $\Phi$  full bridge VSI is considered throughout the thesis for the dc-ac power conversion. This topology can also be used in UPS applications.

## 3.2 Modulation Techniques for VSI

Pulse width modulation (PWM) techniques of VSI have been the subject of intensive research over the last several years as the primary strategy to control the ac output voltage or current of a dc-ac converter [96]. The concept of PWM is to control the duty cycle of each switch at a high switching frequency to generate a train of controlled pulses that have the required low-frequency fundamental component. The second objective of these PWM schemes is to arrange the switching pulses in such a way that it can minimize the unwanted harmonic components and the switching losses. The classical and most widely used modulation technique for a VSI is naturally sampled sine pulse width modulation (SPWM) [96]. Here, a low-frequency voltage control signal (sine wave) is compared with a high-frequency carrier, i.e., triangular signal and the comparison result, which is a logic output, is used to determine the on or off-state of the power switches. The frequency of the triangular signal determines the inverter switching frequency. Out of four switches of the inverter,  $S_1, S_2$ , and  $S_3, S_4$  are operated in a complementary manner, and to avoid the short circuit between these switches, a dead time has to be introduced. Naturally sampled SPWM does not control the position of the pulses it generates in each cycle and the minimum pulse width is not controlled. But uniformly sampled SPWM technique also requires a triangle carrier signal at switching frequency but it only uses the comparison result to determine the on or off duration of the switches but not the pulse position. The pulse position is uniformly controlled, e.g., put at the center of every switching cycle.

Another common form of PWM technique for VSI is space-vector modulation [97]. The primary advantage of this modulation technique over classical sinusoidal PWM is the explicit identification of the pulse placement within each carrier period as an extra degree of freedom, that has been shown to improve the harmonic performance of the inverter. However, implementation of this scheme is quite complex and commonly used in the poly-phase system.

Consequently, other methods like multi-carrier PWM and selective harmonic elimination PWM are used for harmonic elimination in VSI [96]. These techniques

are widely used because it can be easily implemented for low voltage applications [98]. Normally harmonic elimination methods can be classified as level-shifted PWM and phase-shifted PWM methods [99]. The level Shifted-PWM is characterized into phase disposition, phase opposition disposition and alternative phase opposition disposition [100]. Compared to the all above techniques, alternative phase opposition disposition method is the most major process to express harmonics are centered as sidebands around the carrier frequency [101]. Merits of this approach in multi-carrier PWM have no harmonics occur at the carrier frequency and higher band width [102]. Among all the above methods, selective harmonic elimination PWM is the only method for selecting proper switching angles to eliminate low-order harmonics and minimize the THD of the output voltage. The main objective of this method is to determine the switching angles to specific lower order harmonics suppressed in the output voltage of the inverter to achieve desired fundamental component with possible minimum THD [103]. This method operates a set of non-linear transcendental equations as the fitness or objective function that includes many local optimal solutions [104]. But all the above modulation techniques are applicable to voltage mode control of the inverters.

On the other hand, the hysteresis-band current controlled modulation technique is the most popular because of its simplicity in implementation, inherently limiting the over-current and very fast response. Hysteresis-band PWM techniques generate the switching pulse for the inverter switches based on a nonlinear feedback loop with two-level hysteresis comparators. The current error is allowed to pass through a band so that the switching states are defined by the upper and lower envelope of the band. The switching frequency of the inverter is decided by the width of the band. The only disadvantage of this PWM technique; the operating switching frequency depends largely on the load parameters and varies with the ac voltage. However, several methods are proposed for the constant switching operation, which will be discussed later. Hence, this modulation technique is used throughout this thesis to generate the controlled switching pulse for the inverter.

Based on the level of the output voltage of the inverter, the PWM techniques are further classified into two categories, which are discussed below.

### 3.2.1 1- $\phi$ Bridge Topology with Bipolar PWM

The bipolar switching scheme by using the hysteresis band is shown in Figure 3.2(a). In bipolar switching scheme, the error current is passed through a single hysteresis band to control the turn on and turn off period of the switching pairs;  $S_1$ ,  $S_2$ , and

$S_3, S_4$  of the inverter (see the Figure 3.1(a)). In this case, the inverter will produce a positive output voltage when the current error touches the lower hysteresis limit. On the other hand, a negative output voltage is produced when the current error touches the upper hysteresis limit. When the switches  $S_1$  and  $S_2$  receive on signals, a positive output voltage  $E$  is produced. This on period lasts until the output current error reaches the upper hysteresis limit. Thus, during the on period, the current error is changing from  $-h$  to  $+h$ . During the off period, when switches  $S_1$  and  $S_2$  receive off signals (switches  $S_3$  and  $S_4$  receive on signals), the output voltage is negative, i.e.,  $-E$ . During this period, the current ripple changes from  $+h$  to  $-h$ . The switching frequency of the inverter is decided by the width of the hysteresis band, i.e., the value of  $2h$ .

In practice when a switch pair is switched off ( $S_1$  and  $S_2$ ), the next pair ( $S_3$  and  $S_4$ ) is not switched on straight away. This has to ensure that the switches being turned off are fully off before the next pair is turned on. The short time that is allowed to elapse between initiation of turn-off of one pair and initiation of turn-on of the next pair is called the blanking or dead time. The blanking time used is of the order of one or two microseconds. Without a blanking time there may be a risk of short-circuiting the inverter dc supply.

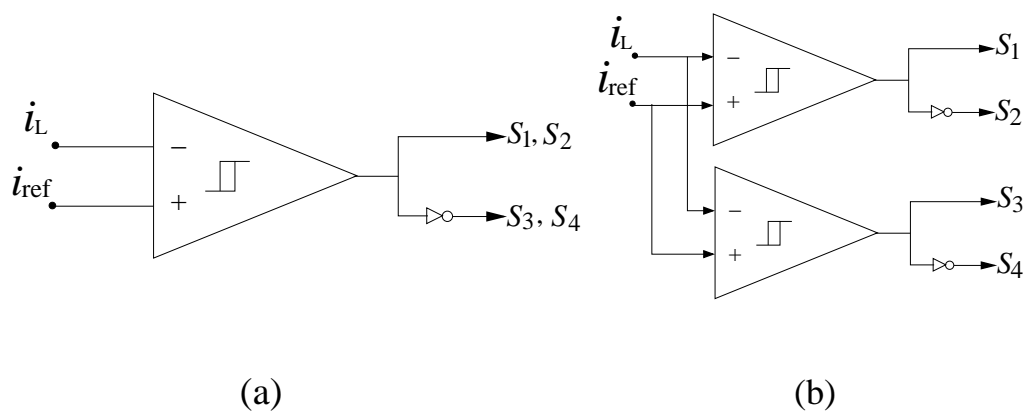


Figure 3.2: PWM techniques for VSI: (a) bipolar; (b) unipolar.

### 3.2.2 1- $\phi$ Bridge Topology with Unipolar PWM

The unipolar switching scheme for an inverter can be achieved by using two hysteresis band as shown in Figure 3.2(b). In this switching scheme, the four switches shown in Figure 3.1(a) are turned on and off to generate three voltage levels,  $E$ , 0, and  $-E$ , respectively. Here one pair of switches (say,  $S_1$  and  $S_2$ ) is controlled by the smaller

hysteresis band and another pair of switches ( $S_3$  and  $S_4$ ) is controlled by the larger hysteresis band. The current error is mainly decided by the smaller hysteresis band. When the smaller hysteresis band has lost its ability to control the current error, then only the larger hysteresis band is active. The smaller hysteresis band cannot control the current error when the output voltage polarity is reversed. In this condition, the polarity of the output voltage can be reversed by the larger hysteresis band. Thus, the pair of switching devices that is controlled by the larger hysteresis band is switched at the fundamental output frequency. During the positive half-cycle of the output voltage, switch  $S_2$  (switch  $S_3$ ) receives an on signal (off signal). On the other hand, during the negative half-cycle of the output voltage, switch  $S_2$  (switch  $S_3$ ) receives an off signal (on signal). The output current error is controlled by switches  $S_1$  and  $S_4$ . The output voltage has a unipolar characteristic similar to the symmetrical unipolar carrier-based PWM.

As implementation of unipolar PWM scheme is quite complex, so bipolar PWM technique is commonly used for switching the inverter.

### 3.2.3 LC Filter Design for 1- $\phi$ VSI

The first design consideration is the selection of components which can be determined by setting criteria on ripple current and filtering criteria. First of all, the inductor  $L$  can be selected by the ripple current in the inductor. A larger inductance value allows a smaller inductor switching ripple; however, a large inductance value will increase the cost, volume, and weight of the inductor. Thus, the choice of the inductor value is a trade-off between ripple current specification and cost. Second, the filter capacitor  $C$  is calculated by the cut-off frequency of the  $LC$  second-order filter for the output voltage  $v_0$  under standalone mode. The cut-off frequency of the  $LC$  filter is suggested to be between 10 times lesser than switching frequency and 10 times higher than the fundamental frequency.

## 3.3 Classical Control Methods for 1- $\phi$ VSI

The PWM VSI is extensively used in ac power conditioning systems. A 1- $\phi$  VSI supplies the non-linear and critical step changing loads. The above loads deform the desired sinusoidal output voltage of inverter [105]. For all types of loads the THD of the inverter output voltage should be as per the IEEE standard 1547, i.e., less than 5%. Moreover, current-controlled inverter should be met the following substantial



performances; fast transient response, low current ripple in the steady-state, optimal switching pattern and stability for the load variation. In recent past, several control strategies have been suggested for the inverter operations depending on how the current or voltage error signal is processed. A review of different current control techniques used for VSI are discussed here.

### I. Conventional PI controls

The control technique based on proportional-integral (PI) controller in the stationary reference frame where the PI regulators have to track sinusoidally varying inputs [106]. Since PI controller only guarantees zero steady state error under dc reference input, this control technique cannot be performed well. Another control technique based on proportional control plus model-based compensation was proposed [107]. It does not require the information that the reference input is a 50 Hz sine wave so that the control design has to be able to handle arbitrary input, which is unlikely to achieve a good control performance for inverter applications. An inverter control technique based on PI regulation only was developed [108]. Even though the system is required to handle harmonic current, no theoretical measure has been taken to address the issue. A dual loop proportional control scheme have designed for 1- $\phi$  half-bridge inverters in island mode [109]. The authors have analyzed through the small signal frequency domain analysis to stabilize the closed-loop system. However, the simple proportional controller can not provide satisfactory performances in either steady state or transient.

### II. Proportional-resonant control

A proportional-resonant (PR) controller is commonly used in a stationary reference frame control like  $abc$  or  $\alpha\beta$  frame. These controllers have achieved a high gain around resonant frequency and thus is capable of eliminating a steady state error, when control variables are sinusoidal [110], [111], [112]. In this controller, a low order harmonics compensator can be easily implemented to improve the performance of the current controller without influencing its behavior [110]. In order to maintain good performance of the controller, the resonant frequency must be identical to the frequency of the output voltage. The frequency can be adaptively adjusted according to output voltage frequency variation as reported in [112].

### III. Deadbeat control

Deadbeat (DB) predictive controllers are widely used for sinusoidal current regulation of different applications due to its good dynamic performance [113], [114], [115]. Theoretically, this controller has a very high bandwidth and hence, tracking of sinusoidal signals is very good. The principle of the DB controller is to calculate the derivative of the controlled variable in order to predict the effect of the control action. Deadbeat predictive control is widely used for current error compensation and offers high performance for current-controlled VSIs. However, it is quite complicated and sensitive to system parameters [113], [114].

### IV. Multiloop control

A multi-loop feedback controller is suitable to meet the above requirements. Generally, this controller is used to control the output voltage or current of a VSI when it equipped with a high order *LC* or *LCL* passive filter. It involves the use of an outer and an inner current loop. The outer loop ensuring the steady state performance and the inner loop providing the transient performance and improving the stability [116]. The stand-alone or grid-connected PV systems have to be controlled in such a way that the output voltage or current should be in phase with an external sinusoidal reference proportional to the utility grid. Hence, this external sinusoidal reference is included in the control loop. In these cases, the control loop design is based on the minimization of the error defined as the difference between the reference signal and the output signal. This control method is known as a “tracking” control scheme, in the sense that the output signal is constrained to track the reference by means of the control action. In stand-alone systems, a multi-loop voltage controller with a capacitor current feedback as inner loop can eliminate the output LC filter resonant peak to increase stability in load disturbance and enhance dynamic performance [117].

### V. Intelligent control

Besides above conventional control, intelligent control can also be applied to inverter control. A fuzzy logic controller has developed for voltage loop regulation which yields a satisfactory performance [118]. However, the control rules are based on empirical knowledge which cannot be obtained directly.

### VI. Sliding mode control

A non-linear control scheme, namely, sliding mode control (SMC) strategy

has been proposed in inverter control since these are well known for their robustness, guaranteed stability and good dynamic response under the wide range of operating conditions. The SMC utilizes a switching control law to drive the state trajectory from any initial positions to a specified surface in the state space called sliding or switching surface and maintain it on this surface for all subsequent time [119]. However, SMC operates at variable switching frequency at which an undesirable chattering phenomenon may occur. In order to compensate the above drawback partially, the SMC are realized by means of a hysteresis comparator [120], which also provides a variable switching frequency. Several authors have proposed constant frequency SMC by means of a variable width hysteresis controller [121], which can however lead to a complex analog implementation, thereby involve more cost. Moreover, the width of hysteresis band depends on the converter parameters. Alternatively, fixed frequency SMC can also be achieved by comparing an external ramp signal to the switching surface [122]. Hence in these controllers, the switching instant does not depend on the switching surface behavior.

Over the past decades, many efforts have been devoted to this research area and references therein [115, 120]. A discrete-time sliding mode control technique has developed for 1- $\phi$  inverters in both voltage and current loops [123]. In this technique, the control variable in each sampling period is calculated based on the plant model and feedback quantities. The control is continuous and the chattering problem does not exist. The presented results show good performances under both linear and nonlinear loads. However implementation of this controller is quite complex, and involve more cost. Another SMC control technique using deadbeat current control and proportional voltage control was proposed [115]. The deadbeat control concept is suitable when the plant model parameters are known. The presented result is reasonably good. However, its dependence on knowledge of plant parameters limits its application as an outer loop controller in multi-loop feedback systems.

Based on the above discussion, SMC is suitable for improving both steady-state and dynamic performance of an inverter system. More details, including SMC design, is discussed in this chapter. Two SMC controllers are proposed to address these issues. First, a fixed frequency hysteretic current (FFHC) controller is proposed on the basis of SMC. The Proposed controller is compared with the carrier based PWM voltage controller under the same load fluctuation to evaluate its performance. Then, another sensorless SMC scheme is also designed for the same inverter by taking an ellipsoidal

switching surface in phase plane, rather than the time plot.

### 3.4 SMC-Based 1- $\phi$ VSI and Its Limitations

Normally, SMC is considered as a good alternative to the control of switching converters. The main advantages of such control scheme over classical one are its robustness and high dynamics performances under parameter fluctuations. However, in order to achieve these advantages the power electronics practitioners usually design and implement the SMC on the basis of hysteresis controller with a band  $\Delta$  [124]. The hysteresis band  $\Delta$  essentially forms the boundary layers of the switching surface. Within these boundaries the trajectory (i.e., current and voltage) of the systems jitters and travel along the switching surface guided by boundary layers. Ideally such switching or sliding surface is designed for the 1- $\phi$  VSI system so that it can act as a reference path for the trajectory of the controlled system, and that can be expressed as a linear combination of state variables  $x_1$  and  $x_2$ , given by

$$S = \alpha_1 x_1 + \alpha_2 x_2 \quad (3.1)$$

where  $\alpha_1$  and  $\alpha_2$  are positive real constants, called sliding coefficients and values are calculated as per [124]. However, it is important to note that for an ideal SMC, it requires an infinite switching frequency so that the state trajectories in the neighborhood of the switching surface can move precisely along the surface. But the operation of such infinite switchings in power electronics inverter system is practically impossible. It is, therefore, necessary a typical control circuit that would require a relay or hysteresis function to restrict the infinite switching frequency as shown in Figure 3.3(a). Where the control signal is defined as

$$u = \begin{cases} 1 & \text{when } S > +\Delta \text{ and } \dot{S} < 0 \\ 0 & \text{when } S < -\Delta \text{ and } \dot{S} > 0 \end{cases} \quad (3.2)$$

Note that, for the hysteresis function (3.2), one can get the infinite switching frequency. The switchings will occur with the band  $S = \pm\Delta$  with a frequency depend upon the slope of the inductor current  $i_L$ . This hysteresis function therefore causes a trajectory oscillations within the vicinity of  $2\Delta$  around the surface as shown in Figure 3.3(b). The  $S$  must increase from  $-\Delta$  to  $+\Delta$  ( $\dot{S} > 0$ ) during  $\Delta t_1$ , while in  $\Delta t_2$ , it decreases from  $+\Delta$  to  $-\Delta$  ( $\dot{S} < 0$ ). The switching frequency is then given by

$$f_s = \frac{1}{\Delta t_1 + \Delta t_2} \quad (3.3)$$

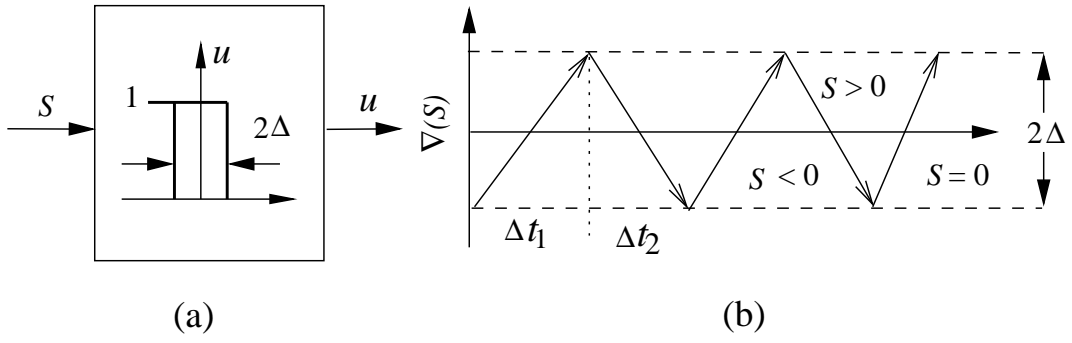


Figure 3.3: Schematic diagram showing: (a) hysteresis function; (b) the state trajectory in the vicinity of sliding surface  $S = 0$ .

where  $\Delta t_1$  is the conduction time of the switches  $S_1, S_2$  and  $\Delta t_2$  is the conduction time of  $S_3, S_4$  respectively. Now, assuming the state trajectories are constant near the surface  $S = 0$ , and by calculating the values of  $\Delta t_1$  and  $\Delta t_2$ , we can easily evaluate the switching frequency [124], given by

$$f_s = \frac{\alpha_2}{4\Delta EL} (E^2 - v_{\text{ref}}^2). \quad (3.4)$$

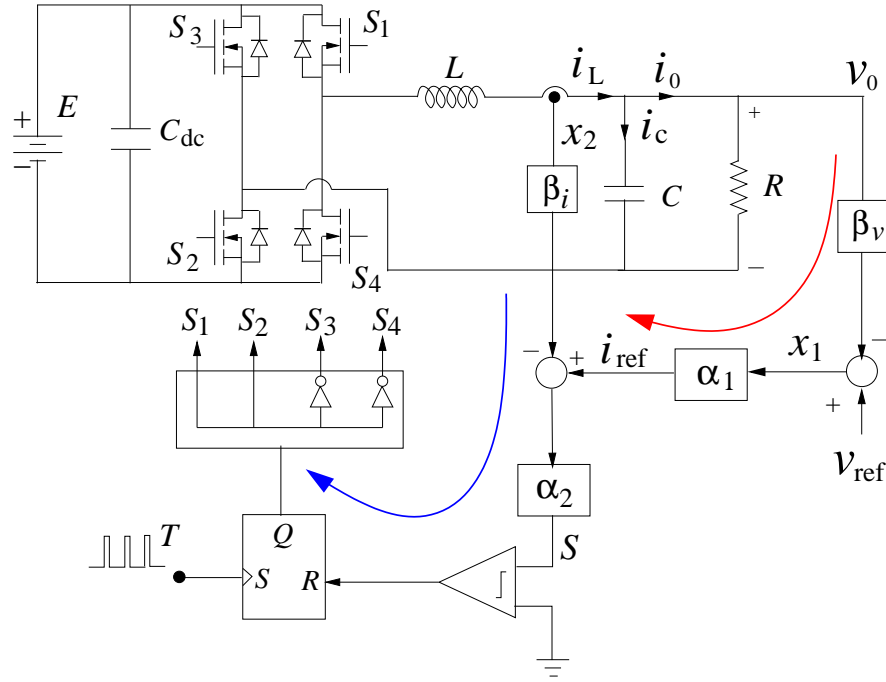
where  $v_{\text{ref}}$  is the external reference voltage set by the user. While, substituting  $v_{\text{ref}} = 0$ , we get the maximum switching frequency

$$f_{s,\text{max}} = \frac{\alpha_2}{4\Delta L} E. \quad (3.5)$$

Moreover, it is important to note that since (3.3) is heavily depended upon the  $\Delta t_1$  and  $\Delta t_2$ , one can get the constant switching frequency operation. Once output load varies, the  $\Delta t_1$  and  $\Delta t_2$ , thereby the switching frequency  $f_s$  will also vary.

### 3.5 Constant-Frequency SMC-Based 1- $\phi$ VSI

To fix-up such varying switching frequency, a FFHC controller is proposed. The schematic diagram of proposed FFHC-controlled VSI is shown in Figure 3.4. VSI consists of a dc supply voltage  $E$ , a dc link capacitor  $C_{\text{dc}}$ , filter elements  $L$  and  $C$ , a load resistance  $R$ , and four controllable power switches  $S_1$  to  $S_4$ . The switches are controlled by the FFHC control logic, which is implemented by means of a nested feedback controller. The slow outer voltage controller is used to generate the reference current  $i_{\text{ref}}$ , whereas the fast inner current controller is used to generate the switching signal to operate the power switches.

Figure 3.4: The proposed FFHC-controlled 1- $\phi$  inverter.

### 3.5.1 Constant Frequency Operation

As shown in Figure 3.4, the outer voltage controller is used to generate the stationary boundary layer of the hysteresis loop. This is achieved by a linear combination of capacitor voltage  $v_o$  and reference voltage  $v_{\text{ref}}$ , in the form of

$$i_{\text{ref}} = \alpha_1(v_{\text{ref}} - \beta_v v_o) \quad (3.6)$$

The inner current loop controller is used to generate the control signal in binary form,  $u \in \{0, 1\}$ , by comparing the inductor current  $i_L$  with the reference current  $i_{\text{ref}}$  and an externally generated clock pulse of period  $T$ . The fixed frequency switching scheme of the 1- $\phi$  VSI can be clearly explained from the Figure 3.5. At the start of the clock pulse, the switches  $S_1, S_2$  are turned on and the switches  $S_3, S_4$  are turned off, the inductor current  $i_L$  raises. But when  $i_L$  reaches a peak value of the reference current  $i_{\text{ref}}$ , then turn off process will start, so the switches  $S_1, S_2$  are off. The inductor current starts falling until the arrival of next clock pulse. So, the turn on and turn off processes of each switch are completed within one clock cycle, which conforms the fixed frequency switching operation of the inverter. Hence, this is the type of hysteresis current control, where the reference current  $i_{\text{ref}}$  acts as the upper band and the lower band is the points of applying external clock pulse.

The additional advantage of this proposed control scheme is that it inherently acts

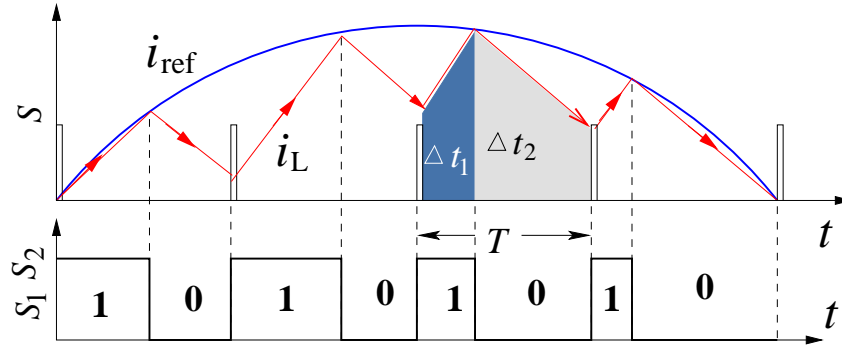


Figure 3.5: Generation of binary switching pulses  $S_1$ ,  $S_2$  over one half cycle, and the switching sequences of  $S_3$ ,  $S_4$  are complementary of power switches  $S_1$ ,  $S_2$  respectively.

as a current limiter for the inverter circuit. As  $x_2 = (i_{\text{ref}} - \beta_i i_L)$ , the inductor current  $i_L$  can never cross the reference current  $i_{\text{ref}}$  as shown in Figure 3.6.1. So, it is possible to limit the load current by limiting the reference current. It therefore leads to the overload and short circuit protection of the inverter.

### 3.5.2 Dynamics of 1- $\phi$ VSI and Its Mathematical Model

Assuming all components are ideal, the state space equations of VSI can be written in matrix form, as

$$\begin{pmatrix} \frac{di_L}{dt} \\ \frac{dv_o}{dt} \end{pmatrix} = \begin{pmatrix} 0 & -\frac{1}{L} \\ \frac{1}{C} & -\frac{1}{RC} \end{pmatrix} \begin{pmatrix} i_L \\ v_o \end{pmatrix} + \begin{pmatrix} \frac{E}{L} \\ 0 \end{pmatrix} u. \quad (3.7)$$

where  $i_L$ ,  $i_C$ , and  $v_0$  are the inductor current, capacitor current and output voltage, and  $u \in (1, -1)$  is the discontinuous control signal. Moreover, in accordance with the sliding mode theory, and to design the switching surface, we redefine the state variables  $x_1$  and  $x_2$ , as

$$x_1 = (v_{\text{ref}} - \beta_v v_o), \quad \text{and} \quad x_2 = i_L \quad (3.8)$$

where  $v_{\text{ref}} = A \sin(2\pi ft)$  is an external reference signal, and  $\beta_v$  and  $\beta_i$  are the corresponding scaling factors of output voltage and inductor current, respectively.

The behavior of the system can be described by the following state space form

$$\begin{bmatrix} \dot{x}_1 \\ \dot{x}_2 \end{bmatrix} = \begin{bmatrix} \frac{1}{RC} & -\frac{\beta_v}{C} \\ -\frac{1}{\beta_v L} & 0 \end{bmatrix} \begin{bmatrix} x_1 \\ x_2 \end{bmatrix} + \begin{bmatrix} 0 \\ \frac{E}{L} \end{bmatrix} u + \begin{bmatrix} d_1 \\ d_2 \end{bmatrix} \quad (3.9)$$

where  $d_1$  and  $d_2$  are the disturbance terms defined as

$$d_1 = \frac{dv_{\text{ref}}}{dt} + \frac{1}{\beta_v} \frac{v_{\text{ref}}}{R} \text{ and } d_2 = \frac{v_{\text{ref}}}{L}$$

In compact form

$$\dot{x} = Ax + Bu + D \quad (3.10)$$

The main objective of sliding mode control is to operate the switches as a function of the state variables to direct the system trajectory to converge at the desired equilibrium point by designing a suitable sliding surface in the state space. In this work, multi-loop with position controller is used for investigation. For the system slides on the sliding surface, the switching control law is given by

$$u = \begin{cases} 1 & \text{for } S > 0 \\ -1 & \text{for } S < 0 \end{cases} \quad (3.11)$$

where the sliding function is given by

$$S(x, t) = \alpha_i(\alpha_v(v_{\text{ref}} - \beta_v v) - \beta_i i_L) \quad (3.12)$$

$$S(x, t) = \alpha_i \alpha_v x_1 - \alpha_i \beta_i x_2 = J^T x \quad (3.13)$$

with sliding coefficients  $J^T = [\alpha_i \alpha_v - \alpha_i \beta_i]$ . A sliding surface is obtained by satisfying the condition  $S = 0$ .

The existence condition for sliding mode operation can be found by using Lyapunov's direct method to solve  $S\dot{S} < 0$ , which gives the existence region of sliding mode. By substituting (3.10), (3.11) and (3.13) to  $S\dot{S} < 0$ , the existence condition is given by

$$\begin{cases} \dot{S}_{S \rightarrow 0^+} = J^T Ax + J^T B + J^T D < 0 \\ \dot{S}_{S \rightarrow 0^-} = J^T Ax - J^T B + J^T D > 0 \end{cases} \quad (3.14)$$

The above inequalities give the existence condition of the SMC as well as the design range for the sliding coefficients, which should ensure the system to remain in sliding mode operation when the system trajectory is close to the sliding surface.

In SMC operation, the dynamics of the system can be characterized using the invariance conditions  $S = 0$  and  $\dot{S} = 0$ . With the condition  $S = 0$ , the system can be represented as

$$S(x, t) = \alpha_i \alpha_v x_1 - \alpha_i \beta_i x_2 = 0 \quad (3.15)$$



By using the condition  $\dot{S} = 0$ , that is,  $J^T Ax + J^T B u_{eq} + J^T D = 0$ , the equivalent control signal, which is the averaged value of the control signal of the closed-loop SMC system, can be obtained as

$$u_{eq} = -[J^T B]^{-1} J^T (Ax + D) \quad (3.16)$$

where  $-1 < u_{eq} < 1$ . Therefore, based on the mathematical model (3.7) and constant-frequency switching logic presented in Section 3.6.1, some numerical results are discussed below.

### 3.5.3 Experimental Validation

In order to carry out real-time experiment, an experimental setup has been built up (see Figure 3.6). The experimental setup consists of an inverter module, a  $LC$  low pass filter, a  $1-\phi$  load (linear as well as nonlinear), a board consisting of voltage and current transducers, a dSPACE DS1103 R&D controller board with ControlDesk software, and MATLAB/ Simulink.

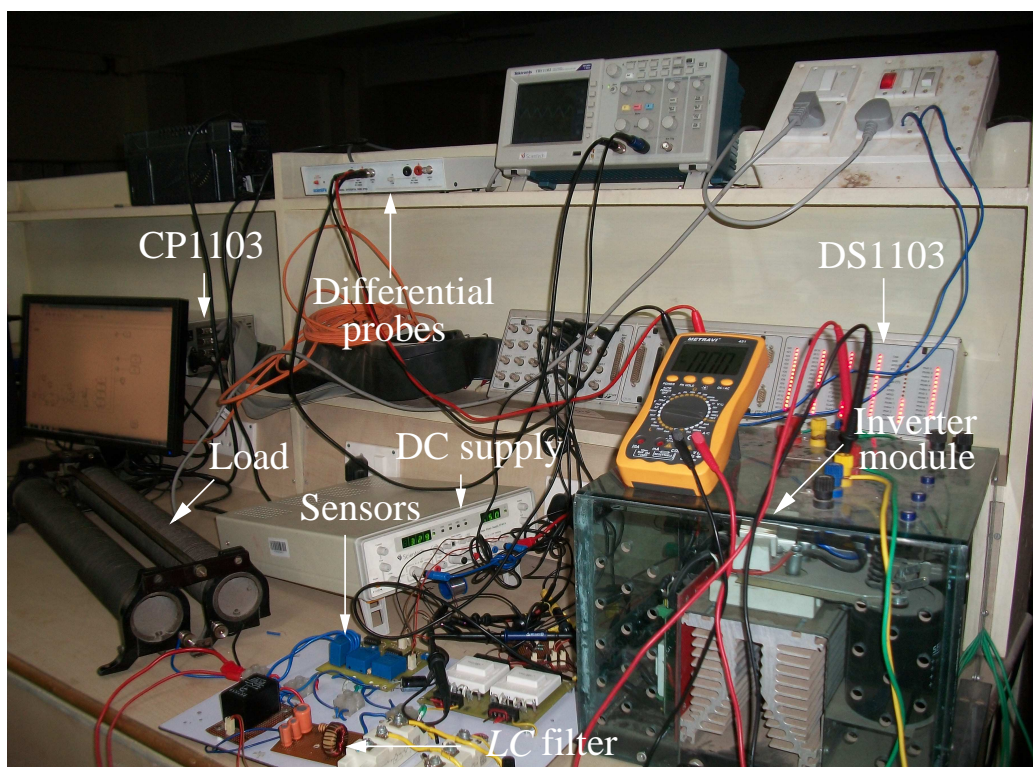


Figure 3.6: Laboratory set-up.

Each of SKM 50GB-123D IGBT module is used as an inverter leg, and is made of two IGBTs with an anti-parallel diode, connected in series. The IGBTs are turned on

by applying a 15 V signal between the gate and the associated emitter and forced open by a -15 V order on the same terminals. These control signal voltages are delivered by the SKHI 22 AR driver through an additional gate resistor of 30 Ohms. These resistors are soldered on the printed circuit board of the drivers. The SKHI 22 A-R drivers are used to operate the IGBT modules. Each driver controls an inverter leg (both “Top” and “Bottom” IGBTs of one single module). These are powered with 0/15 V, and the power supply must be able to deliver a current above the drivers consumption (160 mA / driver max). The error signal is negative logic, i.e., it gives a +15 V signal when no error has occurred. The SKHI 22 A-R is equipped with an internal 10 k $\Omega$  pull-up resistor for protection purposes.

The inductor current and the load voltage are measured for control purposes. Both the measurement circuits consist of a LEM transducer. The LV 25-P and LA 55-NP transducers are used to measure voltages and currents respectively. Both transducers have galvanic isolation between the primary circuit (high power) and the secondary circuit (electronic circuit). The gain of the sensors can be adjusted by using scaling circuits.

The dSPACE system is high performance digital control system based on the MPC-8240 processor and the TMS320F240 DSP processor, a breakout panel and the software tools. It is directly interfaced with MATLAB/SIMULINK running on a PC. A SIMULINK block diagram is converted to real time C and plotting variables in real time in the DSP. The dSPACE Kit used in this work consists of three major components. These are DS1103 controller board, CP1103 connector board and the ControlDesk software [125]. DS1103 controller board is real-time hardware based on PC technology for controller development in various applications. The DS1103 controller board upgrades PC to a development system for rapid control prototyping. This real time interface (RTI) provides MATLAB/Simulink with library blocks for graphical configuration of ADC, DAC, digital I/O lines, incremental encoders, PWM blocks etc. Simulink models can be then easily configured and run by using these RTI blocks. This reduces the implementation time to a minimum. Finally the ControlDesk is a test and experiment software for DS1103 controller development. The ControlDesk manages real-time and Simulink experiments. It performs all the necessary tasks in a single working environment. The sampling frequency of the controller is 200 kHz and the PWM switching frequency is 12 kHz.

### 3.5.4 Performance Analysis

In order to verify the proposed control scheme, the above model has been simulated by MATLAB/SIMULINK. The resonant frequency is taken 1 kHz to design the low pass  $LC$ -filter. The sampling frequency is  $50 \mu\text{sec}$ . The parameters required for simulation of a 1 kVA inverter are:  $E = 250 \text{ V}$ ,  $v_0 = 110 \text{ V (rms)}$ ,  $f = 50 \text{ Hz}$ ,  $f_s = 20 \text{ kHz}$ ,  $L = 1.5 \text{ mH}$ ,  $C = 66 \mu\text{F}$ , load register  $R = 17.5 \Omega$ . All the parameters are chosen to attain the best transient performance of the system.  $\beta_v$  and  $\beta_i$  are selected for considering the electronic circuit's limitation and the values are  $\beta_v = 0.0166$  and  $\beta_i = 0.1$ . The parameter  $\alpha_2$  is chosen to be 0.8 for inner current controller, which keep the tracking performance within the minimum level, and in order to generate the reference current for inner loop, the  $\alpha_1$  is chosen to be 24.8 [124].

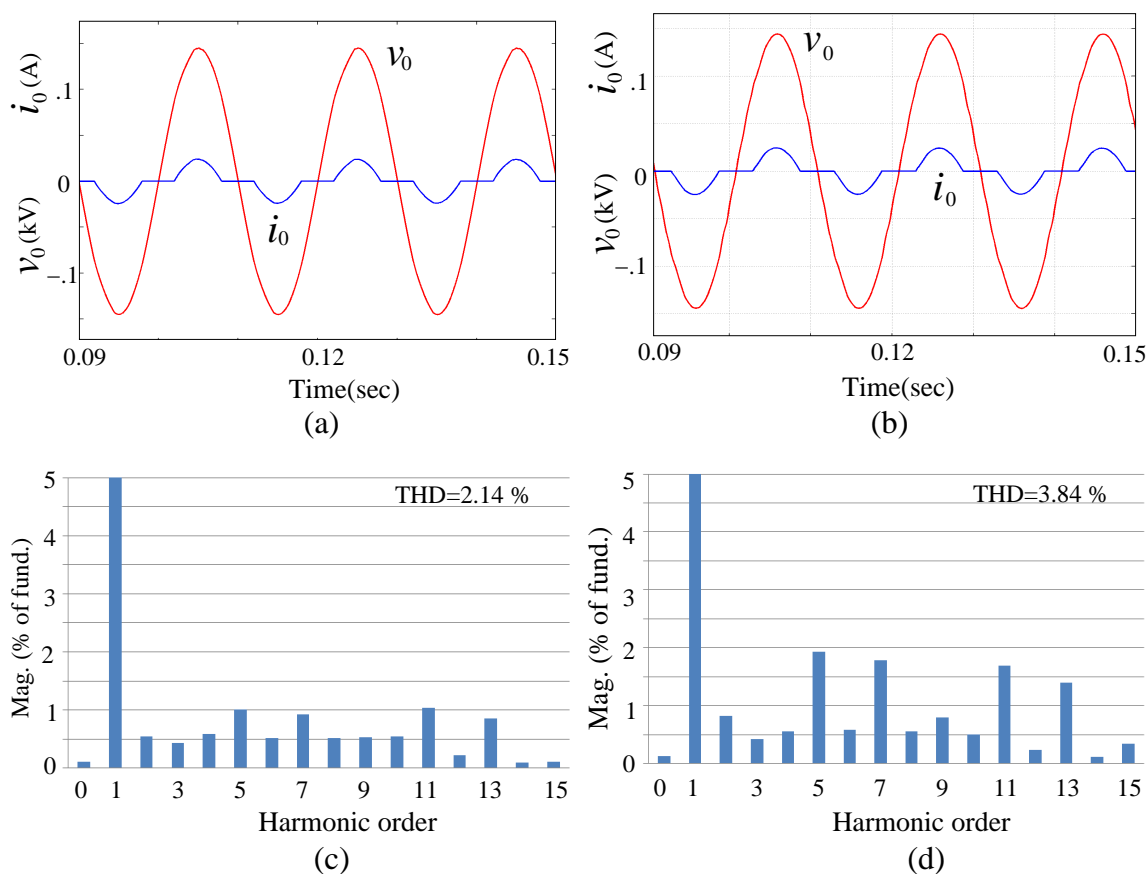


Figure 3.7: Steady state behavior of  $v_o$  and  $i_o$  for a non-linear load. (a) Proposed FFHC controller. (b) PWM voltage controller proposed in [1]. While (c) and (d) are the corresponding harmonic spectrum of the output voltage  $v_o$ .

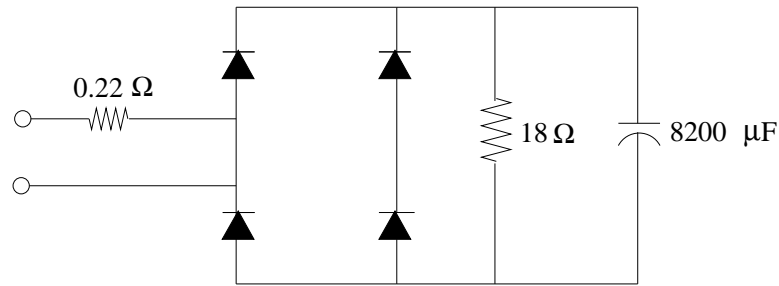
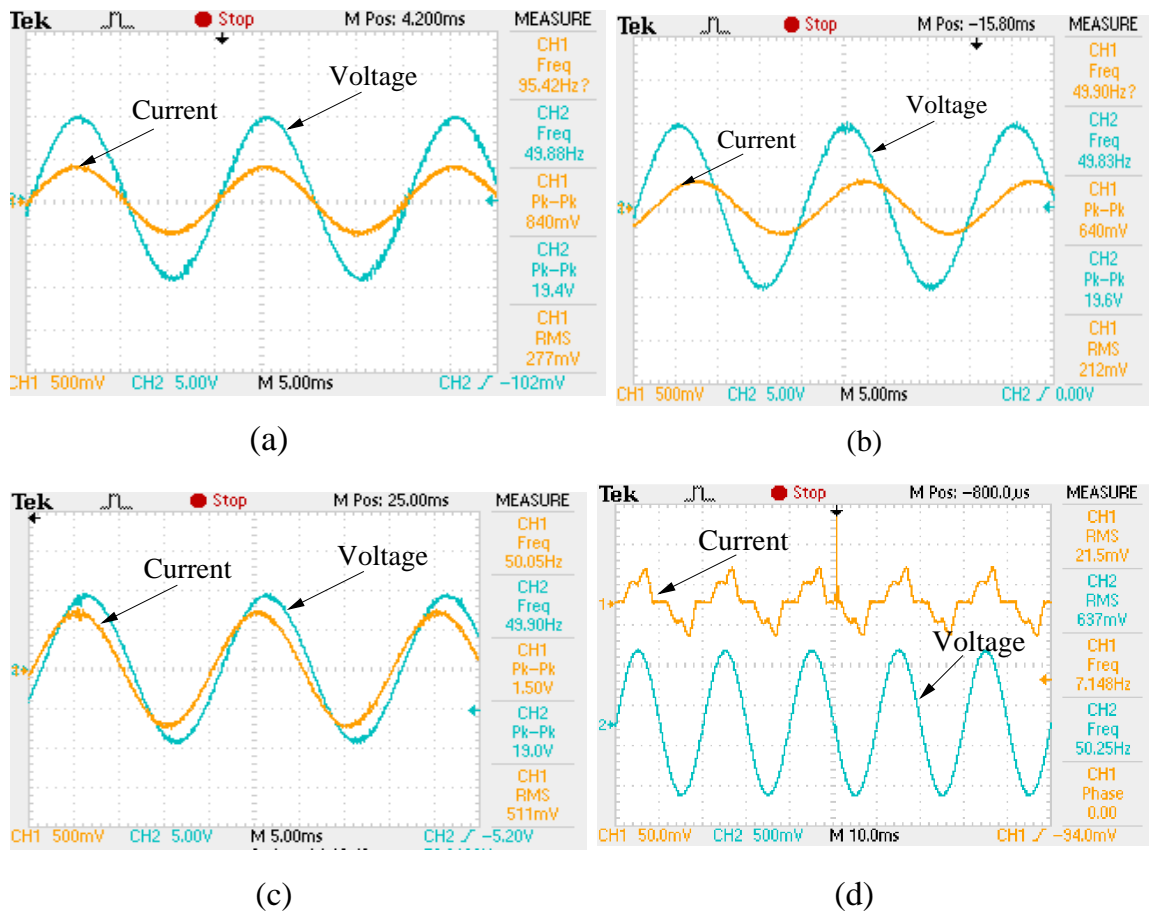


Figure 3.8: Non-linear load according to IEC62040 standards.

Figure 3.9: Steady state response of  $v_o$  and  $i_o$ . (a) *R* load. (b) *RL* load. (c) *RC* load. (d) non-linear load.

The steady state and dynamic performance of the proposed FFHC controller is compared with the carrier based PWM voltage controller [1] for 1- $\phi$  VSI system, under the same load fluctuation. Here all the parameters of both the control schemes are designed as per their optimal performance. The authors [1] used a PI-controller in

the outer voltage control loop to minimize the tracking errors. From the comparison point of view, PI-controller is replaced by a P-controller, as the proposed controller is designed for the same.

Figure 3.9(a) shows experimental waveforms of the steady state output voltage,  $v_0$  and load current,  $i_0$  of the inverter for a resistive load of  $R = 50 \Omega$ . The experimental results agree with those predicted theoretically. The output voltage THD is equal to 1.24%. Figure 3.9(b) and (c) show experimental waveforms of the inverter output current and voltage for inductive load with  $R = 50 \Omega$ ,  $L = 12.7 \text{ mH}$ , and capacitive load of  $R = 50 \Omega$ ,  $C = 100 \mu\text{F}$ . The robustness of the FFHC controller is checked by a full wave uncontrolled rectifier, which has been inserted between the inverter and load as shown in Figure 3.8, so that load becomes non-linear in nature. The steady state response of the proposed controller is compared with the carrier based PWM voltage controller [1]. Figure 4.5(a) and (b) shows the output voltage and current waveforms of the inverter for the non-linear load and the harmonic spectrum of the output voltage waveform of the corresponding controller are shown in Figure 4.5(c) and (d), respectively. The THD were measured to be 2.12% and 3.84% for the two controllers. From these figures it can be observed that, although the load current is heavily distorted but the output voltage suffers a little distortion. The experimental results shown in the Figure 3.9(d) represent the steady state output voltage, and load current of the nonlinear load. The crest factor and the power factor (PF) of the nonlinear load are about 2.75 and +0.7, respectively.

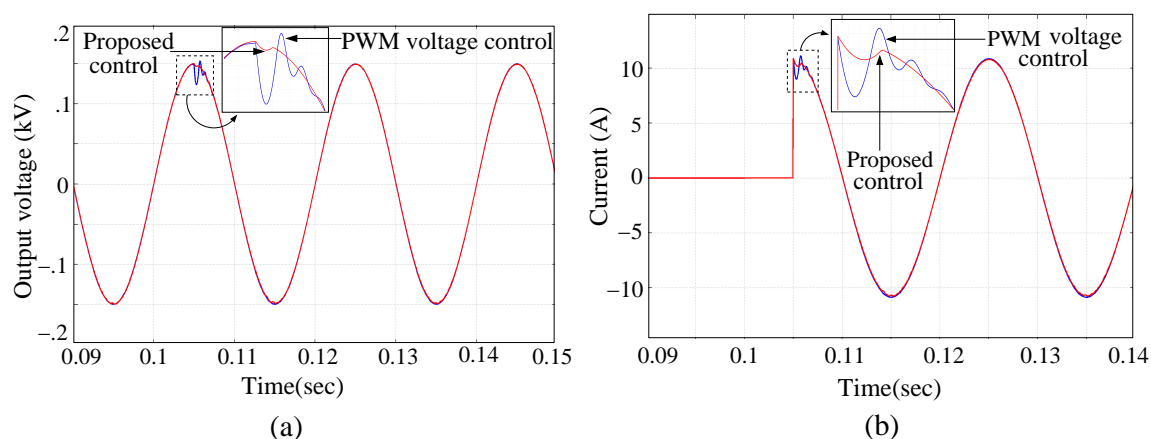


Figure 3.10: Comparison of transient response between the proposed FFHC-controller and PWM voltage controller [1] under step load change from no-load to full load: (a) output voltage  $v_o$ ; (b) load current  $i_o$ .

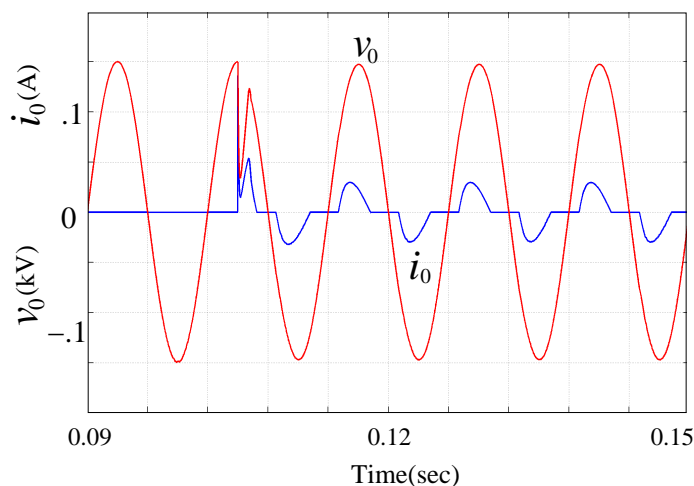


Figure 3.11: Transient output voltage response of the proposed FFHC-controller under nonlinear load change from no load to full load condition.

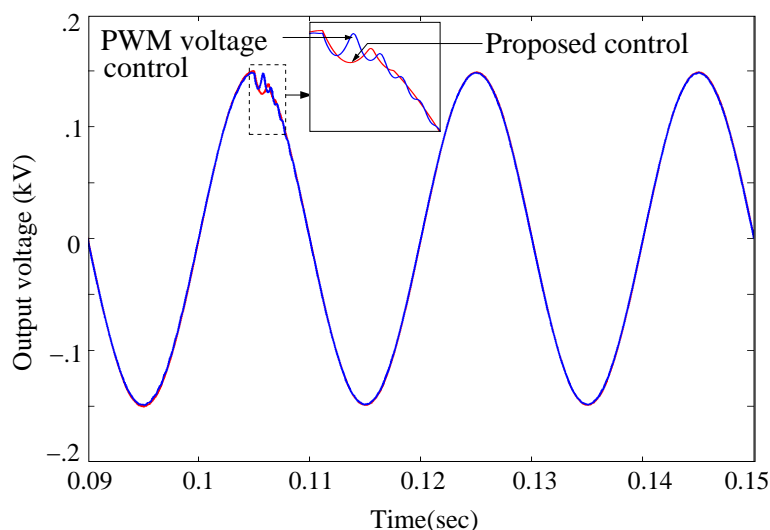


Figure 3.12: Comparison of transient response between the proposed FFHC-controller and PWM voltage controller [1]. The output voltage waveforms under step load change from full-load to no load condition.

The simulation results of the proposed control scheme under step load changes are given to examine the load fluctuation effect. Figure 3.10(a) and (b) shows the responses of the both controllers, under step load change of no-load to full load. From the figures, it is observed that the time taken by the proposed controller to attain the steady state after load change is 0.65 ms whereas for the PWM voltage controller, the output voltage has a settling time of 2.5 ms for the linear load change from zero to

100%. The voltage regulation of 0.8% and 2.45% are noted for the above load change. Figure 3.10(b) shows the transient response of the load currents to distinguish the robustness of the two controllers. The similar type of the above load fluctuation is given for the non-linear load and its voltage response is shown in Figure 3.11. Figure 3.12 shows the dynamic response of the both the controller under step load change from full load to no load. After load fluctuation, the corresponding times required for reaching the steady state are 0.95 ms and .01 s and the voltage overshoot of the proposed controller is very less as compared to the voltage controller, which indicates the superior transient performance of the proposed controller.

### 3.6 Selection of an Ellipsoidal Switching Surface

Here, an ellipsoidal switching surface for the inverter control is taken in phase plane, rather than the time-plot. Since a time varying sinusoidal voltage is taken as the reference voltage, so the sliding surface is no longer a linear relationship between the state variables but the shape is an ellipsoidal. In order to fix-up the varying switching frequency, a constant-frequency hysteresis controller is proposed. The schematic diagram of proposed FFSMC-controlled VSI is shown in Figure 3.13.

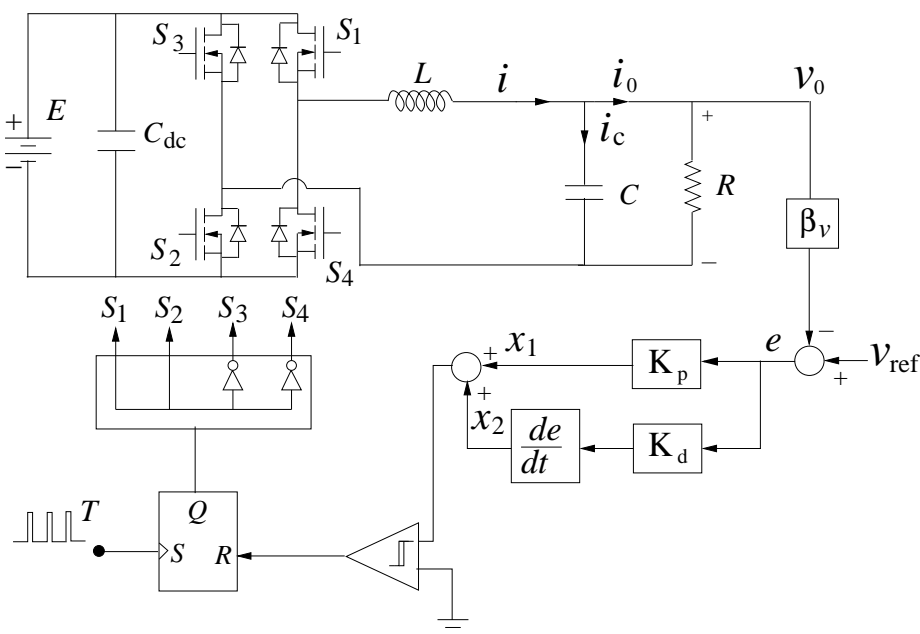


Figure 3.13: The proposed FFSMC-controlled 1- $\phi$  inverter.

### 3.6.1 Dynamics of 1- $\phi$ VSI and Its Mathematical Model

A time independent control scheme can be achieved from a time-dependent one by expressing the switching surface only in terms of the power state variables. The output voltage under steady state is given by

$$\begin{aligned} v(t) &= v_{\text{ref}}(t) = A \sin \omega t \\ t &= \frac{1}{\omega} \arcsin \frac{v}{A} \end{aligned} \quad (3.17)$$

Then the switching surface becomes

$$S(v, \dot{v}) = \dot{v} - A\omega[\arcsin(v/A)] \quad (3.18)$$

by using trigonometric properties, the above can be simplified as

$$S(v, \dot{v}) = \left[ \dot{v} \mp A\omega \sqrt{1 - \left(\frac{v}{A}\right)^2} \right] = 0 \quad (3.19)$$

where the  $-$  and  $+$  signs for  $\dot{v} > 0$  and  $\dot{v} < 0$ , respectively. Then (3.19) can be expressed as

$$\begin{aligned} S(v, \dot{v}) &= \dot{v}^2 + \omega^2 v^2 - \omega^2 A^2 = 0 \\ S(v, \dot{v}) &= \left(\frac{v}{A}\right)^2 + \left(\frac{\dot{v}}{\omega A}\right)^2 - 1 = 0 \end{aligned} \quad (3.20)$$

Equation (3.20) represents a canonical expression of an ellipse in  $(v, \dot{v})$  plane with center at  $(0, 0)$  and x-intercept and y-intercept  $A$  and  $A\omega$  respectively. So by choosing the switching surface (3.20), the desired ac output will be obtained over the surface  $S(v, \dot{v}) = 0$ .

Now, let us define the state variables as  $x_1 = \beta_v v$  and  $x_2 = \beta_v \dot{v}$ . By considering the sensor gain  $\beta_v$ , the switching surface (3.20) becomes

$$S(x) = \frac{x_1^2}{A^2} + \frac{x_2^2}{\omega^2 A^2} - 1 = 0 \quad (3.21)$$

The above sliding surface has two states;  $v$  and  $\dot{v}$ . Since the state  $\dot{v}$  gives the current information, so the sensorless operation is possible to implement this current control scheme. Then, the system dynamics in canonical state variables form can be written as

$$\begin{pmatrix} \frac{dx_1}{dt} \\ \frac{dx_2}{dt} \end{pmatrix} = \begin{pmatrix} 0 & 1 \\ -\frac{1}{LC} & -\frac{1}{RC} \end{pmatrix} \begin{pmatrix} x_1 \\ x_2 \end{pmatrix} + \begin{pmatrix} 0 \\ \frac{\beta_v}{LC} E \end{pmatrix} u. \quad (3.22)$$



Then for  $u \in (-1, 1)$ , the existence condition and the equivalent control can be derived as per the Utkin theory [119]. The SMC exists in the vicinity of the switching surface  $S(x)$  if the following local reachability conditions  $\lim_{S(x) \rightarrow 0^-} \frac{dS(x)}{dt} > 0$  and  $\lim_{S(x) \rightarrow 0^+} \frac{dS(x)}{dt} < 0$ , or  $\lim_{S(x) \rightarrow 0} \frac{dS(x)}{dt} S(x) < 0$  are simultaneously satisfied. The existence condition can be derived by simply substituting the time derivative of  $S(x)$

$$\frac{dS(x)}{dt} = \frac{\partial S(x)}{\partial x} \frac{dx}{dt} = \begin{cases} J \frac{dx}{dt} > 0 & \text{if } S(x) < 0 \\ J \frac{dx}{dt} < 0 & \text{if } S(x) > 0 \end{cases} \quad (3.23)$$

into this condition, where  $J = \frac{\partial S(x)}{\partial x} = \left[ \frac{2x_1}{A^2} \quad \frac{2x_2}{(A\omega)^2} \right]$ . Replacing (3.22) into (3.23) and applying the control law (3.20), the existence region of SMC can be expressed by

$$\lambda_1 = \frac{2k_d^2}{A^2 C R \omega^2} x_2 \left[ \frac{(LC\omega^2 - 1)}{L} R x_1 - x_2 + \frac{\beta_v \cdot R}{L} E \right] \text{ for } u = 1 \quad (3.24)$$

$$\lambda_2 = \frac{2k_d^2}{A^2 C R \omega^2} x_2 \left[ \frac{(LC\omega^2 - 1)}{L} R x_1 - x_2 - \frac{\beta_v \cdot R}{L} E \right] \text{ for } u = -1 \quad (3.25)$$

where  $\lambda_1$  and  $\lambda_2$  are the boundaries of the existence regions. Unlike [126], both the above equations are of the second order with parabolic shape. The limiting boundaries (3.24) and (3.25) give the necessary region of existence region for SMC.

By using the condition  $\dot{S}$  and applying the equivalent control can be found by

$$u_{\text{eq}} = \frac{\frac{1}{C} \frac{di_c}{dt} + \frac{1}{LC} v - \omega^2 \cdot v}{\frac{1}{LC} \cdot E} \quad (3.26)$$

So, this  $u_{\text{eq}}$  control assures the feasibility of the SMC over the switching surface  $S(x, t)$

Therefore, after obtaining the mathematical model (3.21) and (3.22) and constant-frequency switching logic presented, some numerical results are discussed.

### 3.6.2 Performance Analysis

In order to verify the proposed control scheme, the above model has been simulated by MATLAB/SIMULINK. The resonant frequency is taken 1 kHz to design the low pass

$LC$  filter. The sampling frequency is  $50 \mu\text{sec}$ . The parameters required for simulation of a 1 kVA inverter are:  $E = 250 \text{ V}$ ,  $v_0 = 110 \text{ V(rms)}$ ,  $f = 50 \text{ Hz}$ ,  $f_s = 20 \text{ kHz}$ ,  $L = 1.5 \text{ mH}$ ,  $C = 66 \mu\text{F}$ , load register  $R = 17.5 \Omega$ . All the parameters are chosen to attain the best transient performance of the system.  $\beta_v$  is selected for considering the electronic circuit's limitation and the value is  $\beta_v = 0.0454$ . The parameter  $k_p$  and  $k_d$  are chosen to be 11.8 and  $10^{-4}$  respectively which keep the tracking performances within the minimum level.

The phase plane plot of the output voltage  $v_0$  and the voltage derivative  $\dot{v}$  are shown in Figure 3.14(a) under the proposed ellipsoidal surface SMC on full load condition. The system trajectory shown in this Figure moves along the curved switching surface with a switching frequency of the clock pulse. The steady state response of the output voltage and load current are shown on Figure 3.11(b). The

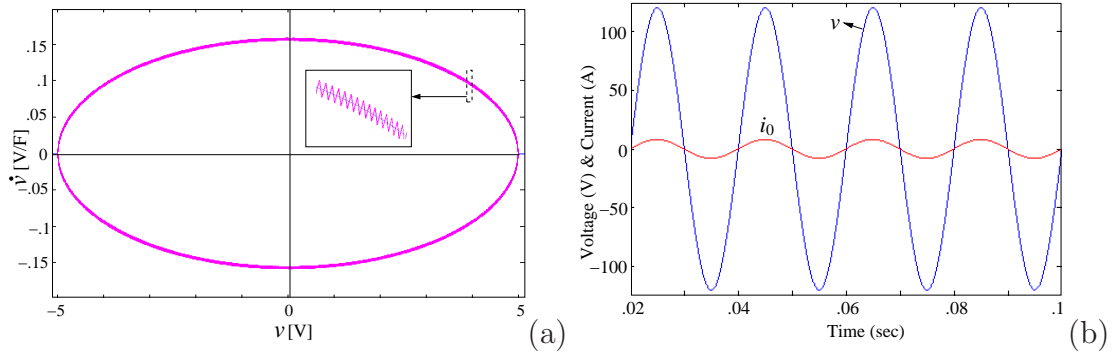


Figure 3.14: Steady state response at the rated load. (a) Phase plane plot under proposed ellipsoidal switching surface. (b) Time plot of the of the output voltage and load current.

THD of the output voltage is found about 0.73% at the full load condition. A 1 kVA single-phase full-bridge inverter prototype has been built and the proposed control scheme has been applied to the prototype. The digital controller is implemented by the help of dSPACE 1103. Parameters of the circuit system are same as the simulation parameters. Figure 3.15(a) and (b) demonstrates the output voltage waveform together with the load current waveform for resistive and nonlinear load which match the simulation results fairly well.

The simulation results of the proposed control scheme under step load changes are verified in phase plane to examine the load fluctuation effect. Figure 3.16 shows the responses of the controller under step load fluctuation by taking the ellipsoidal switching surface.

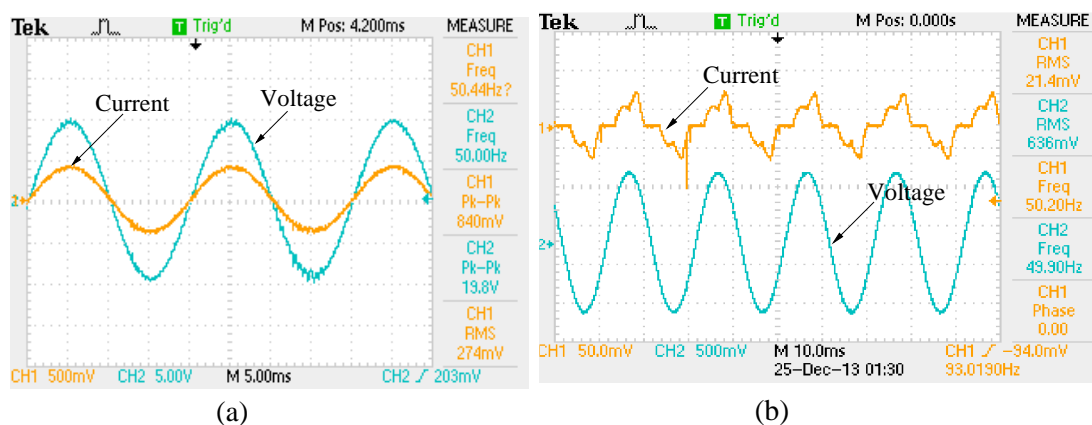


Figure 3.15: Experimental results for  $v_0$  and  $i_0$  in steady state. (a)  $R$  load. (b) Non-linear load.

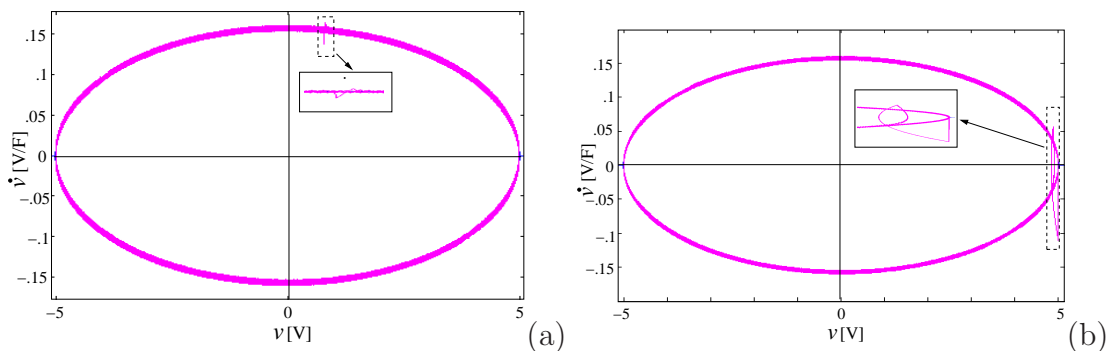


Figure 3.16: The system trajectory under load fluctuation. (a) Hitting in the existence region. (b) Hitting in the non-existence region.

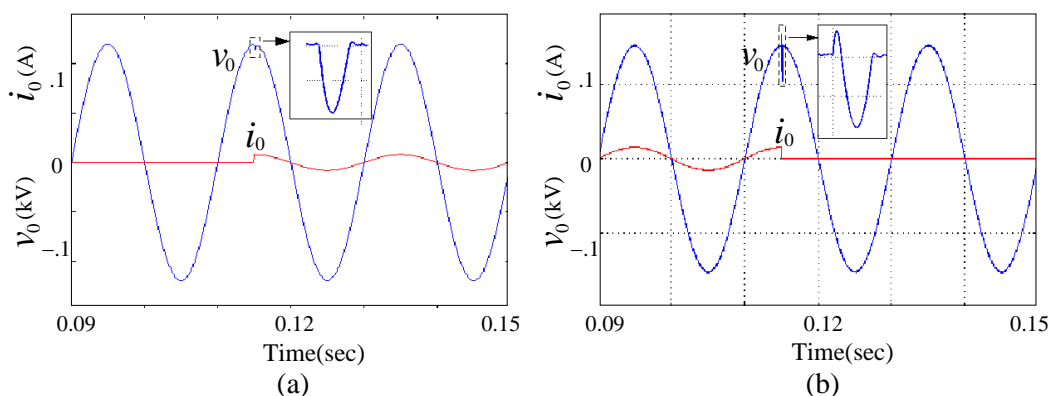


Figure 3.17: Transient response of the output voltage and load current of the proposed controller under step load change from : (a) no-load to full load; (b) full load to no-load.

The system trajectory defined in (3.21) takes a long time to settle when the fluctuation occurs at outside of the existence region whereas it will quickly settle at inside the existence region. Similarly Figure 3.17 shows the dynamic response of the controller under step load change of no-load to full load and full load to no load respectively. From the figures, it is observed that the time taken by the proposed controller to attain the steady state after load change is 0.6 ms and 0.85 ms for the above two cases.

### 3.7 Conclusion

In this chapter, two nonlinear current controllers are proposed on the basis of SMC technique for a 1- $\phi$  full bridge VSI. Since SMC produces a huge chattering problem, so a hysteretic function is employed to generate the switching law for both controllers. A fixed frequency operation of the inverter is achieved by a simple flip-flop with the externally driven constant frequency clock pulse. In the first case, the FFHC controller is implemented through two nested control loops. The outer voltage loop generates the reference current for the inner current loop. The inner current loop is used to generate the control pulses for the inverter. However, the second SMC controller has only one voltage loop. Here the reference voltage is compared with the load voltage and the error signal is passed through proportional-derivative controller. Since the derivative of the error signal gives the current information, so no current sensor is required to implement this control scheme. From the simulation and experimental results, it can be concluded that both the controller not only give better voltage regulation but also exhibit good dynamic performance under sudden load fluctuation. For the sake of simplicity, it has taken a dc voltage source as the inverter input supply. Moreover, these control scheme are also applicable to the islanded distribution generation (DG) system, powered by the renewable energy sources like pv system, fuel cell system etc.

# Chapter 4

## Single -Phase Grid-Connected Inverter System

A PV system can be connected to the utility grid, injecting power into the grid besides providing power to their local loads. In this chapter, the  $1-\phi$  VSI is interfaced with the utility grid. It is important to inject a low THD current from VSI system to grid at unity power factor. This can be achieved by using a phase lock loop (PLL), which collects the grid voltage phase information and produces the reference current for the inverter. As nonlinear loads are dominant in VSI systems which suffer from power quality problems. These local loads produce high THD of the inverter output voltage. These THD have to low as per the IEEE standard 1547. The grid-connected inverter (GCI) system can be operated either in grid connected or in stand-alone mode. The GCI systems are normally operated in grid connected mode; however it can also be operated in stand-alone modes in order to supply power to the emergency load during outages. So, change in operation mode from the grid connected to stand-alone mode and vice-versa is also a challenging task for a GCI system. In this chapter, the detail analysis and design of a  $1-\phi$  inverter system including inductor-capacitor-inductor (*LCL*) filter, and the phase-lock loop (PLL) design will be discussed. A proper controller will be designed to meet the above power quality issues as well as to achieve the seamless transfer operation.

### 4.1 $1-\phi$ GCI System

The single phase grid interactive inverter system is shown in Figure 4.1. It comprises of a dc supply voltage  $E$ , a full bridge VSI, an *LCL* filter with local loads and a utility

grid of voltage  $v_g$ . The  $LCL$  filter composes of the inverter side inductor  $L_1$ , capacitor  $C$ , and a grid interfacing inductor  $L_2$  connected through a static transfer switch (STS). The local sensitive loads are generally connected with the filter capacitor in a parallel manner. The switches of the bridge inverter are controlled by the FFHC control logic, which is implemented by means of a cascaded feedback controller. The currents  $i_1$  and  $i_2$  are called the filter inductor current and grid interfacing current (termed as grid current in this paper) respectively. The STS is used for grid-on and grid-off control. When the STS is closed, the inverter is operated in grid-connected mode. Under any abnormal grid condition or utility interruption, the STS has to open. So the inverter is operated in islanding mode and it supplies the power to the emergency load. A seamless transfer between both modes [127] is used without changing the controller configuration.

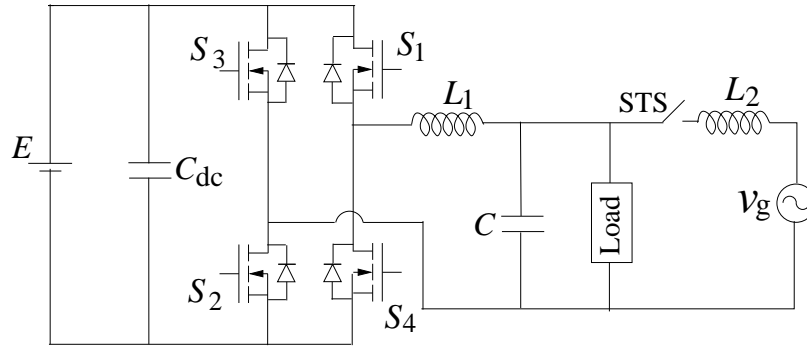


Figure 4.1: 1- $\phi$  grid-interactive inverter system.

### 4.1.1 Grid-Connected Filter Topologies

In order to supply a sinusoidal line current to the grid without harmonic distortion, the inverter is connected to the supply network via a filter. The filter is an important part of every switching converter. The parameters like efficiency, weight and volume have to be considered when choosing an optimal filter topology [51]. Regarding efficiency, filter topologies with reduced losses are required, though those are relatively small when compared to losses in the inverter. Weight and volume of filters are considered as critical due to difficulties with inverter transportation, installation and maintenance. Generally,  $L$ -filter and  $LCL$ -filter topologies are used in grid-connected inverter system.

Small-capacity grid-connected inverter usually utilizes  $L$ -type filter for its simplicity. In a large system, however, such simple  $L$ -type filter is bulky and costly

due to the large current capability. Although this topology has one inductor only, the system dynamics is poor due to the voltage drop across the inductor causing long time responses. Moreover, the inverter switching frequency must be high to attenuate the switching harmonics [51], [128]. Compared to  $L$ -type filter, the same amount of switching ripple reduction can be achieved with smaller inductors by the LCL filter. In summary, compared to the  $L$ -filter, the  $LCL$ -filter configuration allows more flexible inverter usage and also provides more attenuation of switching ripple. However, it is more complicated when using the  $LCL$ -filter; many design considerations, like the location of current feedback selections and component selections, need to be taken into account.

Two different current feedback schemes are possible to use; inverter side inductor current feedback and grid side inductor current feedback. In terms of the low-frequency characteristics, both of the two feedback schemes almost have no difference. This is because the reactance of the filter capacitor is very large at low frequency such that the inverter side current is approximately equal to the grid side current, except for the switching frequency ripples. Nevertheless, once considering the high-frequency characteristics of the two feedback schemes, particularly the  $LC$  resonance, these two current feedback schemes will become totally different. In order to optimally design the  $LCL$ -filter to achieve lowest cost size, it is also necessary to examine both of the two feedback schemes respectively.

The design procedure of the  $LCL$  filter is described as following. First, the selection of the inverter-side inductor  $L_1$  should compromise the output current performance, system cost, size, and efficiency. For example, with a higher  $L_1$  value, lower current ripple can be obtained and a higher controller gain can be designed to obtain better current performance. However, a higher inductance value requires higher cost and occupies a larger volume. For the efficiency concern, higher inductance allows lower current ripple in the inductor  $L_1$ , which decreases core losses of the inductor. On the other hand, higher inductance value increases the winding loss for longer wire required.

The selection of capacitor value depends on the application of inverters. If the inverters are used for only grid-connected applications, the selection of  $C$  can be determined by limiting the reactive power consumed in  $C$  [129]. It is noteworthy that the selection of higher capacitance, the more reactive power is circulating between the inverter and the capacitor, which decreases the inverter efficiency. On the other hand, the selection of the filter capacitor in standalone mode will be determined by the required voltage ripple damping because the inverter-side inductor  $L_1$  and the filter capacitor  $C$  will form a second-order filter that provides a -40dB/dec attenuation after

the resonant frequency of this  $L_1 - C$  filter.

Calculation of The grid-side inductor value can be calculated from the resonance frequency of the  $LCL$  filter based on the requirement for grid-current switching ripple attenuation. The value of  $L_2$  can also be found from the inverter to grid side inductance factor [130], [51].

The value of  $L_1$ ,  $L_2$ , and  $C$  can be found from the following expressions [130], [51], [129]

$$L_1 = \frac{E}{16f_s\Delta i_1}, L_2 = rL_1, C = 0.05\frac{P}{\omega_g v_g} \quad (4.1)$$

where  $E$ ,  $f_s$ ,  $\Delta i_1$ , and  $r$  are the dc input voltage, switching frequency, allowable ripple current through  $L_1$ , and inverter to grid side inductance factor respectively.

## 4.2 State-of-the-Art of Current Controllers

The GCI systems can be operated either in grid-connected or in stand-alone mode. The GCI systems are normally operated in grid-connected mode; however it can also be operated in stand-alone modes in order to supply power to the emergency load during outages. Generally, the inverters connected in the micro-grid act as current sources in grid-connected mode and as voltage sources in islanded mode [131]. This comprises the change of the controller configuration with the change of operation from the grid-connected to islanded mode and vice-versa [127]. When inverters are operated as voltage sources, then the change of the controller is not required by changing the operational mode. Many Seamless transfer controllers were proposed by changing the references of the controllers without changing controller structure [132]. All the above controllers have parallel control structure comprising of a grid side current controller and an output voltage controller. The active and reactive power controls are two important aspects of the grid-connected inverters or micro-grid [133].

As nonlinear loads are the dominant in distributed generation (DG) systems, the micro-grid suffers by power quality problems [134]. These local loads produce high total harmonic distortion (THD) of the inverter output voltage as well as the current exchanged from inverter to grid. These THD have to low as per the IEEE standard 1547. Many literatures were reported to obtain low load voltage THD [135] or low grid side current THD [136] in the grid-connected system. However, hardly any control strategy has been proposed to achieve the low THD of the grid current and inverter load voltage simultaneously. A nested control structure comprising of a current and



voltage control loops is proposed in this paper to overcome the above problems. The outer current controller in grid side is used for the power quality of the grid current; whereas the voltage controller is used for the power quality of the inverter output voltage. The *LCL* filter used in the system can be split into two separate parts. The *LC* filter part is required to design the voltage controller loops whereas the grid interfacing inductor *L* is required to design the outer current controller. All the controllers are implemented in the stationary reference frame.

It is notable stressing that the proposed cascaded control structure improves the dynamic response, power quality of both inverter load voltage and the grid current and attains the seamless transfer operation. In the recent past, several control strategies have been reported like conventional PI controller [137], proportional-resonant (PR) controller [138], deadbeat controller [139], repetitive controller [140], to fulfill the aforesaid requirements. However, these linear controllers can only fulfill partially. On the other hand, as a non-linear control scheme, namely, sliding mode control (SMC) has commonly been used in grid-connected inverter system since it is well known for its robustness, guaranteed stability and good dynamic response over wide range of operating conditions [141]. The SMC utilizes a switching control law to drive the state trajectory from any initial positions to a specified surface in the state space called sliding or switching surface, and maintain it on this surface for all subsequent time [119]. However, SMC operates at variable switching frequency at which an undesirable chattering phenomenon may occur. In order to compensate the above drawback partially, the SMC are realized by means of a hysteresis comparator [120], which also provides a variable switching frequency. So, it produces an undesired harmonic spectrum, for which, designing of the filter components is very difficult. Several authors have proposed constant frequency SMC by means of a variable width hysteresis controller [121], which can however lead to a complex analog implementation, thereby involve more cost. Moreover, the width of hysteresis band depends on the converter parameters. Alternatively, fixed frequency SMC can also be achieved by comparing an external ramp signal to the switching surface [122]. But, the switching instant for these controllers does not depend on the switching surface behavior.

In this work, a cascaded SMC scheme is proposed to improve the dynamic response of a  $1-\phi$  inverter subjected to a sudden fluctuation of load. The proposed controller is designed on the basis of SMC technique. A hysteresis band is employed to generate the switching law for the inverter circuit and that has been implemented using a simple flip-flop with externally driven constant frequency clock pulses. In spite of this constant frequency switching operation, it also retains all of the properties of an ideal

SMC; that is, simplicity in design and good dynamic response.

### 4.2.1 Proposed Control Scheme

The control scheme of the grid-connected inverter system is shown in Figure 4.2. The main objective of this controller is to improve the dynamic performance of the inverter as well as to achieve low THD for the local load voltage  $v_0$  and the grid current  $i_2$  simultaneously. Since the  $LC$  filter and the grid interfacing inductor  $L_2$  are cascaded together, so a cascaded controller is suitable for mitigating the above power quality issues. The proposed controller consists of three loops: an outer current loop to regulate the grid current  $i_2$ , so that it exactly in phase with the grid voltage, and also used for grid synchronization, the voltage loop to control the local load voltage of inverter with low THD, and an inner current control loop to improve the dynamic performance of the inverter by sensing the inverter side inductor current  $i_1$ . Here no controller is required to control the dc link voltage, as it is assumed that inverter is powered by a constant dc voltage source. In this paper, a fixed frequency hysteretic controller is designed on the basis of SMC, due to its robustness towards the wide parameter variation. The fast inner current loop is used to produce the control signal and then a hysteresis band is employed to generate switching laws for the VSI. But the use of hysteresis comparator involves variable switching frequency operation. So constant switching frequency operation can be implemented by using a simple flip-flop with externally driven clock pulses. The main role of this control loop is to improve the dynamic performance of the VSI under wide load fluctuations.

The prime roles of the voltage controller are; to address the power quality problems of the inverter local load voltage for all types of loads, so that the THD of the load voltage should be below the IEEE standard 1547. This controller is also used for synchronization of the inverter with the grid. Once both are synchronized, then the voltage and the frequency are decided by the grid.

The role of the outer current controller is to communicate a low THD current between the inverter to grid and vice-versa even in the presence of the distorted grid voltage and nonlinear local loads of the inverter. A phase lock loop (PLL) is generally used to synchronize the inverter with the grid. The commonly used d-q PLL [132], which collects the grid voltage phase information and produces the reference current  $i_{\text{ref}}$  for the outer current loop.  $H_v$  and  $H_{i_2}$  are the sensor gains of the grid voltage and injected grid current, respectively and a PI controller is used to regulate the grid current. The current  $I^*$  that applied to the outer current loop can be automatically adjusted by the active power controller [142]. But this will not be discussed here,



### 4.3.1 Dynamics of 1- $\phi$ GCI System and Equation of the SS

The dynamical equations of 1- $\phi$  GCI system, as shown in Figure 4.1 can be expressed as

$$\begin{aligned} L_1 \frac{di_1}{dt} &= uE - v_0 \\ L_2 \frac{di_2}{dt} &= v_0 - v_g \\ C \frac{dv_0}{dt} &= i_1 - i_2 \end{aligned} \quad (4.2)$$

where  $u = \pm 1$ , is the control input of the system.

Let us define the state variables of the system as

$$x_1 = i_1, x_2 = v_0, x_3 = i_{\text{ref}} - i_2, x_4 = \int x_3 dt \quad (4.3)$$

where  $i_{\text{ref}} = I_2 \sin(\omega t)$  is the grid reference current, which is set by the user,  $v_{\text{ref}}$  is the reference for the local load voltage, generated by the outer grid current loop and  $i^*$  is the inverter side inductor current reference, generated by the voltage control loop. These are represented by

$$v_{\text{ref}} = L_2 \dot{i}_{\text{ref}} + v_g = L_2 I_2 \omega \cos(\omega t) + v_g \quad (4.4)$$

$$i^* = i_{\text{ref}} + C \dot{v}_{\text{ref}} = I_2 \sin(\omega t) - CL_2 I_2 \omega^2 \sin(\omega t) + C \dot{v}_g \quad (4.5)$$

The system behavior can be represented by following the state-space form.

$$\dot{x} = Ax + Bu + D, x = [x_1 \ x_2 \ x_3 \ x_4]^T, \quad (4.6)$$

where

$$A = \begin{bmatrix} 0 & -\frac{1}{L_1} & 0 & 0 \\ \frac{1}{C} & -\frac{1}{RC} & -\frac{1}{C} & 0 \\ 0 & -\frac{1}{L_2} & 0 & 0 \\ 0 & 0 & 1 & 0 \end{bmatrix}, B = \begin{bmatrix} \frac{E}{L_1} \\ 0 \\ 0 \\ 0 \end{bmatrix}, D = \begin{bmatrix} 0 \\ d_1 \\ d_2 \\ 0 \end{bmatrix}$$

where  $d_1 = \frac{i_{\text{ref}}}{C}$ , and  $d_2 = \dot{i}_{\text{ref}} + \frac{v_g}{L_2}$ . By considering the switching function  $u = 1/2(1 + \text{sign}(S))$ , where  $u$  is the control signal given to the power switches  $S_1 - S_4$ , the sliding

surface of the proposed cascaded controller is chosen by the linear combination of the state variables, i.e

$$S(x, t) = -K_1x_1 - K_1K_2x_2 + K_1K_2K_px_3 + K_1K_2K_px_4 \quad (4.7)$$

or,

$$S(x, t) = \alpha_1x_1 + \alpha_2x_2 + \alpha_3x_3 + \alpha_4x_4 \quad (4.8)$$

where  $\alpha_1 = -K_1$ ,  $\alpha_2 = -K_1K_2$ ,  $\alpha_3 = K_1K_2K_p$ , and  $\alpha_4 = K_1K_2K_i$  are called sliding coefficients.

### 4.3.2 Existence Condition

The three necessary conditions for SMC operation are hitting, existence, and stability conditions. The hitting condition has been discussed till now, by selecting the suitable switching function. As far as existence condition, the SMC exists in the vicinity of an sliding surface  $S(x)$ , if the following local reachability conditions  $\lim_{S(x) \rightarrow 0^-} \frac{dS(x)}{dt} < 0$  or  $\lim_{S(x) \rightarrow 0^+} \frac{dS(x)}{dt} > 0$  are simultaneously satisfied [119]. The reachability condition can be derived by simply substituting the time derivative of  $S(x)$

$$\frac{dS(x)}{dt} = \frac{\partial S(x)}{\partial t} \frac{dx}{dt} = \begin{cases} J \frac{dx}{dt} > 0 & \text{for } S(x) < 0 \\ J \frac{dx}{dt} < 0 & \text{for } S(x) > 0 \end{cases} \quad (4.9)$$

into this condition, where  $J = \frac{\partial S(x)}{\partial t} = \begin{bmatrix} \alpha_1 & \alpha_2 & \alpha_3 & \alpha_4 \end{bmatrix}$ . Replacing (4.6) into (4.9), and applying the control law (4.8), the existence region of SMC can be expressed as

$$\lambda_1 = x_1 \left( -\frac{\alpha_1}{L_1} + \frac{\alpha_2}{C} \right) + x_2 \left( -\frac{\alpha_2}{RC} - \frac{\alpha_3}{L_2} \right) + x_3 \left( -\frac{\alpha_2}{C} \right) + \frac{\alpha_1 E}{L_1} + \alpha_2 d_1 + \alpha_3 d_2 \quad (4.10)$$

$$\lambda_2 = x_1 \left( -\frac{\alpha_1}{L_1} + \frac{\alpha_2}{C} \right) + x_2 \left( -\frac{\alpha_2}{RC} - \frac{\alpha_3}{L_2} \right) + x_3 \left( -\frac{\alpha_2}{C} \right) - \frac{\alpha_1 E}{L_1} + \alpha_2 d_1 + \alpha_3 d_2 \quad (4.11)$$

The limiting boundaries (4.10) and (4.11) give the necessary region of existence for the SMC on smooth sliding surface [119] and set the design range for the sliding coefficients, which should ensure the system to remain in sliding mode operation when the system trajectory is close to the sliding surface.

### 4.3.3 Stability Condition

Generally, the equivalent-control method is adopted for the stability condition of the sliding coefficients, as all the state variables are highly non-linear in nature. The equivalent control  $u_{eq}$ , that is, the ideal control making the sliding flow invariant, provides the ideal dynamics when the system is in sliding mode, and can be viewed as the average control value forcing the system dynamics to remain on the sliding manifold. The equivalent control can be obtained by applying the invariance conditions  $\dot{S}(x, t) = 0$  and  $S(x, t) = 0$ . Using (4.6) and (4.9) and putting  $u = u_{eq}$

$$\frac{S(x, t)}{dt} = J \frac{dx}{dt} = J(Ax + Bu_{eq} + D) = 0 \quad (4.12)$$

$$u_{eq} = -(JB)^{-1}J(Ax + D) \quad (4.13)$$

$$u_{eq} = -\frac{L_1}{CE} \frac{\alpha_2}{\alpha_1} x_1 + \frac{L_1}{E} \left[ \frac{1}{L_2} + \frac{\alpha_2}{\alpha_1} \frac{1}{RC} + \frac{\alpha_3}{\alpha_1} \frac{1}{L_2} \right] x_2 + \frac{L_1}{E} \left[ \frac{\alpha_2}{\alpha_1} \frac{1}{C} - \frac{\alpha_4}{\alpha_1} \right] x_3 - \frac{L_1}{E} \left[ \frac{\alpha_2}{\alpha_1} d_1 + \frac{\alpha_3}{\alpha_1} d_2 \right] \quad (4.14)$$

where  $-1 < u_{eq} < 1$ .

## 4.4 Performance Analysis

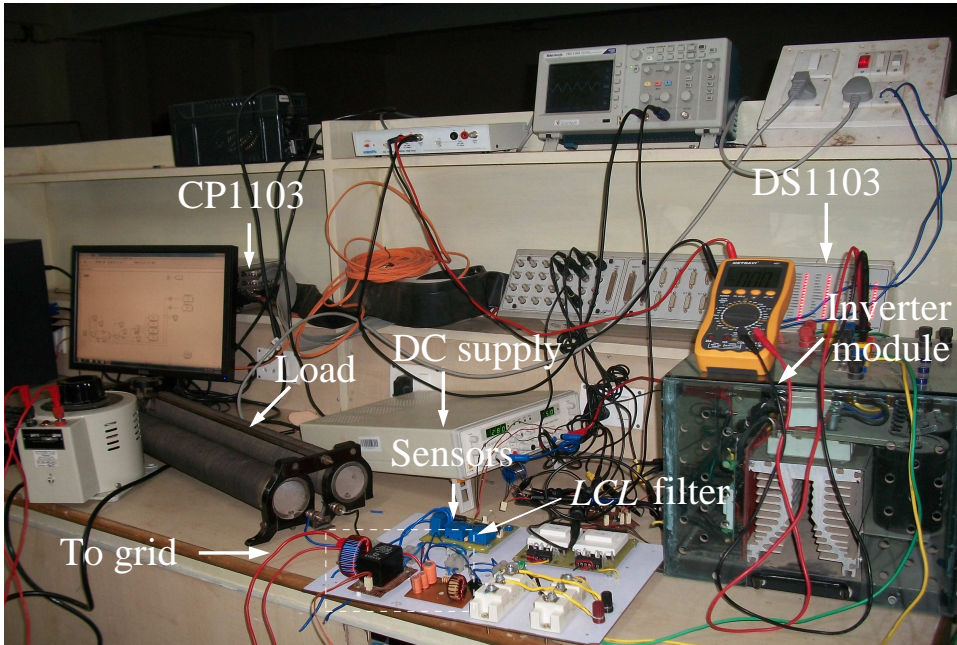


Figure 4.3: Laboratory set-up for grid-connected inverter system.

In order to verify the proposed three loop compensation control scheme, the above model had been simulated by MATLAB/SIMULINK. The resonant frequency was taken 1 kHz to design the low pass  $LC$  filter. The sampling frequency was  $50 \mu\text{sec}$ . The parameters required for simulation of a 1 kVA inverter were:  $E = 250 \text{ V}$ ,  $v_0 = 110 \text{ V(rms)}$ ,  $f = 50 \text{ Hz}$ ,  $f_s = 20 \text{ kHz}$ ,  $L_1 = 1.5 \text{ mH}$ ,  $C = 66 \mu\text{F}$ ,  $L_2 = 1.5 \text{ mH}$ , load register  $R = 17.5 \Omega$ . The performance of the controller was evaluated in both grid-connected and stand-alone modes with various loads. The seamless transfer operation from one mode to another was also carried out. The externally given reference current  $I^*$  was set to zero in stand-alone mode of operation and the STS was turned off. The experiment was performed in the power electronics laboratory with the set-up shown in Figure 4.3

#### 4.4.1 Stand-Alone Mode of Operation

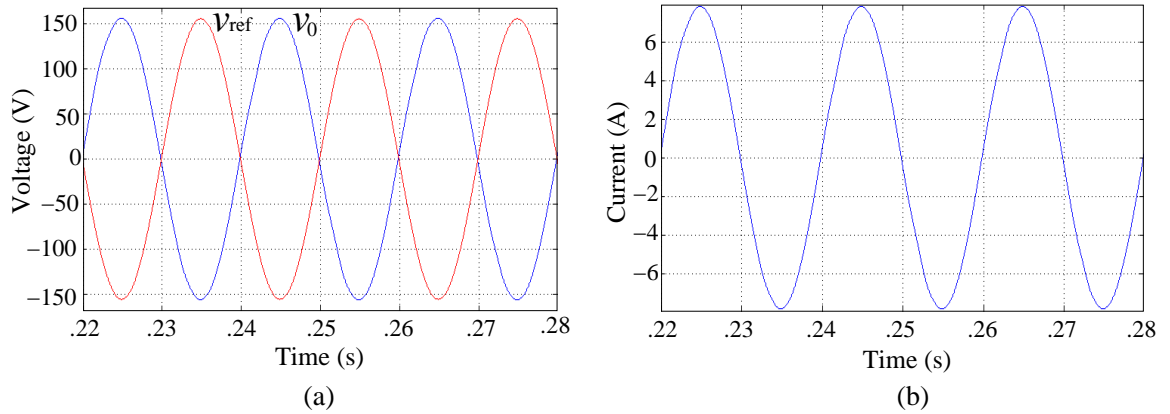


Figure 4.4: Stand-alone mode with a resistive load. (a) Steady-state load voltage  $v_0$ ,  $180^\circ$  shifted reference  $v_{\text{ref}}$ . (b) Load current  $i_0$

Here the outer grid current controller is absent. So, for this mode of operation only two control loops were functioning. The reference voltage for the voltage control loop was fixed to the grid voltage, so that the synchronization of the inverter with the grid could be done and ready to linked with the grid. The proposed cascaded controller can be evaluated for the resistive load ( $R = 17.5 \Omega$ ), and a standard nonlinear load of IEC62040. Figure 4.4 shows the steady state response of the local load voltage  $v_0$ , the reference voltage  $v_{\text{ref}}$  and the local load current  $i_0$ . The load voltage  $v_0$  exactly followed the reference voltage (grid voltage) and ready for synchronization. The measured

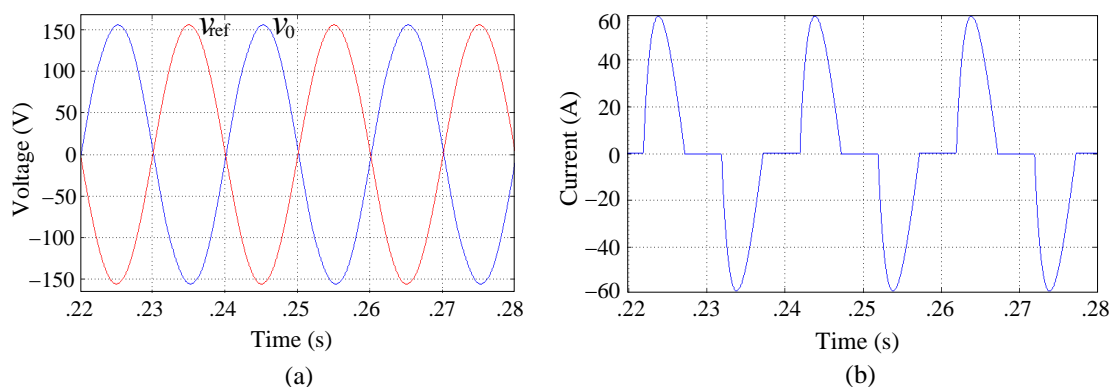


Figure 4.5: Stand-alone mode with the IEC62040 non-linear load. (a) Steady-state load voltage  $v_0$ , 180° shifted reference  $v_{ref}$ . (b) Load current  $i_0$ .

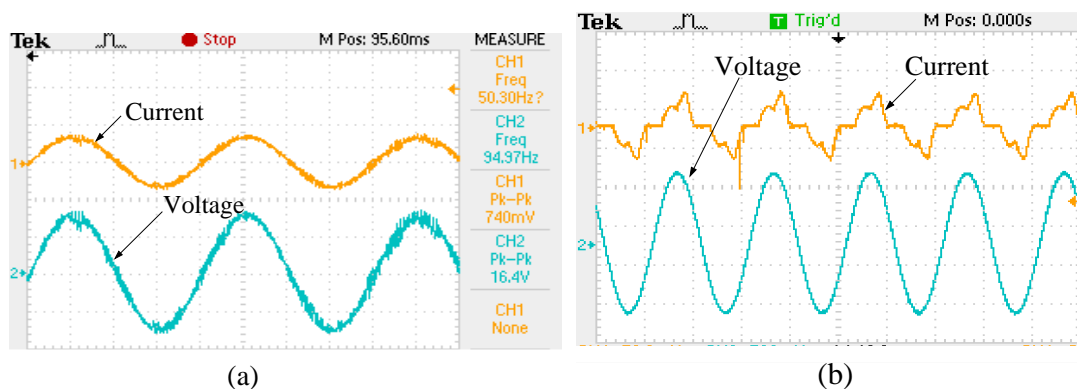


Figure 4.6: Experimental results of  $v_0$  and  $i_0$  in stand-alone mode for: (a)  $R$ -load; (b) non-linear load.

load voltage THD was 0.91%, whereas the load current was 3.75%. Figure 4.5 shows the load voltage and load current waveforms of the inverter for the non-linear load with the measured THD of 2.37% and 30.17% respectively. The steady-state responses are also verified under resistive and nonlinear load through the experiment set up. The control and the line parameters are taken same as the previous experimental set up. The load voltage  $v_0$ , and the load current  $i_0$  for both the cases are shown in Figure 4.6.

The transient performance of the proposed controller in stand-alone mode was evaluated under the large load fluctuation. Figure 4.7 shows the responses of local load voltage and output current under the step load change of no-load to full-load and back. From the figures, it was observed that the time taken by the load current to attain the steady state was 0.45 ms for the linear load change from zero to 100 %, whereas 0.32 ms was required for a step load change from full-load to no-load. so the above results confirmed satisfactory steady-state and transient performance in



the stand-alone mode of operation.

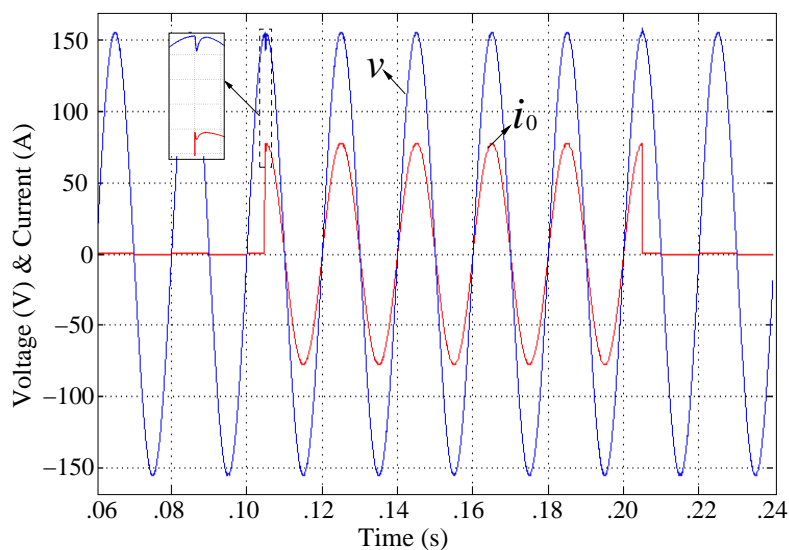


Figure 4.7: Transient response of load voltage  $v_0$ , and load current  $10 \cdot i_0$  for a step load change from open circuit to  $20 \Omega$ , and back.

Table 4.1: steady-state response in grid-connected mode of operation

Controller	Type of load	$i_2$	$v_{\text{ref}}$	$v_0$
Proposed controller	Without load	2.34 %	1.12%	1.74%
	With R-load	1.52 %	1.24%	1.26%
	Non-linear load	3.12 %	1.14%	1.33%

#### 4.4.2 Grid-Connected Mode of Operation

A sinusoidal reference current of 5A (related to 3.54A rms) was set for the outer loop after synchronization of the inverter with the grid. The steady state response for the resistive load and the nonlinear load used in the previous section was repeated again. The case of grid-feeding (when local load is absent, then, the power produced by the inverter was fed to utility grid) was also carried out. Finally, the transient performance under the grid and load side fluctuation was evaluated.

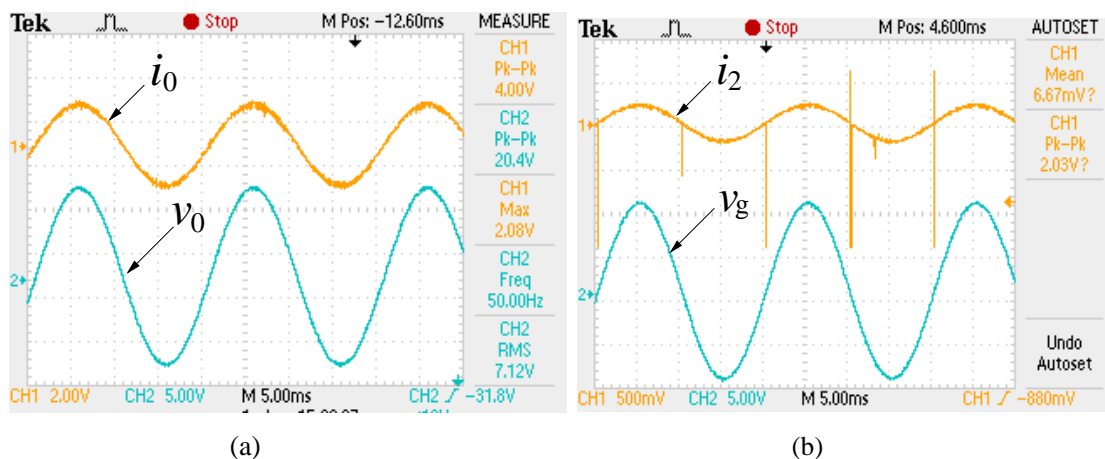


Figure 4.8: Steady state response in the grid-connected mode. (a) Load current  $i_0$  with local load voltage  $v_0$ . (b) Grid current  $i_2$  with the grid voltage  $v_g$ .

In the case of grid-feeding mode of operation, the steady state response of the proposed controller was evaluated in terms of THD. The THD of the load voltage  $v_0$ , the voltage reference  $v_{\text{ref}}$ , and the current fed to the grid  $i_2$  of the controller, under the presence and absence of the local load, was given in Table 4.1. The grid current had THD of 2.34% for the proposed controller, whereas the load voltage THD was 1.74%. From these results, it is concluded that the proposed controller performed

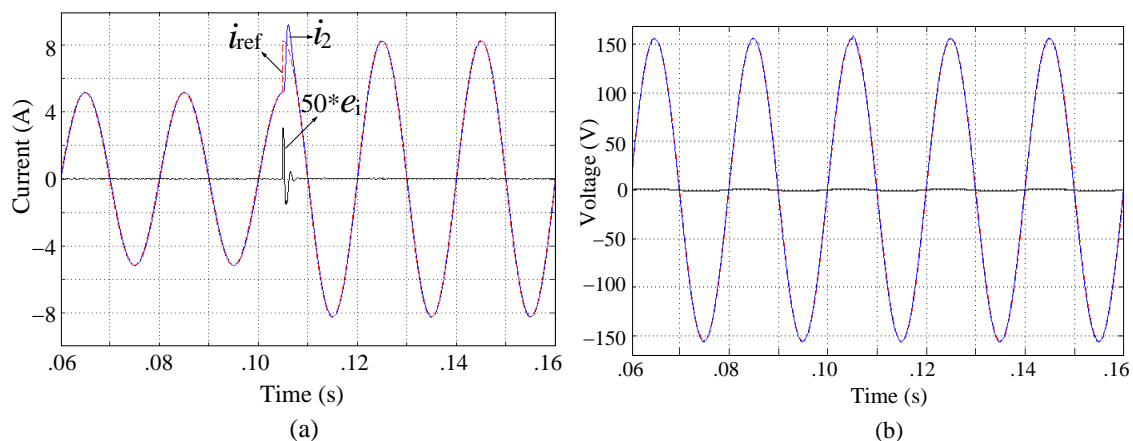


Figure 4.9: Transient response of the proposed controller on the absence of the local load in the grid-connected mode to a step change in  $I^*$ . (a) Grid-current  $i_2$ , the reference current  $i_{\text{ref}}$ , and the current error  $e_i$ . (b) Local load voltage  $v_0$ , the reference voltage  $v_{\text{ref}}$  and the voltage tracking error  $e_v$ .

satisfactorily. The steady state response in the presence of resistive load and non-linear

load was given in same table. Similar kinds of the results were recorded as the results obtained in the absence of local loads. Figure 4.8 illustrates the steady state performance of the proposed controller applied on the GCI prototype. Although the experimental results are less perfect compared to the simulation ones, but they are reasonably good to demonstrate the effectiveness of the proposed control technique.

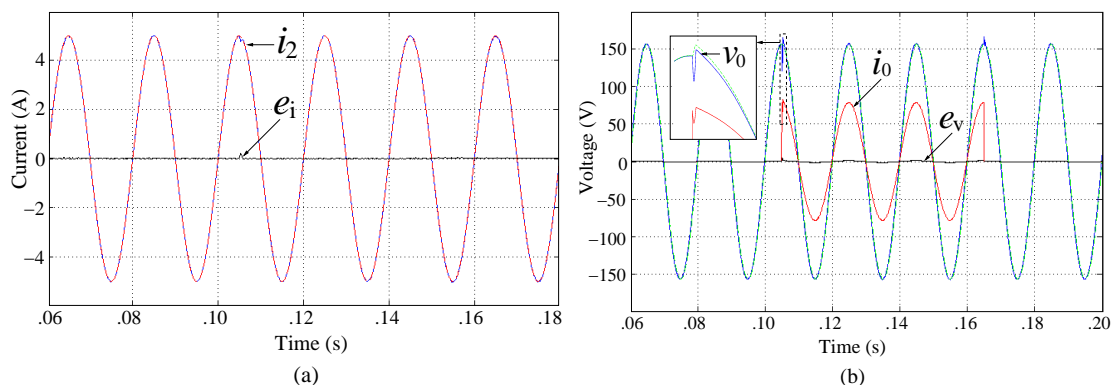


Figure 4.10: Transient response in the grid-connected mode for the step load change from no-load to full load ( $R=20 \Omega$ ) and back. (a) Grid current  $i_2$ , its reference  $i_{ref}$ , and the tracking error current  $e_i$ . (b) Load current  $i_0$ , local load voltage  $v_0$  with its reference  $v_{ref}$ , and the tracking error voltage  $e_v$ .

Transient response of the proposed controller was evaluated under the grid current reference fluctuation on the absence of the local load. A step change of the reference grid current  $I^*$  from 5 A (3.53 A rms) to 8 A (5.66 A rms) was given. Figure 4.9 and represent the reference grid current  $i_{ref}$ , the grid current  $i_2$  and tracking current error  $e_i$  along with the reference voltage  $v_{ref}$ , load voltage  $v_0$ , the error voltage  $e_v$  of the controller. The grid current took 0.1 ms to settle its new value by the proposed controller. There was no noticeable change in load voltage and the results show the proposed controller has the transient response within the IEEE standard. Similar types of results were obtained in the presence of the local load. The transient performance of the proposed controllers was recorded under the local load fluctuation. The grid current  $i_2$  with its reference current and the current tracking error  $e_i$  as well as the load voltage  $v_0$ , load current  $i_0$  were shown in Figure 4.10 under the resistive load change from no-load to  $R = 20 \Omega$  at  $t = 0.105$  s and back at  $t = 0.165$  s. The load current took about 0.5 ms and 0.1 ms to settle down for the above load variations. There is no remarkable change in grid current.

## 4.4.3 Seamless Transfer Mode of Operation

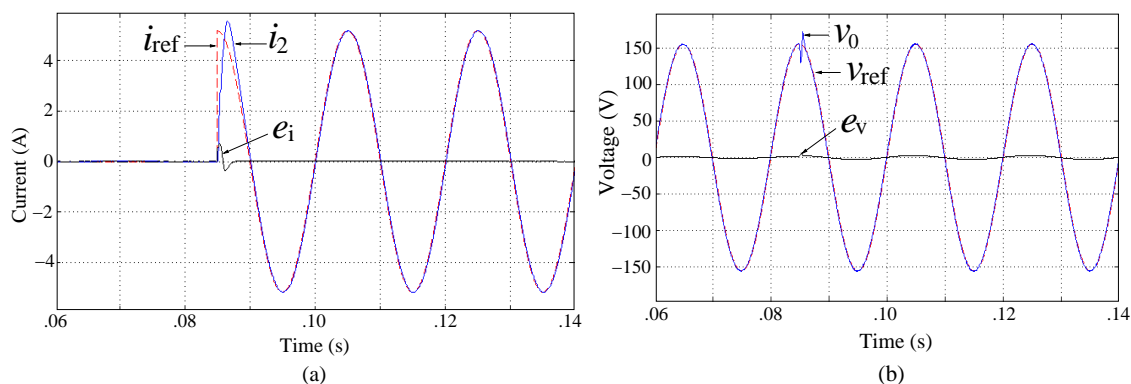


Figure 4.11: Seamless transfer response from stand-alone to grid-connected mode at  $t = 0.085$  s. (a) Grid current  $i_2$ , its reference  $i_{ref}$ , and the tracking error current  $e_i$ . (b) Local load voltage  $v_0$  with its reference  $v_{ref}$ , and the tracking error voltage  $e_v$ .

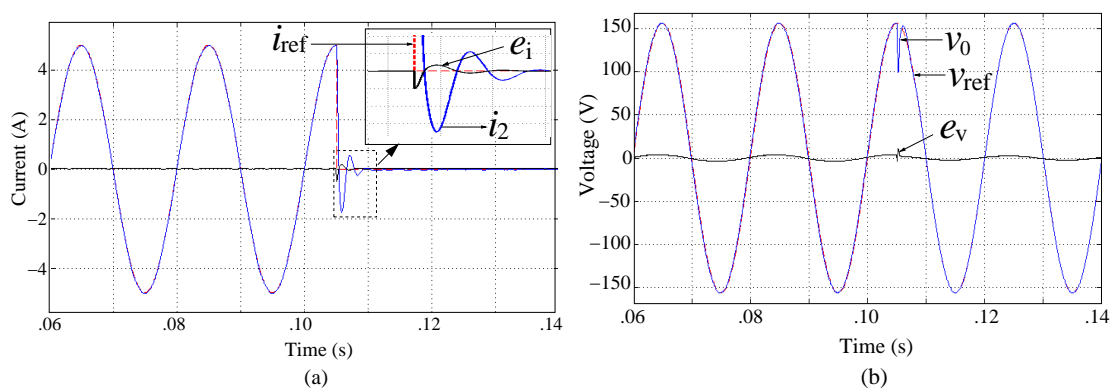


Figure 4.12: Seamless transfer response from grid-connected to stand-alone mode at  $t = 0.105$  s. (a) Grid current  $i_2$ , reference current  $i_{ref}$ , and its tracking error current  $e_i$ . (b) Local load voltage  $v_0$ , reference voltage  $v_{ref}$ , and tracking error voltage  $e_v$ .

The seamless transfer between grid-connected and standalone modes can be achieved by matching the load voltage with the grid voltage in terms of magnitude, frequency, and phase. Figure 4.11 gives the simulation results changing from stand-alone mode to grid-connected mode at  $t = 0.085$  s. There were not much inrush spikes in load voltage and the grid current during transition period, indicate a smooth seamless transfer from stand-alone to grid-connected mode. For the stand-alone mode of operation, the STS opened and the reference grid current  $I^*$  was removed.

Similarly, the results from grid-connected mode to stand-alone mode are also shown in Figure 4.12. It is observed that the local load voltage and the load current had not any noticeable transient, indicates a smooth transfer from grid-connected to stand-alone mode.

## 4.5 Conclusion

In this chapter, the cascaded SMC strategy has been proposed for the grid-connected inverter system. It consists of two current loops and a voltage loop and offers excellent performance in terms of THD for both inverter output voltage and the grid current, even under the case of the non-linear local load. The dynamic performance of the system is improved by introducing the inner current loop. The controller is designed on the basis of constant frequency SMC. The proposed scheme also achieves seamless transfer between the stand-alone and the grid-connected modes. This strategy can also be used in 3- $\phi$  inverter systems.

## Chapter 5

# Dual-Stage Grid-Connected Photovoltaic System

All the power processing stages, discussed in the previous chapters are combined here to form a GPV system. The PV system can either be connected in Standalone mode or in grid-connected mode. A typical stand-alone PV system comprises of a solar array and a storage device i.e., battery. The battery is used as a backup source for power management between the source and the load. Generally, a Lead-acid battery is used in high power PV applications due to its low cost and availability in large size. The modeling of a lead-acid battery by using the equivalent circuits is discussed here. Three independent control loops are proposed to control the standalone PV system; MPPT control loop for extracting maximum power from PV module, battery control loop for bidirectional power flow between battery and dc-link through buck-boost converter to keep the dc-link voltage constant and inverter control loop for maintaining good voltage regulation and achieving fast dynamic response under sudden load fluctuations. Similarly, a cascaded sliding mode control is proposed for GPV system to regulate the current from PV system to the grid at a lower THD level. The stability of the above controllers is verified by using Bode-diagram.

### 5.1 1- $\phi$ Standalone PV System

The standalone PV system is commonly used in remote areas where the grid is not reachable or is not economical to install. This system can also be suitable for telecommunications units, rural electricity supply, and auxiliary power units for emergency services or military applications. As the solar energy is only possible during

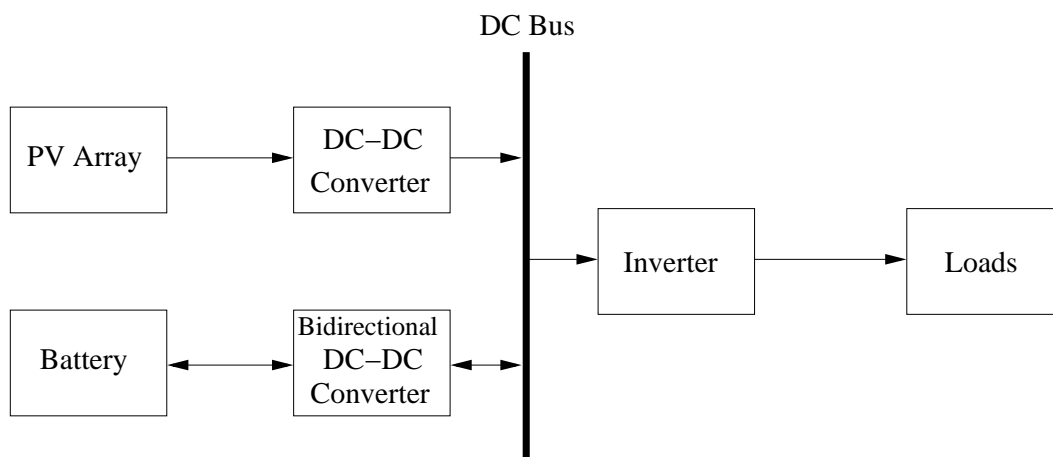


Figure 5.1: Standalone PV system with battery load.

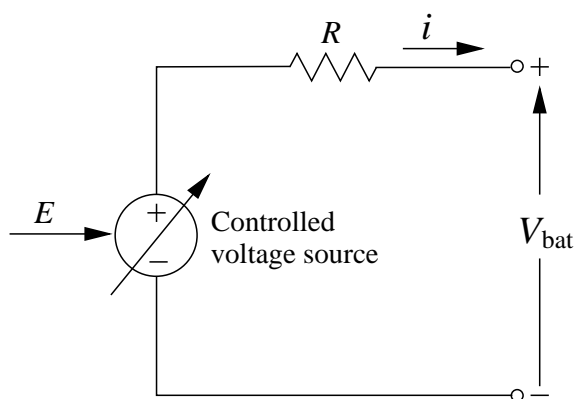


Figure 5.2: Equivalent circuit of a battery.

the daytime, it is very much necessary to store the energy for the night or for cloudy days. A standalone PV system uses lead-acid rechargeable batteries, as the storage device. A basic block diagram of standalone PV system with battery as storage element is shown in Figure 5.1. As battery plays an important role in this mode of operation, so modeling is required to design its charging and discharging control.

### 5.1.1 Battery Modeling

Out of various available models, the equivalent circuit model is commonly used for dynamic simulation [143], [144]. Battery possesses high energy density and can provide power at almost constant voltage. In this work a lead-acid battery is used as it is more convenient for renewable systems because of its low cost and availability in large size [143]. A generic battery model of lead-acid battery is used for dynamic simulation

in which it is composed of a controlled voltage source along with a series resistance ( $R$ ) as shown in Figure 5.2. Here control input  $E$  depends not only on the current but also on the battery state of charge (SOC). The knowledge of the battery characteristics given in manufacturers' data sheet, it is easy to find the values of parameters like  $E_0$  and  $K$ . The battery terminal voltage is given by

$$V_{\text{bat}} = E - Ri \quad (5.1)$$

For discharging:

$$E = E_0 - K \frac{Q}{Q - it} \cdot it - K \frac{Q}{Q - it} \cdot i^* + \exp(t) \quad (5.2)$$

For charging:

$$E = E_0 - K \frac{Q}{Q - it} \cdot it - K \frac{Q}{it - 0.1 \cdot Q} \cdot i^* + \exp(t) \quad (5.3)$$

where,  $R$  is the internal resistance of the battery ( $\Omega$ ),  $E_0$  is the open circuit potential (V),  $i$  is the charging/discharging current of the battery (A),  $Q$  is the battery capacity (Ah),  $i^*$  is the filtered battery current (A),  $it = i \int dt$  is the actual battery charge,  $K$  is the polarization constant (V /Ah).

## 5.1.2 Control Strategies

### I. Analog MPPT Control

The maximum power of the PV module changes with external climate conditions. At any operating condition, there is only one value of current ( $I_{\text{mpp}}$ ) and one value of voltage ( $V_{\text{mpp}}$ ), that defines the maximum power point (MPP) at which power is maximum. The MPPT technique is implemented by using a boost dc-dc converter, as it is required to increase the voltage level at the input of the inverter, across the dc-link capacitor. Figure 5.3 shows the PV system with analog MPPT controller, which consists of a PV module, a boost converter comprising an input filter capacitor  $C$ , an output low-pass filter with inductor  $L$  and capacitor  $C_{\text{dc}}$ , a diode  $D$  and a controllable switch  $S$ , regulated by the MPPT controller.

Denoting  $v$  and  $i$  as the module voltage and current respectively, the power  $p$  will be maximum at  $v = V_{\text{mpp}}$ , where  $dp/dv = 0$  and  $dp/dv > 0$  when  $v < V_{\text{mpp}}$  or  $dp/dv < 0$  when  $v > V_{\text{mpp}}$ . Irrespective of any initial voltage of PV module, the MPPT controller continuously forces the system's state trajectory to move



towards the MPP to satisfy this conditions, which can be described by a simple function,  $\dot{v} = -\gamma(v - V_{\text{mpp}})$ , where  $\gamma$  is a positive number and associated with the dynamic response of the MPPT controller. Larger the value of  $\gamma$ , faster the speed of response. From the above discussion a simple control law can be formulated by taking  $\dot{v} \propto \frac{\partial p}{\partial v} = k \frac{\partial p}{\partial v}$  (where  $k$  is a positive constant). Now redefining the control law as

$$\frac{\partial p}{\partial v} = \text{sign}(\dot{p}/\dot{v}) \equiv \frac{\text{sign}(\dot{p})}{\text{sign}(\dot{v})} \equiv \text{sign}(\dot{p})\text{sign}(\dot{v}) \quad (5.4)$$

$$\text{where } \text{sign}(X) = \begin{cases} +1 & \text{if } X > 0 \\ -1 & \text{if } X \leq 0 \end{cases}$$

Practically it is more convenient to use the boolean 0/1 instead of -1/+1 for representing the sign of value. Thus, comparators are then used for evaluating its sign by producing binary signals. Finally, an XOR gate is used to multiply the two signs, which are now expressed as booleans or binary form. Then the exclusive-ORed output is sampled by S-R flipflop with a clock frequency of  $1/T$  to operate the boost converter at a constant frequency. The brief description of the ASMC-based MPPT technique is already discussed in Chapter-2.

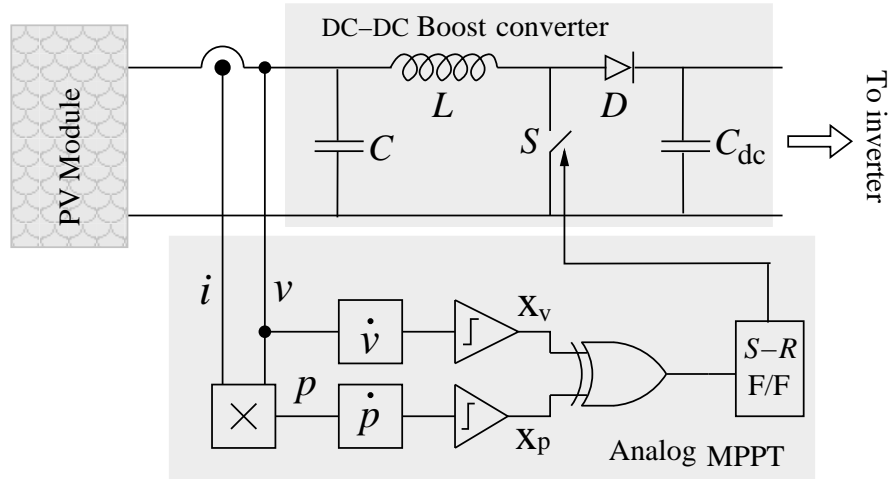


Figure 5.3: PV module with analog MPPT control.

## II. Buck-Boost Converter Control

The lead-acid battery is mainly used to provide a steady power to the local load irrespective of source or load power variation [145]. In the standalone PV system, lead-acid battery operates in two modes, in which it may be charged to store the excess power from the PV source or discharged to supply local load when solar

power is not sufficient. The primary objective battery control is to maintain a stable common dc-link voltage. A bidirectional buck-boost dc-dc converter is used to maintain continuous power flow between the dc-link and BSS with a constant dc-link voltage [146], [145]. A constant dc-link voltage is maintained by charging or discharging the lead-acid battery depending on the load change or solar irradiance change. So no matter the battery is charging or discharging, the dc-link voltage should be stable and regulated throughout the operation. The bidirectional buck-boost converter is controlled in such a way that the dc-link voltage will remain constant or stable during changing in the solar power or load demand.

The battery control scheme includes two loops, internal current control and external voltage control. The inner current loop controls battery current against any parameter variations, and the outer voltage loop regulates the dc-link voltage. When the dc-link voltage ( $V_{dc}$ ) is greater than the reference voltage ( $V_{dcref}$ ), switch  $Q_1$  is activated to operate the circuit as a buck converter (charging mode) and when the dc-link voltage ( $V_{dc}$ ) is lower than the reference voltage ( $V_{dcref}$ ), switch  $Q_2$  is activated to operate the circuit as a boost converter (discharging mode). So the switch  $Q_1$  and  $Q_2$  activates in a complimentary manner (either buck mode or boost mode). The control strategy for the buck-boost converter is shown in Figure 5.4. The voltage  $V_{dc}$  is compared with a reference dc-link voltage  $V_{dcref}$  to get the error signal and this error signal is passed through the PI controller to produce  $i_{batref}$ . Then, the  $i_{batref}$  is compared with the sensed battery current to get the error signal and the error obtained is compensated by the PI controller for getting a control signal as shown in Figure 5.4. The control signal is compared with a high-frequency triangular signal to get the PWM switching pulses.

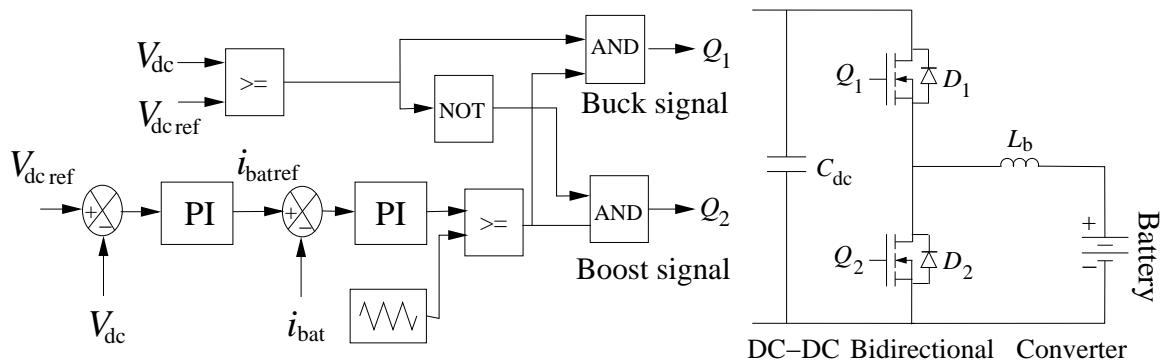


Figure 5.4: Control of bidirectional buck-boost converter.

### III. Inverter Control

In this system the output of the inverter is connected with the local load, producing a pure sinusoidal load voltage. Maintaining good voltage regulation and achieving fast dynamic response under sudden load fluctuation are extremely important in stand-alone PV systems. The two loops (inner inductor current loop and outer output voltage loop) control strategy is adopted for achieving the above power quality issues [147]. The details of this control scheme is already discussed in Chapter-3. The proposed current control technique not only controls

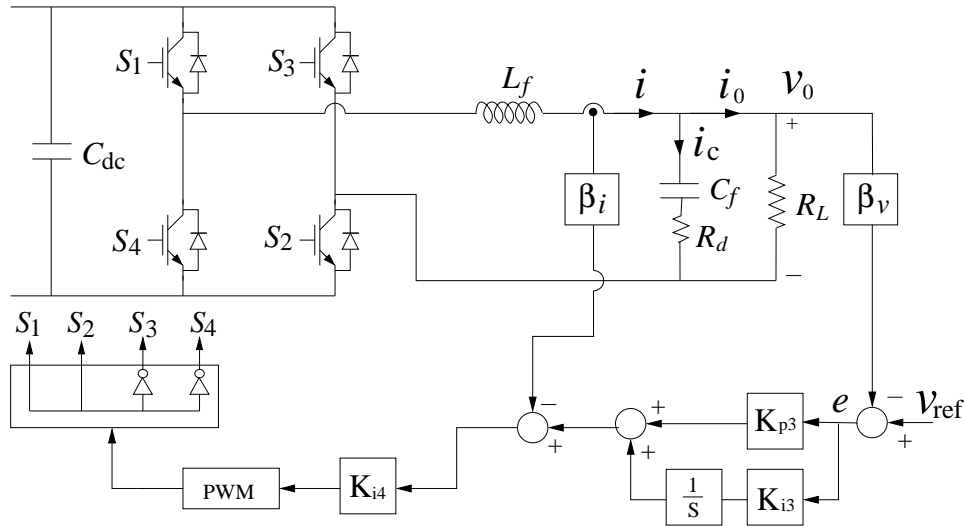


Figure 5.5: Control of 1- $\phi$  inverter.

the inverter output voltage but also improve the dynamic performance of the system under load fluctuations. The details of the inverter control was already discussed in Chater-3.

#### 5.1.3 Small Signal Stability Analysis

The state-space averaging is used to the corresponding time periods of both the subintervals to approximate the converter to the continuous time nonlinear time invariant system. Then, the nonlinear system is linearized about the operating point to get the continuous time linear time invariant system [147]. The transfer functions of the bidirectional buck-boost converter shown in Figure 5.6(a) are given by

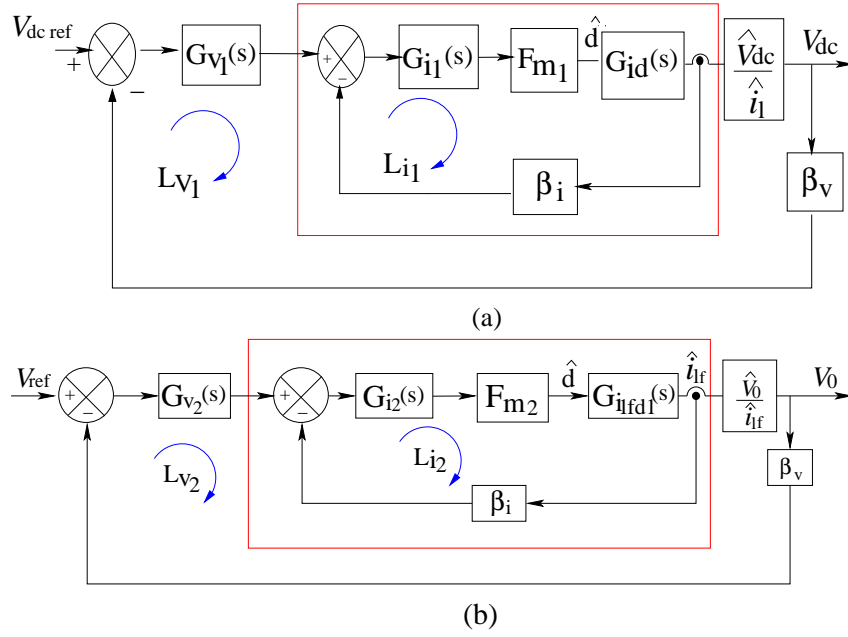


Figure 5.6: Control block diagram: (a) bidirectional buck-boost converter; (b) inverter.

$$\frac{\hat{i}_1(s)}{\hat{d}(s)} = \frac{V_{dc}Z_{dc}C_{dc}s + V_{dc} + D'Z_{dc}i_1}{LC_{dc}Z_{dc}s^2 + Ls + D'^2Z_{dc}} \quad (5.5)$$

$$\frac{\hat{V}_{dc}(s)}{\hat{i}_1(s)} = \frac{Z_{dc}V_{dc}D' - LZ_{dc}i_1s}{V_{dc}Z_{dc}C_{dc}s + V_{dc} + D'Z_{dc}i_1} \quad (5.6)$$

Let  $G_{ild}(s) = \frac{\hat{i}_1(s)}{\hat{d}(s)}$  and transfer functions of the current loop and voltage loop controller are  $G_{i_1}(s) = K_{p1} + \frac{K_{i_1}}{s}$  and  $G_{v_1}(s) = K_{p2} + \frac{K_{i_2}}{s}$  respectively.

The control block diagram shown in Figure 5.6(a),  $F_{m1} = 1$  is the gain of PWM and  $\beta_v = 0.06$ ,  $\beta_i = 0.02$  are the voltage and current sensor gains respectively. Using all the transfer functions, the current loop ( $L_{i1}$ ) gain and voltage loop ( $L_{v1}$ ) gain of the bidirectional buck-boost control system can be found. The stability of both the control loops for the controller tuning parameters are verified by plotting the Bode diagram for current loop and voltage loop. The inner current loop,  $L_{i1}$  has infinite gain margin and phase margin of 89.9 deg (see Figure 5.7(a)). Similarly the outer voltage loop,  $L_{v1}$  has gain margin of 50.3 dB and phase margin of 82.8 deg (see Figure 5.7(b)).

Similarly, the transfer functions for the single phase VSI shown in Figure 5.6(b) are given by

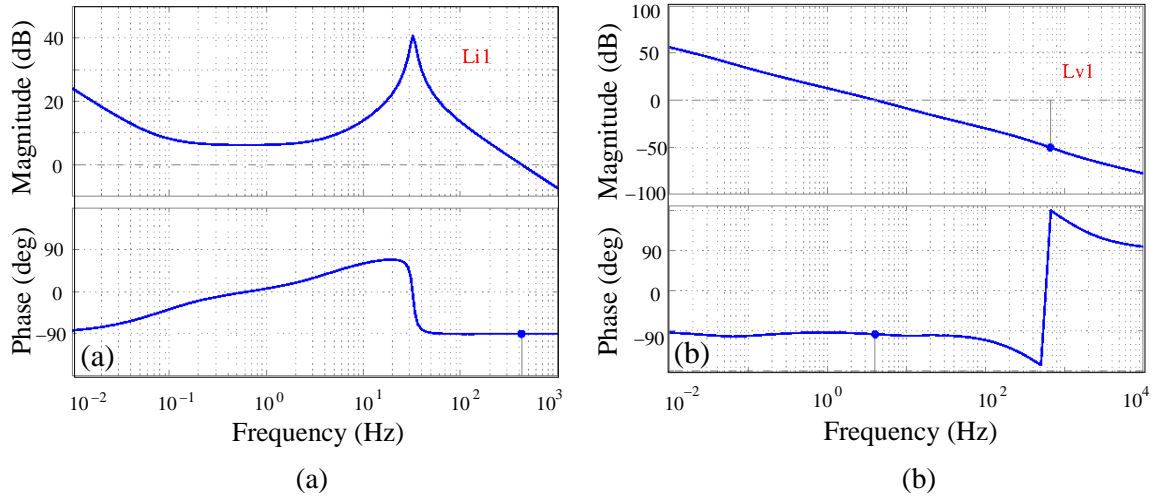


Figure 5.7: Bode diagram: (a) current loop ( $L_{i1}$ ); (b) voltage loop ( $L_{v1}$ ) of buck-boost converter.

$$\frac{\hat{i}_{lf}(s)}{\hat{d}(s)} = \frac{2V_{dc}((R_l + R_d)C_f s + 1)}{(R_l + R_d)C_f L_f s^2 + (L_f + R_l R_d C_f)s + R_l} \quad (5.7)$$

$$\frac{\hat{v}_0(s)}{\hat{i}_{lf}(s)} = \frac{R_l(1 + R_d C_f s)}{1 + (R_l + R_d)C_f s} \quad (5.8)$$

Assuming  $G_{ilfd}(s) = \frac{\hat{i}_{lf}(s)}{\hat{d}(s)}$  and transfer functions of voltage loop and current loop

controller are  $G_{v2} = K_{p3} + \frac{K_{i3}}{s}$  and  $G_{i2} = K_{i4}$  respectively. In the control block diagram,  $F_{m2} = 1$  is the gain of PWM. Similar to buck-boost converter by using all the transfer functions, the current loop ( $L_{i2}$ ) gain and voltage loop ( $L_{v2}$ ) gain can be found. Bode diagram for both the inner current and outer voltage control loops are plotted and found stable for the given controller tuning parameters. The inner current loop,  $L_{i2}$  has gain margin of 6.5 dB and phase margin of 48.9 deg, whereas the outer voltage loop,  $L_{v2}$  has gain margin of 27.5 dB and phase margin of 80.8 deg (see Figure 5.8).

### 5.1.4 Performance Analysis

#### I. Nominal Condition

At nominal condition, let us assume that the power generated by the PV system is equal to the load demand, so that BSS is not supplying or drawing any power. Here, the standalone PV system produces 2 kW of electrical

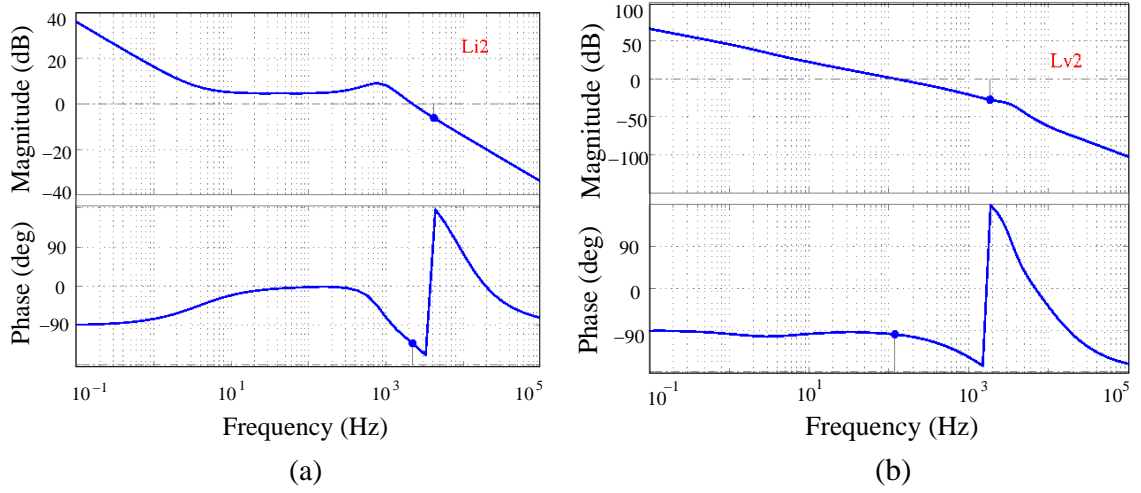
Figure 5.8: Bode diagram: (a) current loop ( $L_{i2}$ ); (b) voltage loop ( $L_{v2}$ ) of inverter.

Table 5.1: Key Parameters for stand-alone mode

Boost, Buck-Boost, Inverter	Controller and PV parameters
$L = 3 \text{ mH}$ , $C = 0.2 \text{ mF}$	$K_{p1} = 0.1$ , $K_{i1} = 0.05$ , $K_{p2} = 0.08$
$L_f = 1.7 \text{ mH}$ , $C_f = 66 \text{ } \mu\text{F}$	$K_{i2} = 512$ , $K_{p3} = 4.2$ , $K_{i3} = 100$
$C_{dc} = 2000 \text{ } \mu\text{F}$ , $L_b = 2 \text{ mH}$	$K_{i4} = 3.8$ , $I_{sc} = 3.8 \text{ A}$ , $V_{oc} = 21.1 \text{ V}$
$V_{dc} = 250 \text{ V}$ , $v_0 = 110 \text{ V(rms)}$	$V_{mpp} = 17.1 \text{ V}$ , and $I_{mpp} = 3.5 \text{ A}$

power at nominal condition and its steady state output voltage ( $v_0$ ) and load current ( $i_0$ ) are shown in Figure 5.9(a) and (b) respectively. The steady state dc-link voltage and its reference voltage is shown in Figure 5.10(a). Its proper tracking shows the effectiveness of the battery controller by using bidirectional dc-dc converter. As BSS is not charging or discharging during this time, so its SOC curve remains constant as shown in Figure 5.10(b).

## II. Load Variation

When load varies, there will be a power mismatch between PV generation and local load, and that power gap can be fulfilled by using the BSS. The Load power demand is varied from 1.6 kW to 2 kW to 2.4 kW. For this load variation, the

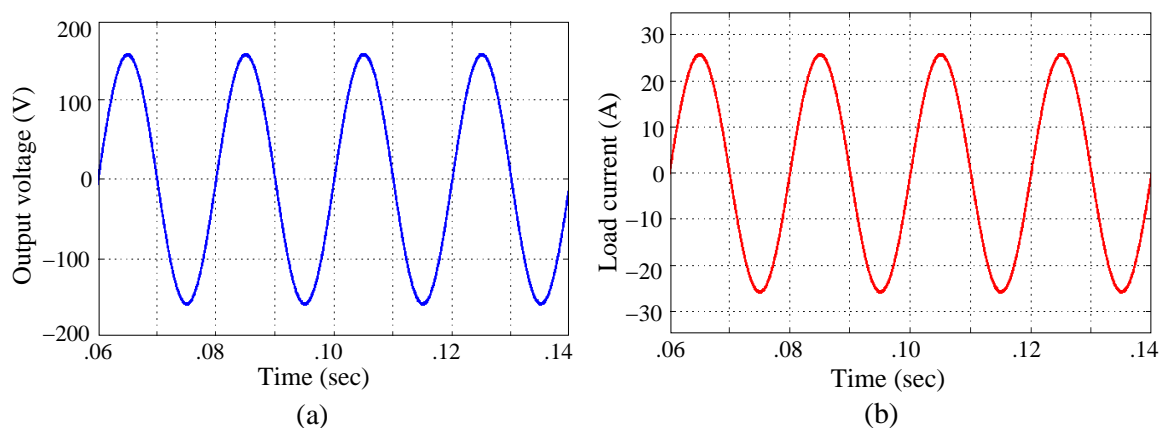


Figure 5.9: Steady state performance. (a) Output voltage  $v_0$ . (b) Load current  $i_0$  of inverter.

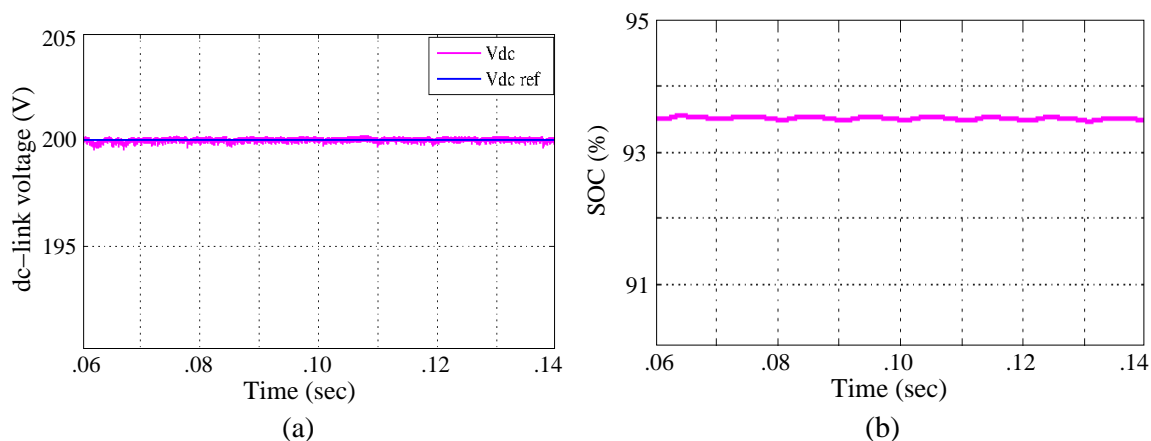


Figure 5.10: Steady state performance at nominal condition. (a) DC-link voltage  $V_{dc}$ . (b) SOC of BSS.

output voltage is shown in Figure 5.11(a), which remains stable and unchanged. This proves the effectiveness of inverter current control technique, which is responsible for maintaining a constant voltage across the load. The load current is shown in Figure 5.11(b) under the same load variation. But this current waveform has a less transient effect that signifies the stability of inverter control loop. From the power curves shown in Figure 5.12(a), it is clear that when PV generation is greater than load power demand, the battery starts charging, and its SOC increases and when load power demand is more than the PV generation, battery discharges to provide the additional power to the load and its SOC starts decreasing. During discharging, battery power is positive and, negative when it is charging. When the load power demand is same as the PV power generation,

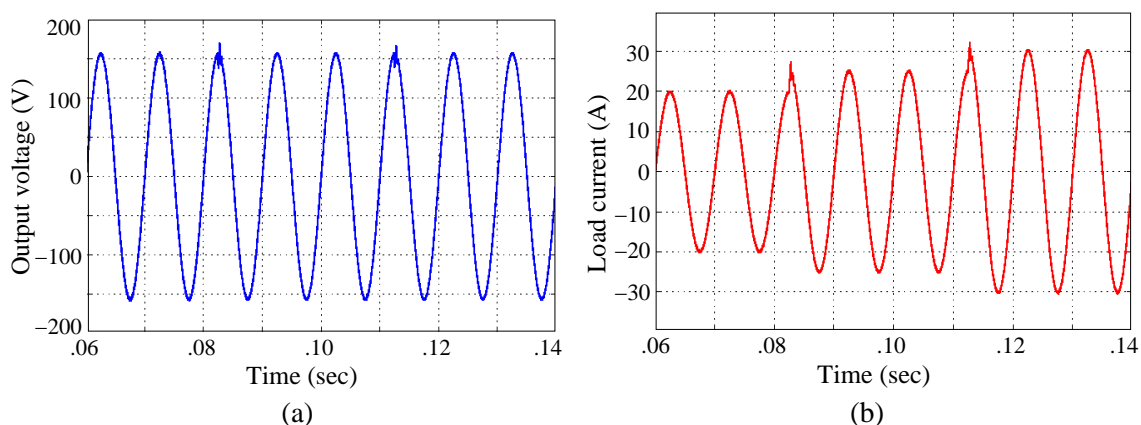


Figure 5.11: Transient performance under load variation. (a) Output voltage  $v_0$ . (b) Load current  $i_0$ .

battery need not to take or supply any power, which keeps its SOC remains constant, shown in Figure 5.12(b).

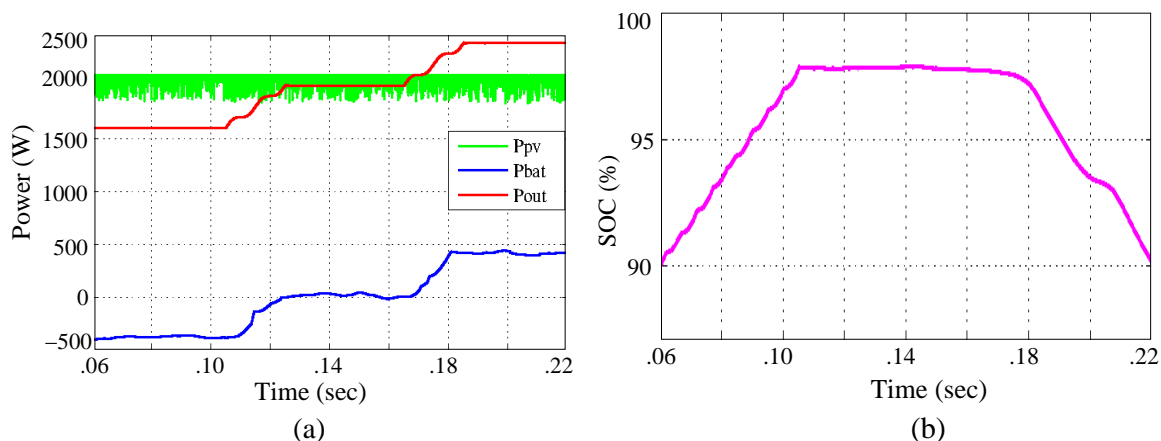


Figure 5.12: Transient performance under load variation. (a) DC-link voltage  $V_{dc}$ . (b) SOC of BSS.

### III. Variation of Solar Irradiance

When PV generation power is not sufficient to supply the load demand, BSS needs to provide the extra power through the discharging process and this condition is called underproduction. When PV generation power is more than the load power demand, the BSS needs to store the excess power through the charging process, and this condition is called overproduction. Solar generated power is varied by varying its irradiance level from  $800 \text{ W/m}^2$  to  $1000 \text{ W/m}^2$  to  $1200 \text{ W/m}^2$ . Figure 5.13(a) and (b) show the output voltage and load



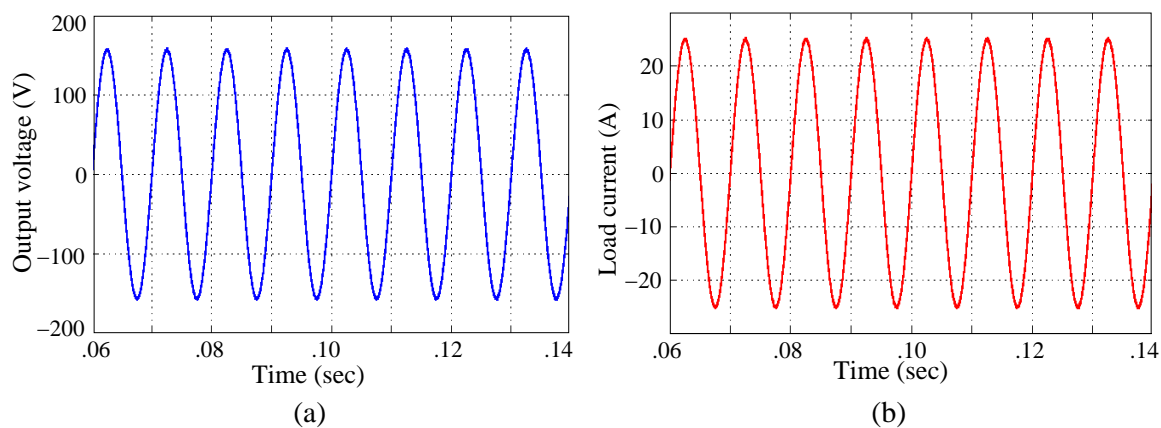


Figure 5.13: Transient performance under solar irradiance variation. (a) Output voltage  $v_o$ . (b) Load current  $i_o$ .

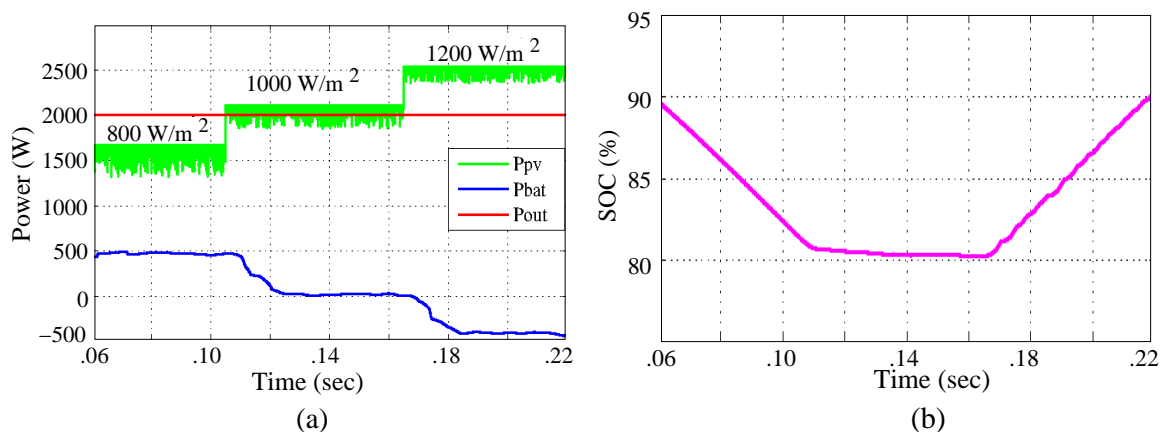


Figure 5.14: Transient performance under solar irradiance variation. (a) DC-link voltage  $V_{dc}$ . (b) SOC of BSS.

current respectively under solar power variation. From the power curves (see Figure 5.14(a)), it is clear that when solar power is less than the output power demand, BSS is providing the extra amount of power through discharging process, and when solar power is greater than the output power demand, BSS is taking the extra amount of power through charging process. The SOC curve shown in Figure 5.14(b), gives the clear idea about battery charging and discharging process.

## 5.2 1- $\phi$ Grid-Connected PV System

### 5.2.1 Two-stage Architecture

In this work, a GPV system with peak power capacity of 2 kW is interfaced with the utility grid through the *LCL* filter. A two-stage topology is introduced for interfacing the PV system and the distribution network. The first stage consists of a non-isolated dc-dc boost converter. This converter is employed to achieve high efficiency and track the maximum power point of each PV panel. The dc-dc boost converter operates in continuous conduction mode (CCM) along its overall operational range. A single-phase full bridge two-level voltage source inverter is the second stage, which is used for transferring power from PV system to the grid. The dc-link capacitor  $C_{dc}$  is used to keep the input voltage of the inverter constant. The dc-link voltage is regulated with a level higher than the peak voltage of the grid in order to ensure the adequate direction of the power flow. The inverter is interfacing with the grid by an inductor  $L_2$ , whereas the high-frequency switching harmonics are suppressed by the *LC* filter of inductance  $L_1$ , and capacitance  $C$ . The GPV system parameters are given in Table 5.2.

### 5.2.2 System Control Description

The schematic control diagram for two-stage single-phase GPV system is shown in Figure 5.15. The main objective of this controller is to improve the dynamic performance of the inverter as well as to achieve low THD grid current  $i_2$ . The proposed controller consists of three loops; an outer dc voltage control loop to regulate the dc-link voltage  $V_{dc}$ , the grid current loop to control the grid current  $i_g$  so that it exactly in phase with the grid voltage, and also used for grid synchronization, and an inner current control loop to improve the dynamic performance of the inverter by sensing the inverter side inductor current  $i_1$ . Here the voltage ( $V_{PV}$ ) and the power ( $P_{PV}$ ) are continuously sensed to calculate the instantaneous power. The MPPT algorithm is based on the sliding mode control to track the maximum PV power. In order to keep power balanced between the PV system and the grid, a dc-link voltage controller is used to keep the voltage constant. The dc-link voltage can be controlled by controlling the current injected into the grid. Suppose the irradiation is increasing, the dc link voltage increases, as the dc-dc converter stage is operating with MPPT. When  $V_{dc}$  is greater than  $V_{dc}^*$ , the dc-link voltage controller output,  $I_d$  increases so

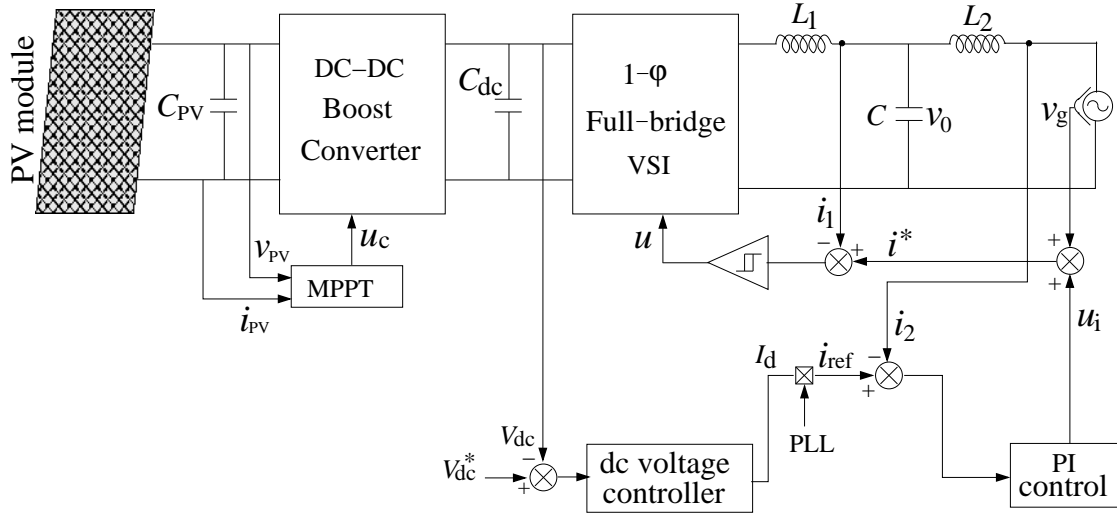


Figure 5.15: Schematic diagram of a two-stage 1- $\phi$  GPV system.

that more current will be injected to the grid. On the other hand, if the irradiation is decreasing, then the current injected to the grid decreases. The outer dc voltage control loop is used for generating the reference for the grid current control loop through the PLL.

The role of the grid current controller is to communicate a low THD current between the inverter to grid and vice-versa even in the presence of the distorted grid voltage and nonlinear local loads of the inverter. A phase lock loop (PLL) is generally used to synchronize the inverter with the grid. The commonly used d-q PLL [132], which collects the grid voltage phase information and produce the reference current  $i_{ref}$  for the grid current loop.

In this work, a fixed frequency hysteretic controller is designed on the basis of SMC, due to its robustness towards the wide parameter variation. The fast inner current loop is used to produce the control signal and then a hysteresis band is employed to generate switching laws for the VSI. The main role of this control loop is to improve the dynamic performance of the inverter.

### 5.2.3 Modeling of 1- $\phi$ GPV System

With the switching functions established, it is possible to write the system equations in terms of the state variable. The schematic diagram of a grid-connected inverter with the  $LCL$  filter is shown in Figure 5.15. The parasitic resistance of the inductor and capacitor are neglected in order to simplify the derivation. A damping resistor  $R_d$  is connected in series with the capacitor to damp out the oscillations occurring due to

resonance. The average model of VSI can be obtained by neglecting the high-frequency component of dc voltage and ac current. Since the switching frequency is much higher than the line frequency, so the switching function  $u$  can be replaced by their equivalent duty cycle  $d$ . So the average model of GCI is given by

$$\frac{di_1}{dt} = -\frac{R_d}{L_1}i_1 + \frac{R_d}{L_1}i_2 - \frac{v_0}{L_1} + \frac{V_{dc}}{L_1}d \quad (5.9)$$

$$\frac{di_2}{dt} = \frac{R_d}{L_2}i_1 - \frac{R_d}{L_2}i_2 + \frac{v_0}{L_2} + \frac{1}{L_2}v_g \quad (5.10)$$

$$\frac{dv_0}{dt} = \frac{1}{C}i_1 - \frac{1}{C}i_2 \quad (5.11)$$

$$\frac{dV_{dc}}{dt} = \frac{i_{bus} - i_{dc}}{C_{dc}} \quad (5.12)$$

where  $d$  is the duty cycle of the inverter. In the steady state, the current ( $i_2$ ) injected to the grid are controlled to be sinusoidal and in phase with the grid voltage  $v_g$ , so that only active power will be fed to the grid. The grid voltage is given by

$$v_g = V_m \cos(\omega t) \quad (5.13)$$

where  $V_m$  and  $\omega$  are the peak voltage and the angular grid frequency. The small signal model is used to predict the presence of the low order harmonics in the output voltage. It is obtained by giving a deliberate perturbation to the average model around the dc operating point as shown in (5.14) and then linearizing it at that point.

$$x = X + \hat{x} \quad (5.14)$$

where  $X$  and  $\hat{x}$  are the dc operating point and the small perturbation, respectively. From (5.9)- (5.11), considering a small perturbation, the small signal model can be represented as

$$\begin{aligned} \dot{\hat{x}} &= -A\hat{x} + Bu + F\delta \\ y &= -Cx + Du \end{aligned} \quad (5.15)$$

where  $\delta = \hat{v}_g$ ,  $\hat{x}$ ,  $u$ ,  $\delta$ , and  $y$  are the grid voltage, the state vectors, inverter control input, and the injected grid current respectively.

The state variables are  $\hat{x} = [\hat{i}_1 \ \hat{i}_2 \ \hat{v}_0]^T$ . The state matrix  $A$ ,  $B$ ,  $C$ ,  $D$ ,  $F$  are given



limit of band-width  $2h$ . It is observed that, turn-on time is the time to keep the upper switch  $S_1$  ON. Turn-on time is also defined as the time taken by the inductor current  $i_1$  to traverse from lower limit to upper limit. Similarly, turn-off time is the time for which the lower switch  $S_2$  ON. The turn-on and turn-off time are calculated from the following (5.17) and (5.18) as

$$\begin{cases} i_{\text{ref}} = I_m \sin(\omega t) \\ i_{\text{lower}} = i_{\text{ref}} - h \\ i_{\text{upper}} = i_{\text{ref}} + h \end{cases} \quad (5.16)$$

$$T_{\text{ON}} = \frac{2hL}{V_{\text{dc}} - V_m} \quad (5.17)$$

$$T_{\text{OFF}} = \frac{2hL}{V_{\text{dc}} + V_m} \quad (5.18)$$

The switching frequency is calculated by using (5.17) and (5.18)

$$f_s = \frac{(V_{\text{dc}})^2 - (V_m)^2}{4LV_{\text{dc}}h} \quad (5.19)$$

It is observed from (5.19), the switching frequency  $f_s$  is variable at the line frequency with the variation of  $i_{\text{lower}}$ ,  $i_{\text{upper}}$ , and  $V_m$ . The inverter side current loop can be designed by considering the small signal model and averaging of the inner current loop. The transfer function  $G_{C_1}(s)$  is

$$G_{C_1}(s) = \frac{i_1(s)}{i_{\text{ref}}(s)} = \frac{G_{i_1}(s)}{\hat{d}(s)} \quad (5.20)$$

where duty ratio  $\hat{d}$  and  $G_{i_1}$  are found from small signal averaging of the single-phase inverter [148], and the final expression given by

$$G_{i_1 d}(s) = \frac{i_1(s)}{\hat{d}(s)} = \frac{v_{\text{dc}}}{R_d} \frac{1 + R_d C s}{L_1 C s^2 + L_1 s / R_d + 1} \quad (5.21)$$

## II. Grid Current Control Loop

The grid current loop is used to achieve high loop gain at the harmonic frequency and improve the stability. This loop ensure the unity power factor at the grid side. As the inner current controller is faster than the grid current controller, so the former is replaced by  $G_{C_1}(s)$  as given in (5.20). Referring the small signal model of the GCI shown in Figure 5.17(a), the transfer function  $\hat{i}_2(s)/\hat{i}_1(s)$  from the reference of the inverter side inner current loop to grid current loop can be expressed by

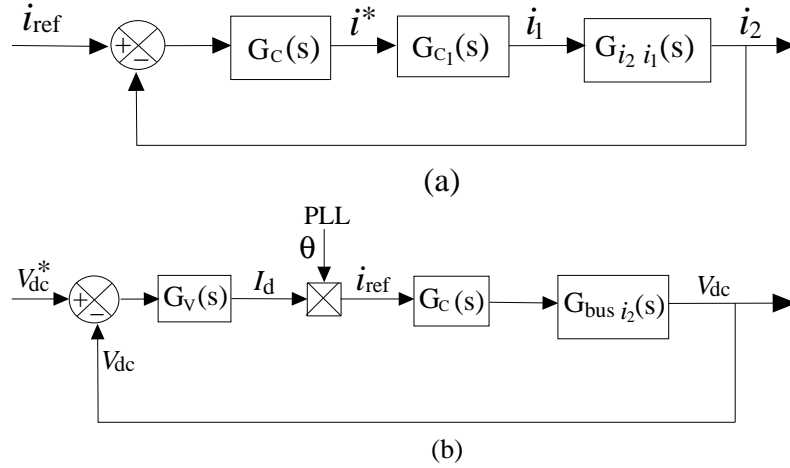


Figure 5.17: (a) Grid current control diagram. (b) DC-link voltage control diagram .

$$G_{i_2 i_1}(s) = \frac{i_2(s)}{i_1(s)} = \frac{R_d C s}{L_2 C s^2 + R_d C s + 1} \quad (5.22)$$

A PI controller is used to increase low frequency gain and reduce the steady-state error between the reference and the actual injected grid current. The transfer function of the PI controller is given by

$$G_{PI}(s) = k_p + \frac{k_i}{s} = \frac{k_p s + k_i}{s} \quad (5.23)$$

The grid current loop has the loop gain and is given by

$$G_{OL_2} = G_{PI}(s) \cdot G_{C1}(s) \cdot G_{i_2 i_1}(s) \quad (5.24)$$

Substituting the values of  $G_{PI}(s)$ ,  $G_{C1}(s)$ , and  $G_{i_2 i_1}(s)$  into (5.24), the grid current loop gain can be found. The controller  $G_{PI}(s)$  is designed, so that the steady state error is reduced. The parameter  $k_p$ , and  $k_i$  are taken as 17 and 1023 respectively. Here, the crossover frequency is found nearly 1 kHz, the amplitude margin is very high, and the phase margin is about 54.7 degree. The gain at 50 Hz is about 50 dB, which means that the disturbance can be attenuated by a factor of 0.06. Obviously, the stability margin is satisfactory and the steady-state error is acceptable.

### III. DC-Link Voltage Control Loop

The dc-link voltage can be regulated at the reference value by the outer voltage control loop, by changing the injected grid current as shown in Figure 5.15. Since all the control loops are cascaded, so that two inner current loops are

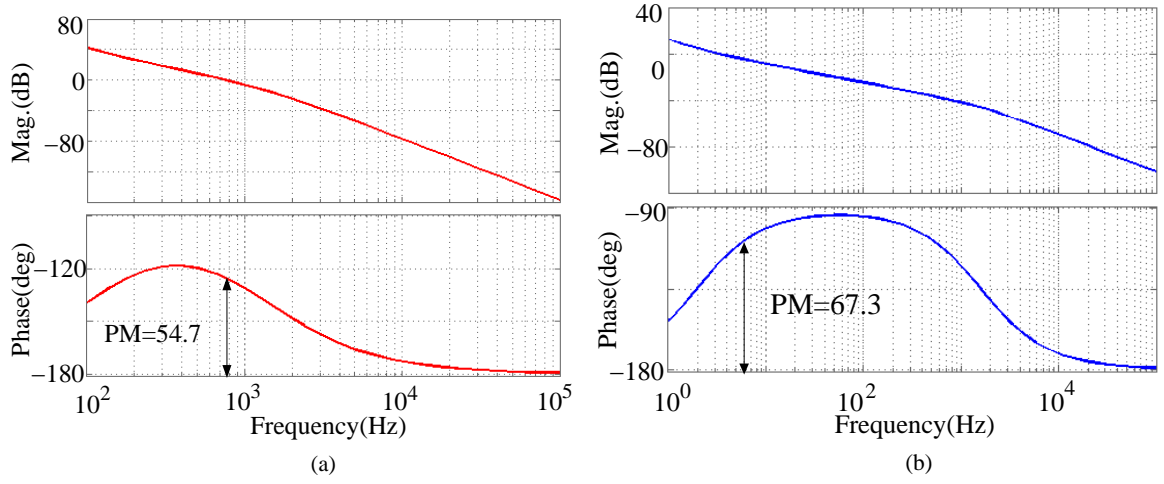


Figure 5.18: Bode plot: (a) current control loop with PI controller; (b) dc-link voltage control loop with PI controller.

assumed as a part of the voltage control loop. The dc-link voltage control loop is reconfigure in Figure 5.17(b). Here the inner current loop and the dc voltage loop are located in the dotted box. The inner current loop has a disturbance term of  $v_g$ , whereas the outer dc voltage loop has the disturbance term of  $i_{bus}$ . In several case, the MPPT control algorithm is comparatively slow, and the grid voltage disturbances are small. On the consequence, these terms are neglected. The transfer function  $G_{dc\ i_2}(s)$ , from the grid current  $i_2$  to the dc-link voltage can be derived from the Figure 5.17(b). In order to conform the stability of the system, the bandwidth of the outer voltage loop should be lower than the inner current loop. Hence, these two control loops are designed independently. The outer dc-link voltage control loop regulates the dc voltage, generated by the PV system and produces the current reference to the injected grid current. A PI controller is used here as the dc voltage regulator. The control parameters are calculated to obtain a phase margin of 67.3 degrees. The parameters:  $k_{pv}$  of 11.2 and  $k_{iv}$  of 723 are found to achieve the above value. The open loop transfer function of the dc-link voltage can be expressed as

$$G_{dcopen}(s) = G_V(s) \cdot G_C(s) \cdot G_{dc\ i_2}(s) \quad (5.25)$$

$$\text{where } G_V(s) = \frac{sk_{pv} + k_{iv}}{s}, \quad \text{and } G_C(s) = \frac{1}{1 + 3st_d} = \frac{1}{1 + 0.001s} \quad [149],$$

$$G_{dc\ i_2}(s) = \frac{\sqrt{3}}{4sC_{dc}}.$$



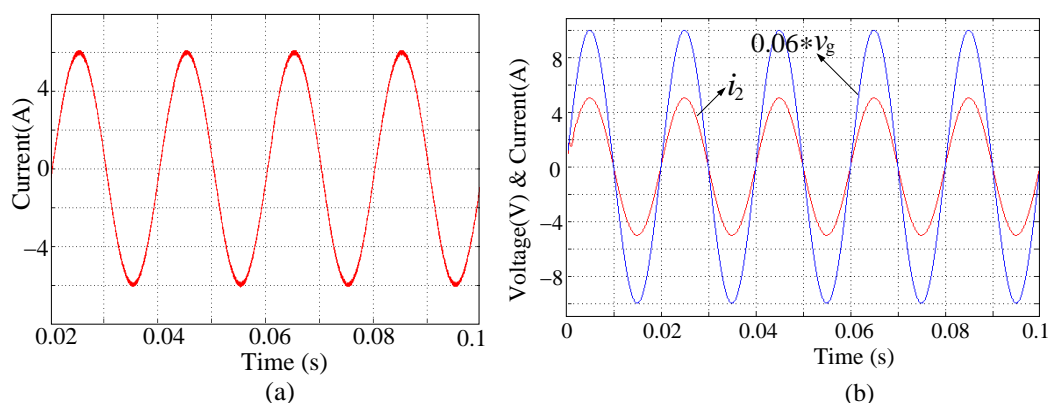


Figure 5.19: Steady-state current waveforms in inverter stage. (a) Inverter side inductor current  $i_1$ . (b) Injected grid current  $i_2$  with grid-voltage.

### 5.2.5 Performance Analysis

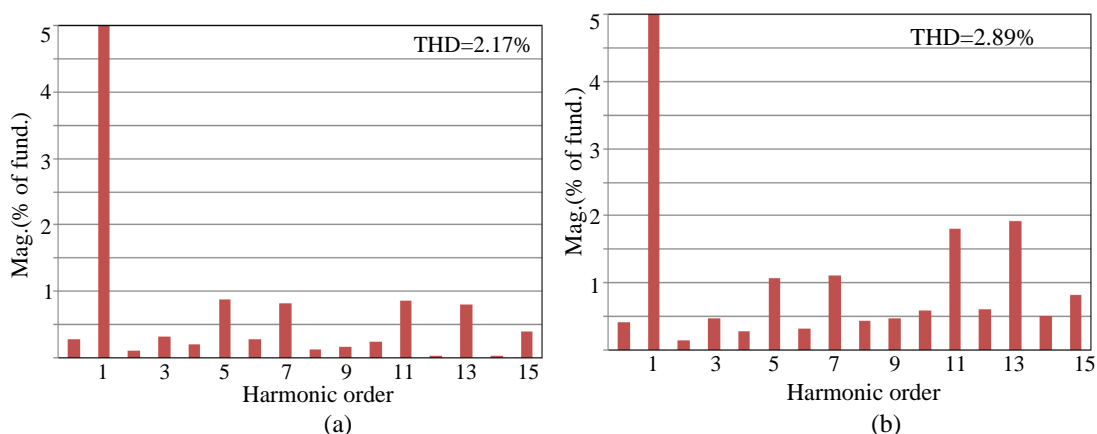


Figure 5.20: % THD of injected grid current  $i_2$  at different power level. (a) Rated output power. (b) 50% of the rated output power.

To demonstrate the effectiveness and applicability of the proposed control strategy, a single-phase two-stage GPV model has been simulated by MATLAB/SIMULINK. The corresponding key parameters used in the simulation is given in table 5.2. The number of PV cells are connected in series-parallel manner to meet the required current and voltage. The PV panel at MPP produces a dc voltage range of 135V to 155V. The second stage comprises of a single-phase voltage source inverter that connects the dc-bus to the grid through a grid interfacing inductor of 1 mH. The nominal dc-bus voltage is 250V and the RMS value of the grid voltage is 110V.

Table 5.2: Key Parameters for grid-connected mode

1- $\phi$ dc-ac Converter	Controller and PV parameters
$L_1 = 0.75$ mH, $C = 100$ $\mu$ F	$K_P = 17$ , $K_I = 1023$
$L_2 = 1.0$ mH, $C_{dc} = 1000$ $\mu$ F	$K_{PV} = 11.2$ , $K_{IV} = 723$
$f_s = 20$ kHz, $v_g = 110$ V(rms)	$I_{sc} = 8.2$ A, $V_{oc} = 45$ V,
$f_o = 50$ Hz, $V_{dc} = 250$ V	$V_{mpp} = 17.1$ V, and $I_{mpp} = 3.5$ A.

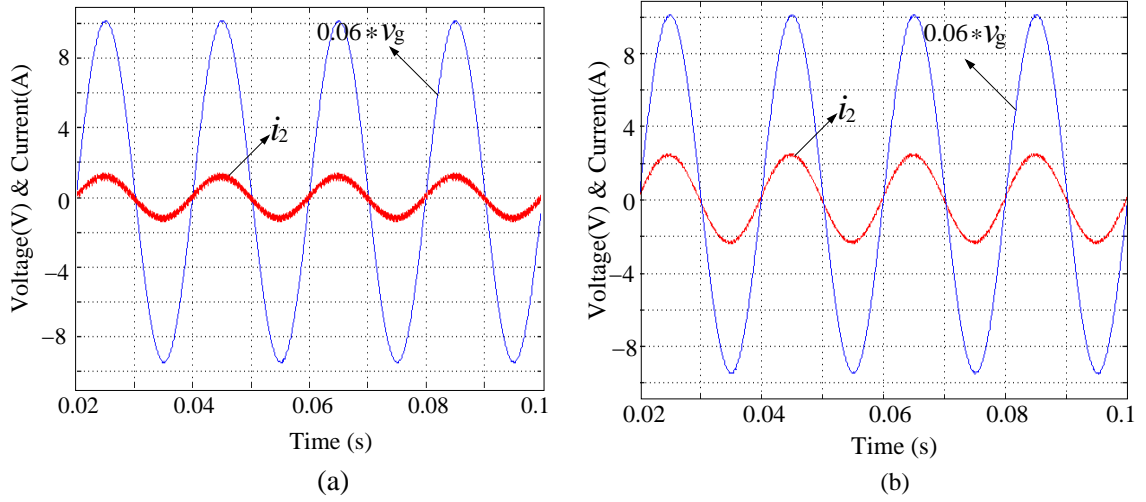


Figure 5.21: Current injected into the grid  $i_2$  at different power level. (a) 25% of the rated output power. (b) 50% of the rated output power.

Figure 5.19(a) shows the inverter side inductor current waveform  $i_1$ , whereas the current  $i_2$  injected to the grid at the steady state is shown in Figure 5.19(b). The above figure reveals that although the inverter side inductor current  $i_1$  has a high ripple, the THD of the injected grid current is less than 2.5%, which meets the IEEE 1547 standards [39]. Moreover the current injected into the grid at different power level with 25% and 50% of rated output power are given in Figure 5.21, and their corresponding THD are shown in Figure 5.20. From the above results, it is observed that even though output power is less than the rated power, still low THD grid current is obtained. But the THD of the grid current at the lower output power is slightly higher than the rated output power. It is due to the relatively high error generated by the measurement of the current sensor at light load. The THD of the grid current can

be minimized by improving the grid current sensing circuit. In all the above cases, the injected grid current is in phase with the grid voltage, so that only active power can be fed to the grid.

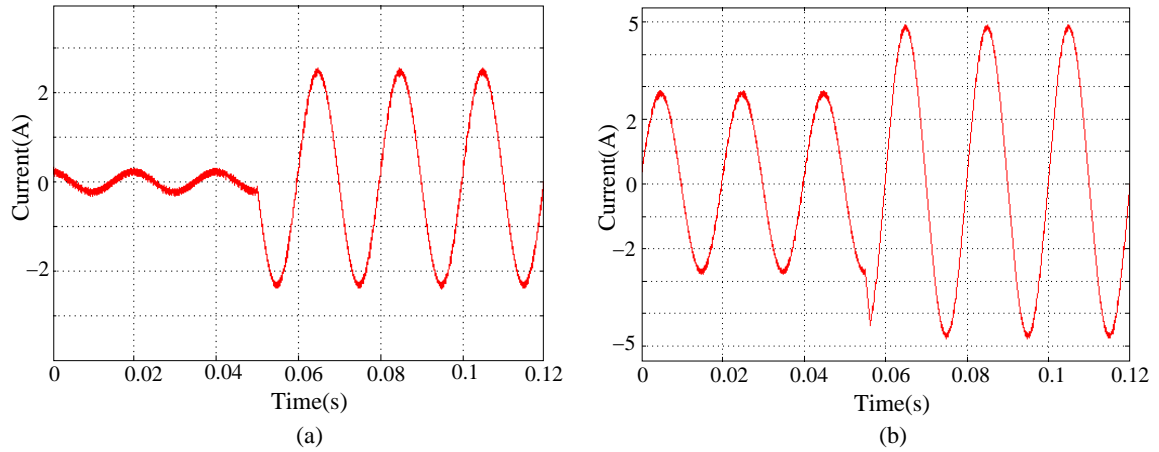


Figure 5.22: Transient response of the GPV system. (a) Step change of 0 to 50% of the rated power. (b) Step change of 50% to 100% of the rated output power.

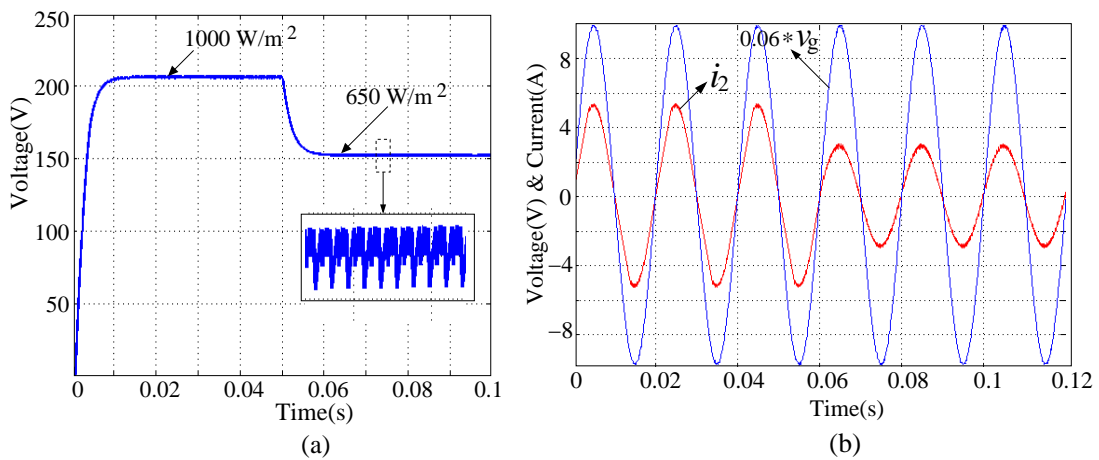


Figure 5.23: Transient performance under solar irradiation change. (a) DC-link voltage. (b) Injected grid current  $i_2$  and grid voltage  $v_g$ .

Now, the performance of the proposed controller is evaluated under the transient conditions. The dynamic performance of the inverter is observed with a step current reference change from 0 to 50% of the rated output power and from 50% to 100% of the rated output power are separately shown in Figure 5.22(a) and (b). From the above two figures, it is revealed that, the current injected into the grid tracks quickly the current reference due to the inner current loop. Now the dynamic performance of

the outer dc voltage loop is evaluated by fluctuating the PV power. Figure 5.23(a) shows the dc-link voltage when connected to the grid. The dc-link voltage controller is used to maintain the constant bus voltage while the sliding mode control based analog MPPT algorithm is active. As shown in Figure 5.23(b), the current injected into the grid is perfectly followed the MPPT, which is tracking the maximum power of the PV panel.

### 5.3 Conclusion

In this chapter, controlling issues of stand-alone and grid-connected operation PV system were discussed. A typical stand-alone PV system comprises of a solar array and a storage device i.e., battery. Lead-acid battery is used in this work to its low cost and availability in large size. The modeling of a lead-acid battery by using the equivalent circuit was discussed. Three independent control loops were used to control the standalone PV system- ASMC based MPPT control for extracting maximum power from PV module, battery control loop for bidirectional power flow between battery and dc-link through buck-boost converter to keep the input dc voltage constant. In addition, inverter control loop was used for maintaining good voltage regulation and achieving fast dynamic response under sudden load fluctuations. Finally, a cascaded controller strategy has been proposed for the two-stage GPV system. It consists of two current loops and a dc-link voltage loop and offers excellent performance in terms of THD for both inverter output voltage and the injected grid current. The dynamic performance of the system is improved by introducing the inner current loop. In order to use the PI regulator of the grid current control in the second loop, a small signal equivalent circuit of single-phase bridge inverter is derived based on the average signal model. Once the design of the two inner current control loops was completed, design of the dc-link controller was addressed for two-stage GPV applications. The controller is designed on the basis of hysteresis current control technique. This strategy can also be used in 3- $\phi$  inverter systems.

# Chapter 6

## Conclusion

### 6.1 Summary of Contributions

PV panels convert solar energy into electric power. Voltage and current at PV terminals have a complicated nonlinear relationship depending on the environment temperature and irradiance. To best regulate the available power from the PV panels, several power electronic technologies have been developed in recent decades. An inverter achieves the dc-ac power processing stage. This inverter must guarantee that it will inject the current into the grid at unit power factor with the lowest harmonic distortion level. Therefore, PV inverters have an enormous impact on the performance of PV grid-tie systems. The different GPV inverter topologies were reviewed. Among all configuration "string-inverter" is suitable, where each string is connected to one inverter and inject power to the grid. Since new strings can be easily added to the system to increase its power rating, system modularity is maximized. Due to its extensive use and the possibility to easily add other power converter stages, this configuration has been chosen as the power conditioning structure considered in this work. In numerous string-inverter topologies, the dual stage inverter structure is selected in this dissertation.

For the first dc-dc stage of the dual-stage inverters, the non-isolated converter topologies are suitable candidates, as no transformer is required. The MPPT is used to control dc-dc converter such that the power extracted from PV panel is maximized. An analog circuitry based PV MPPT technique is therefore an attractive solution due to its low cost and capability of easy integration as compared to the conventional MPPT techniques. A fast and robust analog MPP tracker is proposed without imposing any external control or perturbation. The fast dynamic performances with absolute

robustness are ensured here by integrating the concepts of Utkin's equivalent SMC law and fast-scale stability analysis of actual switched converter systems. Moreover, the superiority of the proposed MPP tracker (in terms of high tracking performances) over classical ones, and its impact in series-connected converters configuration are analytically demonstrated.

For the second dc-ac stage of the dual-stage inverters, the selection of the inverter configuration, with its proper switching technique is necessary to improve power efficiency and power density. The different inverter topologies and switching techniques are reviewed in **Chapter-3**. Among them 1- $\phi$  bridge inverter with bipolar switching technique is found to be suitable one. Moreover, a FFHC controller is proposed to improve the good voltage regulation and the fast dynamic response under sudden load fluctuation. The proposed controller is designed on the basis of SMC technique. The proposed method is then applied to a 1-kVA, 110 V, 50 Hz 1- $\phi$  VSI system. The results show that dynamic response is quite faster than that of the widely used PWM-controlled inverter systems. Moreover, the THD of inverter output voltage is 2.14% at standard nonlinear load IEC62040-3 as well.

In addition, a PV system can be connected to the utility grid, injecting power into the grid besides providing power to their local loads. It is therefore important to inject a low THD current from PV system to grid at unity power factor. This can be achieved by using a PLL, which collects the grid voltage phase information and produce the reference current for the Inverter. Out of the various structure, d-q PLL is suitable for this work. In this dissertation, a cascaded SMC strategy has been proposed for a grid-connected inverter system in order to simultaneously improve the power quality of the local load voltage and the current exchanged with the grid. The proposed controller also enables seamless transfer operation from stand-alone mode to grid-connected mode and vice versa. The control scheme includes an inner voltage loop with a proportional controller and an outer current loop with a PI-controller. This results in a very low THD in both the grid current and the inverter local load voltage simultaneously. The overall controller is designed on the basis of fixed-frequency hysteresis controller. The proposed method is then applied to a 1-kVA, 110 V, 50 Hz grid-connected 1- $\phi$  VSI system. The results show that the steady-state response and the dynamic response are quite attractive.

All the power processing stages discussed in the previous chapters are then combined to form a GPV system. The PV system can either be connected in stand-alone mode or in grid-connected mode. A typical stand-alone PV system comprises of a solar array and a storage device i.e., battery. Whereas in the GPV system, the battery may or may not require. In the former case, a battery is used as

a backup source for power management between the source and the load. Lead-acid battery is used in high power PV applications due to its low cost and availability in large size. The modeling of a lead-acid battery by using the equivalent circuits are discussed here. Three independent control loops are proposed to control the standalone PV system- MPPT control loop for extracting maximum power from PV module, battery control loop for bidirectional power flow between battery and dc-link through buck-boost converter to keep the input dc voltage constant. In addition, inverter control loop is used for maintaining good voltage regulation and achieving fast dynamic response under sudden load fluctuations. Similarly, a cascaded SMC is proposed for GPV system to regulate the current from PV system to the grid at a lower THD level. The stability of the above controllers are verified by using linear stability criterion.

## 6.2 Future Research Directions

The further research might be focused on the following issues.

1. The proposed analog circuitry based MPPT technique was implemented for conventional dc-dc non-isolated converters, which are operated at low duty cycle. This MPPT could be applied for an isolated converter in quasi-resonant mode, which can not only reduce the switching losses but also recycle the leakage energy. Moreover, these converters have the ability to boost a lower dc voltage level to a higher dc-link voltage.
2. For the experimental validation, the current controllers were implemented in dSPACE<sup>TM</sup> which had a time step size limit of 100  $\mu$ s. A relatively smaller time step size device such as FPGA or DSP can be utilized to achieve the control algorithm. So that, current feedback should track the reference more quickly and exactly, and a better performance of harmonic compensation could be expected. This will be essential for analyzing the inner dynamics of the system.
3. The fast scale and the slow scale stability of the proposed SMC controller could be carried out in future.
4. Less steady-state oscillations with reduced cross-coupling effects was found for the series connected buck-type MIC. This could also be verified for the series-connected inverter in future.

# Bibliography

- [1] Y. W. Li, D. M. Vilathgamuwa, and P. C. Loh. A grid-interfacing power quality compensator for three-phase three-wire microgrid applications. *IEEE Trans. Power Electron.*, 21(4):1021–1031, July 2006.
- [2] L. Philipson. Distributed and dispersed generation: addressing the spectrum of consumer needs. In *Proc. IEEE Power Engineering Society Summer Meeting*, volume 3, pages 1663–1665, 2000.
- [3] H. B. Puttgen, P. R. MacGregor, and F. C. Lambert. Distributed generation: Semantic hype or the dawn of a new era? *IEEE Power Energy Mag.*, 1(1):22–29, Jan./Feb. 2003.
- [4] R. H. Lasseter. Microgrids and distributed generation. *Journal of Energy Engineering*, 133(3):144–149, Dec. 2007.
- [5] N. Hatziargyriou, H. Asano, R. Iravani, and C. Marnay. Microgrids. *IEEE Power and Energy Mag.*, 5(4):78–994, Jul./Aug. 2007.
- [6] F. Katiraei, R. Iravani, and N. Hatziargyriou. Microgrids management. *IEEE Power and Energy Mag.*, 6(3):54–65, Jun. 2008.
- [7] B. Kroposki, R. H. Lasseter, T. Ise, S. Morozumi, S. Papathanassiou, and N. Hatziargyriou. Making microgrids work. *IEEE Power and Energy Mag.*, 6(3):41–53, May/June. 2008.
- [8] K. Dang, J. Yu, T. Dang, and B. Han. Benefit of distributed generation on line loss reduction. In *Proc. IEEE ICECE*, volume 2, pages 2042–2045, 2011.
- [9] G. T. Chinery and J. M. Wood. Tva’s photovoltaic activities. *IEEE Trans. Power Appl. Syst.*, 104:1998–2005, Aug. 1985.
- [10] T. Ackermann. *Wind Power in Power Systems*. J. Wiley Press, 2005.
- [11] R. P. O’Hayre, S.W. Cha, W. G. Colella, and F.B. Prinz. *Fuel Cell Fundamentals*. John Wiley & Sons New York, 2009.
- [12] A. K. Saha, S. Chowdhury, S. P. Chowdhury, and P. A. Crossley. Modeling and performance analysis of a microturbine as a distributed energy resource. *IEEE Trans. Energy Convers.*, 24(2):529–538, Mar. 2009.



- 
- [13] J. Bayamba. Photovoltaics: An energy option for sustainable development. In *3rd World Conf. on Photovoltaic Energy Conversion*, pages 174–176, 2003.
- [14] J. M. Carrasco, L. G. Franquelo, J. T. Bialasiewicz, E. Galvan, R. C. P. Guisado, Ma.A.M. Prats, J.I. Leon, and N. Moreno-Alfonso. Power-electronic systems for the grid integration of renewable energy sources: a survey. *IEEE Trans. Ind. Electron.*, 53(4):1002–1016, Jun. 2014.
- [15] P. F. Ribeiro, B. K. Johnson, M. L. Crow, A. Asroy, and Y. Lie. Energy storage systems for advanced power applications. In *Proc. of IEEE*, volume 89, pages 1744–1765, 2001.
- [16] D. Cruz-Martins and R. Demonti. Photovoltaic energy processing for utility connected system. In *27th Annual Conference of the IEEE Industrial Electronics Society*, pages 1292–1296, 2011.
- [17] M. Meinhardt. Past, present and future of grid-connected photovoltaic and hybrid power systems. In *Power Engineering Society Summer Meeting*, volume 2, pages 1283–1288, 2010.
- [18] A. Pregelj, M. Begovic, and A. Rohatgi. Impact of inverter configuration on PV system reliability and energy production. In *Twenty-Ninth IEEE Photovoltaic Specialists Conf.*, 2002.
- [19] IEEE 519 Working Group et al. *IEEE recommended practices and requirements for harmonic control in electrical power systems. IEEE STD*, pages 519–1992, 1992.
- [20] T. S. Basso and R. DeBlasio. *IEEE 1547 series of standards: interconnection issues. IEEE Trans. Power Electron.*, 19(5):1159–1162, 2004.
- [21] R. M. Swanson. A vision for crystalline silicon photovoltaics. In *Progress in Photovoltaics: Research and Applications*, volume 14, pages 443–453, 2006.
- [22] S. B. Kjaer, J. K. Pedersen, and F. Blaabjerg. A review of single-phase grid-connected inverters for photovoltaic modules. *IEEE Trans. Industry Applications*, 41(4):1292–1306, Sep. 2015.
- [23] Q. Li and P. Wolfs. A review of the single phase photovoltaic module integrated converter topologies with three different dc link configurations. *IEEE Trans. Ind. Electron.*, 23(4):1320–1333, May. 2008.
- [24] M. Calais, J. Myrzik, T. Spooner, and V. G. Agelidis. Inverters for single-phase grid-connected photovoltaic systems: an overview. In *Proc. of IEEE PESC*, pages 1995–2000, 2002.
- [25] F. Blaabjerg, Z. Chen, and S. B. Kjaer. Power electronics as efficient interface in dispersed power generation systems. *IEEE Trans. Power Electron.*, 19(5):1884–1194, Sep. 2004.
- [26] H. B. Ertan, E. Dogru, and A. Yilmaz. Comparison of efficiency of two dc-to-ac converters for grid connected solar applications. In *OPTIM, 2012 13th International Conference on*, pages 879–886, 2012.
- [27] M. A. G. de Brito, L. P. Sampaio, L. G. Junior, and C. A. Canesin. Research on photovoltaics: Review, trends and perspectives. In *Power Electronics Conf. (COBEP), 2011 Brazilian*, pages 531–537, 2011.

- 
- [28] J. Schonberger. A single phase multi-string PV inverter with minimal bus capacitance. In *Power Electronics and Applications, 2009. 13th European Conf. on*, pages 1–10, 2009.
- [29] Qian Zhang. *Optimization and design of photovoltaic micro-inverter*. PhD thesis, University of Central Florida Orlando, Florida, 2013.
- [30] H. Hu, S. Harb, N. Kutkut, I. Batarseh, and Z. J. Shen. A review of power decoupling techniques for micro-inverters with three different decoupling capacitor locations in pv systems. *IEEE Trans. Power Electron.*, 28(6):2711–2726, May. 2013.
- [31] H. Haibing, Z. Qian, F. Xiang, Z. J. Shen, and I. Batarseh. A single stage micro-inverter based on a three-port flyback with power decoupling capability. In *Energy Conversion Congress and Exposition (ECCE), 2011*, pages 1411–1416, 2011.
- [32] A. Abramovitz, B. Zhao, and K. M. Smedley. High-gain single-stage boosting inverter for photovoltaic applications. *IEEE Trans. Power Electron.*, 31(5):3550–3558, May. 2016.
- [33] Baifeng Chen, Bin Gu, Jih-Sheng Lai, and Wensong Yu. A high efficiency and reliability single-phase photovoltaic micro-inverter with high magnetics utilization for nonisolated AC-module applications. In *Energy Conversion Congress and Exposition (ECCE), 2013 IEEE*, pages 2406–2411, 2013.
- [34] Lin Chen, A. Amirahmadi, Qian Zhang, N. Kutkut, and I. Batarseh. Design and implementation of three-phase two-stage grid-connected module integrated converter. *IEEE Trans. Power Electron.*, 29(8):3881–3892, Aug. 2014.
- [35] L. F. Costa and R. P. Torrico-Bascope. Stand-alone photovoltaic system with three energy processing stages. In *Power Electronics Conf. (COBEP), 2011 Brazilian*, pages 651–656, 2011.
- [36] J. H. R. Enslin and P. J. M. Heskes. Harmonic interaction between a large number of distributed power inverters and the distribution network. In *Proc. IEEE PESC'03*, pages 1742–1747, 2003.
- [37] J. J. Bzura. The AC module: An overview and update on self-contained modular PV systems. In *Power and Energy Society General Meeting, 2010 IEEE*, page 1–3, 2010.
- [38] G. He, D. Xu, and M. Chen. A Novel Control Strategy of Suppressing DC Current Injection to the Grid for Single-Phase PV Inverter. *IEEE Trans. Power Electron.*, 30(3):1266–1274, Mar. 2015.
- [39] R. H. Bonn. Developing a next generation PV inverter. In *Conf. Rec. 29th IEEE Photovoltaic Specialists Conf.*, pages 1352–1355, 2012.
- [40] Y. Tang, Z. Qin, G. Garcera, F. Blaabjerg, and P. C. Loh. A Dual Voltage Control Strategy for Single-Phase PWM Converters With Power Decoupling Function. *IEEE Trans. Power Electron.*, 30(12):7060–7071, Dec. 2015.
- [41] E. Koutroulis and F. Blaabjerg. Design optimization grid-connected pv inverters including reliability. *IEEE Trans. Power Electron.*, 28(1):325–335, Jan. 2013.

- 
- [42] M. Valentini, A. Raducu, D. Sera, and R. Teodorescu. PV inverter test setup for European efficiency, static and dynamic MPPT efficiency evaluation. In *Optimization of Electrical and Electronic Equipment, 2008. OPTIM 2008. 11th International Conf. on*, pages 433–438, 2008.
- [43] S. Harb and R. S. Balog. Reliability of candidate photovoltaic module-integrated-inverter (pv-mii) topologies: A usage model approach. *IEEE Trans. Power Electron.*, 28(6):3019–3027, Jun. 2013.
- [44] C. Olalla, D. Clement, M. Rodriguez, and D. Maksimovic. Architectures and control of submodule integrated dc–dc converters for photovoltaic applications. *IEEE Trans. Power Electron.*, 28(6):2980–2997, Jun. 2013.
- [45] T. J. Liang and J. H. Lee. Novel high-conversion-ratio high-efficiency isolated bidirectional dc–dc converter. *IEEE Trans. Ind. Electron.*, 62(7):4492–4503, Jul. 2014.
- [46] M. K. Kazimierczuk. *Pulse-width modulated DC-DC power converters*. John Wiley & Sons, 2012.
- [47] M. Kasper, D. Bortis, and J. M. Kolar. Classification and comparative evaluation of pv panelintegrated dcdc converter concepts. *IEEE Trans. Power Electron.*, 29(5):2511–2526, Aug. 2014.
- [48] W. Li and X. He. Review of nonisolated high-step-up dc/dc converters in photovoltaic grid-connected applications. *IEEE Trans. Ind. Electron.*, 58(4):1239–1250, Apr. 2011.
- [49] D. Meneses, F. Blaabjerg, O. Garcia, and J. A. Cobos. Review and comparison of step-up transformerless topologies for photovoltaic ac—module application. *IEEE Trans. Power Electron.*, 28(6):2649–2663, Jun. 2013.
- [50] J. Lee, T. Liang, and J. Chen. Isolated coupled-inductor-integrated dc–dc converter with nondissipative snubber for solar energy applications. *IEEE Trans. Ind. Electron.*, 61(7):1239–1250, Jul. 2014.
- [51] S. V. Araujo, P. Torrico-Bascope, G. V. TorricoBascope, and L. Menezes. Step-up converter with high voltage gain employing three state switching cell and voltage multiplier. In *Proc. Power Electron. Spec. Conf.*, pages 2271–2277, 2008.
- [52] R. marouani, K. Echaieb, and A. Mami. Sliding mode controller for buck-boost dc-dc converter in pv grid-connected system. In *Electrotechnical Conference (MELECON), 2012 16th IEEE Mediterranean*, pages 281–284, Feb. 2012.
- [53] G. R. Walker and P. C. Sernia. Cascaded DC-DC converter connection of photovoltaic modules. *IEEE Trans. Power Electron.*, 19(4):1130–1139, Jul. 2004.
- [54] A. Bidram, A. Davoudi, and R. S. Balog. Control and circuit techniques to mitigate partial shading effects in photovoltaic arrays. *IEEE Journal of Photovoltaic*, 2(4):532–546, Oct. 2012.

- 
- [55] R. C. N. Pilawa-Podgurski and D. J. Perreault. Submodule integrated distributed maximum power point tracking for solar photovoltaic applications. *IEEE Trans. Power Electron.*, 28(6):2957–2967, Jun. 2013.
- [56] F. Wang, X. Wu, F. C. Lee, Z. Wang, P. Kong, and F. Zhuo. Analysis of unified output MPPT control in sub-panel PV converter system. *IEEE Trans. Power Electron.*, 29(3):1275–1284, Mar. 2014.
- [57] M. S. Agamy, M. H. Todorovic, A. Elasser, S. Chi, R. L. Steigerwald, J. A. Sabale, A. J. McCann, Li Zang, and F. Mueller. An efficient partial power processing DC/DC converter for distributed PV architectures. *IEEE Trans. Power Electron.*, 29(12):674–686, Feb. 2014.
- [58] M. A. G. Brito, L. Galotto, Jr., L. P. Sampaio, G. A. Melo, and C. A. Canesin. Evaluation of the main MPPT techniques for photovoltaic applications. *IEEE Trans. Ind. Electron.*, 60(3):1156–1167, Mar 2013.
- [59] N. Femia, G. Petrone, G. Spagnuolo, and M. Vitelli. A technique for improving P&O MPPT performances of double-stage grid-connected photovoltaic systems. *IEEE Trans. Ind. Electron.*, 56(11):4473–4482, Nov. 2009.
- [60] P. E. Kakosimos, A. G. Kladas, and S. N. Manias. Fast photovoltaic system voltage or current oriented MPPT employing a predictive digital current-controlled converter. *IEEE Trans. Ind. Electron.*, 60(12):5673–5685, Dec. 2013.
- [61] C. W. Chen, K. H. Chen, and Y. M. Chen. Modeling and controller design of an autonomous PV module for DMPPT PV systems. *IEEE Trans. Power Electron.*, 29(9):4723–4732, Sep. 2014.
- [62] S. Maity and Y. Suraj. A fixed frequency dual-mode dc-dc buck converter with fast-transient response and high efficiency over a wide load range. in *Proc. Applied Power Electronics Conf. and Exposition APEC*, pages 415–420, 2013.
- [63] S. Maity and Y. Suraj. Analysis and modeling of a FFHC-controlled dc-dc buck converter suitable for wide range of operating conditions. *IEEE Trans. Power Electron.*, 27(12):4914–4924, Dec. 2012.
- [64] M. Bradley, E. Alarcón, and O. Feely. Design-oriented analysis of quantization-induced limit cycles in a multiple-sampled digitally controlled buck converter. *IEEE Trans. Circuits and Syst. I*, 61(4):1192–12–5, Apr. 2014.
- [65] R. P. Venturini, V. V. R. Scarpa, G. Spiazzi, and S. Buso. Analysis of limit cycle oscillations in maximum power point tracking algorithms. *Power Electronics Spec. Conf.*, pages 15–19, Jun. 2008.
- [66] N. Femia, G. Petrone, G. Spagnuolo, and M. Vitelli. Optimization of perturb and observe maximum power point tracking method. *IEEE Trans. Power Electron.*, 20(4):963–973, Jul. 2005.

- 
- [67] V. V. R. Scarpa, S. Buso, and G. Spiazzi. Low complexity MPPT technique exploiting the PV module MPP locus characterization. *IEEE Trans. Ind. Electron.*, 56(5):1531–1538, May 2009.
- [68] Y. Levron and D. Shmilovitz. Maximum power point tracking employing sliding mode control. *IEEE Trans. Circuits and Syst. I*, 60(3):724–732, Mar. 2013.
- [69] E. Mamarelis, G. Petrone, and G. Spagnuolo. An hybrid digital-analog sliding mode controller for photovoltaic applications. *IEEE Trans. Ind. Electron.*, 9(2):1094–1103, May 2013.
- [70] E. Bianconi, J. Calvente, R. Giral, E. Mamarelis, G. Petrone, C. A. Ramos-Paja, G. Spagnuolo, and M. Vitelli. A fast current-based MPPT technique employing sliding mode control. *IEEE Trans. Ind. Electron.*, 60(3):1168–1178, Mar. 2013.
- [71] E. Mamarelis, G. Petrone, and G. Spagnuolo. Design of a sliding mode controlled SEPIC for PV MPPT applications. *IEEE Trans. Ind. Electron.*, 99, Oct. 2013.
- [72] M. di. Bernardo, C. J. Budd, A. R. Champneys, and P. Kowalczyk. *Piecewise-smooth Dynamical Systems: Theory and Applications*. Applied Mathematical Sciences: Springer, 2008.
- [73] J. C. Alexander and T. I. Seidman. Sliding modes in intersecting switching surfaces II: Hysteresis. *Houston Journ. of Math.*, 25(1):185–211, 1999.
- [74] S. K. Mazumder, A. H. Nayfeh, and D. Boroyevich. Theoretical and experimental investigation of the fast-scale and slow-scale instabilities of a dc-dc converter. *IEEE Trans. Power Electron.*, 16(2):201–216, 2001.
- [75] R. Khanna, Q. Zhang, W. E Stanchina, G. F. Reed, and Z. H. Mao. Maximum power point tracking using model reference adaptive control. *IEEE Trans. Power Electron.*, 29(3):1490–1499, Mar. 2014.
- [76] J. M. Carrasco, L. G. Franquelo, J. T. Bialasiewicz, E. Gaalvan, R. C. P. Guisado, M. A. M. Prats, J. I. Leon, and N. Moreno-Alfonso. Power electronics systems for the grid integration of renewable energy sources:A survey. *IEEE Trans. Power Electron.*, 53(4):1002–1016, 2006.
- [77] J. Huusari and T. Suntio. Origin of cross-coupling effects in distributed dc-dc converters in photovoltaic applications. *IEEE Trans. Power Electron.*, 28(10):4625–4635, Oct. 2013.
- [78] N. Femia, G. Lisi, G. Petrone, G. Spagnuolo, and M. Vitelli. Distributed maximum power point tracking of photovoltaic arrays: Novel approach and system analysis. *IEEE Trans. Ind. Electron.*, 55(7):2610–2621, Jul. 2008.
- [79] G. Petrone, C. A. Ramos-Paja, G. Spagnuolo, and M. Vitelli. Granular control of photovoltaic arrays by means of a multi-output maximum power point tracking algorithm. *Prog. Photovolt. Res. Appl.*, 21(5):918–923, 2013.
- [80] N. Femia, M. Fortunato, G. Lisi, G. Petrone, G. Spagnuolo, and M. Vitelli. Guidelines for the optimization of P&O technique for grid-connected double-stage potovoltaic systems. In *Proc. IEEE Int. Symp. Ind. Electron., Vigo, Spain*, pages 2420–2425, Jun. 2007.

- 
- [81] K. Ogata. *Morden control engineering*. Prentice Hall, 2010.
- [82] J. J. Negroni, D. Biel, F. Guinjoan, and C. Meza. Energy-balance and sliding mode control strategies of a cascade h-bridge multilevel converter for grid-connected pv systems. In *Proc. IEEE ICIT.*, pages 1155–1160, March 2010.
- [83] Y. H. Lim and D. C. Hamill. Simple maximum power point tracker for photovoltaic arrays. *Electronics Letters*, 36:997–999, May 2000.
- [84] S. Maity. Dynamics and stability issues of a discretized sliding-mode controlled dc-dc buck converter governed by fixed-event-time switching. *IEEE Trans. Circuits and Syst. I*, 60(6):1657–1669, Jun. 2013.
- [85] E. J. Brea, A. S. Llinas, E. O. Rivera, and J. G. Llorente. A maximum power point tracker implementation for potovoltaic cells using dynamic optimal voltage tracking. In *Proc. 25th Annu. IEEE APEC*, pages 2161–2165, Feb. 2010.
- [86] D. Giaouris, S. Maity, S. Banerjee, V. Pickert, and B. Zahawi. Application of Filippov method for the analysis of subharmonic instability in dc-dc converters. *Int. Journ. of Circuit Theory and Applications*, 37(8):899–919, 2009.
- [87] B. H. Cho, J. R. Lee, and F. C. Y. Lee. Large-signal stability analysis of spacecraft power processing systems. *IEEE Trans. Power Electron.*, 5(1):110–116, Jan. 1990.
- [88] R. Alonso, E. Román, A. Sanz, V. E. M. Santos, and P. Ibáñez. Analysis on inverter-voltage influence on distributed MPPT architecture performance. *IEEE Trans. Ind. Electron.*, 59(10):3900–3906, Oct. 2012.
- [89] A. Safari and S. Mekhilef. Simulation and hardware implementation of incremental conductance MPPT with direct control method using cuk converter. *IEEE Trans. Ind. Electron.*, 58(4):1154–1161, Apr. 2011.
- [90] Y. Jiang, J. A. A. Qahouq, and T. A. Haskew. Adaptive step size with adaptive-perturbation-frequency digital MPPT controller for a single-sensor photovoltaic solar system. *IEEE Trans. Power Electron.*, 28(7):3195–3205, July 2013.
- [91] T. Esum, J. W. Kimball, P. T. Krein, P. L. Chapman, and P. Midya. Dynamic maximum power point tracking of photovoltaic arrays using ripple correlation control. *IEEE Trans. Power Electron.*, 21(5):1282–1291, September 2006.
- [92] F. Zhang, K. Thanapalan, A. Procter, S. Carr, and J. Maddy. Adaptive hybrid maximum power point tracking method for a photovoltaic system. *IEEE Trans. Energy Convers.*, 28(3):353–360, Jun. 2013.
- [93] T. Esum and P. L. Chapman. Comparison of photovoltaic array maximum power point tracking techniques. *IEEE Trans. Energy Convers.*, 22(2):439–449, June 2007.

- 
- [94] M. Matsui, M. Nagai, M. Mochizuki, and A. Nabae. High-frequency link dc/ac converter with suppressed voltage clamp circuits-naturally commutated phase angle control with self turn-off devices. *IEEE Trans. Industry Applications*, 32(2):293–300, Mar. 1996.
- [95] S. M. S. H. Rafin, T. A. Lipo, and B. i. Kwon. Performance analysis of the three transistor voltage source inverter using different pwm techniques. In *Power Electronics and ECCE Asia (ICPE-ECCE Asia), 2015 9th International Conference on*, pages 1428–1433, Jun. 2015.
- [96] J. Holtz. Pulsewidth modulation survey. *IEEE Trans. Ind. Electron.*, 39(5):410–420, Dec. 1992.
- [97] H.W. van der Broeck, H. C. Skudelny, and G.V. Stanke. Analysis and realization of a pulsewidth modulator based on voltage space vectors. *IEEE Trans. Industry Applications*, 24(1):142–150, Jan. 1988.
- [98] P. N. Enjeti, P. D. Ziogas, and J. F. Lindsay. Programmed pwm techniques to eliminate harmonics: A critical evaluation. *IEEE Trans. Industry Applications*, 26(2):302–316, Mar. 1990.
- [99] A. I. Maswood and et. al. A Flexible Way to Generate PWMSHE Switching Pattern using Genetic Algorithm. In *IEEE Applied Power Electronics (APEC) Conf. Proc., Anaheim, California, USA*, pages 1130–1134, 2001.
- [100] A. Sayyah and et. al. Optimization of THD and Suppressing Certain Order Harmonics in PWM Inverters using Genetic Algorithms. In *Proc. of IEEE International Symposium on Intelligent Control, Germany*, pages 874–879, 2006.
- [101] K. Sundareswaran and et. al. Inverter harmonic elimination through a colony of continuously exploring ants. *IEEE Trans. Ind. Electron.*, 54(5):2558–2565, Oct. 2007.
- [102] A. Kavousi and et. al. Application of the Bee algorithm for selective harmonic elimination strategy in multilevel inverters. *IEEE Trans. Power Electron.*, 27(4):1689–1696, Apr. 2012.
- [103] Mohamed Azab. Global maximum power point tracking for partially shaded pv arrays using particle swarm optimization. *International Journal of Renewable Energy Technology*, 11(2):211–235, Apr. 2009.
- [104] J. Hereford and M. Siebold. A multi-robot search using a physically embedded particle swarm optimization. *International Journal of Computational Intelligence Research*, 4(2):197–204, Apr. 2008.
- [105] R. J. Wai, W. H. Wang, and C. Y. Lin. High-performance stand-alone photovoltaic generation system. *IEEE Trans. Ind. Electron.*, 55(1):240–250, Jan. 2008.
- [106] U. Borup, P. N. Enjeti, and F. Blaabjerg. A new space-vector-based control method for ups systems powering nonlinear and unbalanced loads. *IEEE Trans. Industry Applications*, 37(6):1864–1870, Nov. 2001.

- 
- [107] D. Noriega-Pineda, G. Espinosa-Perez, A. Varela-Vega, and S. HortaMejia. Experimental evaluation of an adaptive nonlinear controller for single-phase UPS. In *Proc. IEEE International Conf. on Control Appl. (CCA'01), Mexico, Sept.*, pages 254–258, 2001.
- [108] J. C. Liao and S. N. Yeh. A novel instantaneous power control strategy and analytic model for integrated rectifier/inverter systems. *IEEE Trans. Power Electron.*, 15(6):996–1006, Nov. 2000.
- [109] N. Abdel-Rahim and J. E. Quaicoe. Analysis and design of a multiple feedback loop control strategy for single-phase voltage-source ups inverters. *IEEE Trans. Power Electron.*, 11(4):532–541, Jul. 1996.
- [110] F. Blaabjerg, R. Teodorescu, M. Liserre, and A. V. Timbus. Overview of control and grid synchronization for distributed power generation systems. *IEEE Trans. Ind. Electron.*, 53(5):1398–1409, Jul. 2014.
- [111] D. Sera, T. Kerekes, M. Lungeanu, R. Teodorescu, G.K. Andersen, and M. Liserre. Low-cost digital implementation of proportional-resonant current controllers for PV inverter applications using delta operator. In *31st Annual Conf. of IEEE Industrial Electronics Society, IECON*, Nov., pages 6–11, 2005.
- [112] A. Hasanzadeh, O. C. Onar, H. Mokhtari, and A. Khaligh. A proportional-resonant controller-based wireless control strategy with a reduced number of sensors for parallel-operated ups. *IEEE Trans. Power Delivery*, 25(1):468–478, Jan. 2010.
- [113] A. Timbus, M. Liserre, R. Teodorescu, P. Rodriguez, and F. Blaabjerg. Evaluation of current controllers for distributed power generation systems. *IEEE Trans. Power Electron.*, 24(3):654–664, Mar. 2009.
- [114] T. Kawabata, T. Miyashita, and Y. Yamamoto. Digital control of three-phase pwm inverter with lc filter. *IEEE Trans. Power Electron.*, 6(1):62–72, Jan. 1991.
- [115] Y. A. R. I. Mohamed and E. F. ElSaadany. A control scheme for pwm voltage-source distributed-generation inverters for fast load-voltage regulation and effective mitigation of unbalanced voltage disturbances. *IEEE Trans. Ind. Electron.*, 55(5):2072–2084, May 2008.
- [116] P. C. Loh and D. G. Holmes. Analysis of multiloop control strategies for *LC*, *CL*, and *LCL*-filtered voltage-source and current source inverter. *IEEE Trans. Industry Applications*, 41(2):644–654, Mar. 2005.
- [117] Qin Lei, Shuitao Yang, and F.Z. Peng. High-performance and cost-effective multiple feedback control strategy for standalone operation of grid-connected inverter. In *25th Annual IEEE Applied Power Electronics Conference and Exposition, APEC'10*, pages 854–860, 2010.
- [118] W. Guo, S. Duan, Y. Kang, and J. Chen. A new digital multiple feedback control strategy for single-phase voltage-source PWM inverters. In *Proc. IEEE International Conf. on Electrical and Electronic Technology (TENCON'01), Singapore*, pages 809–813, 2001.



- 
- [119] V. I. Utkin. Variable structure systems with sliding modes. *IEEE Transactions on Automatic Control*, 22(2):212–222, Apr. 1977.
- [120] M. Carpita and M. Marchesoni. Experimental study of a power conditioning using sliding mode control. *IEEE Trans. Power Electron.*, 11(5):731–742, 1996.
- [121] L. Malesani, L. Rossetto, G. Spiazzi, and A. Zuccato. An ac power supply with sliding-mode control. *IEEE Ind. Appl. Mag.*, pages 32–38, 1996.
- [122] J. F. Silva and S. S. Paulo. Fixed frequency sliding modulator for current mode pwm inverters. In *Proc. Power Electron. Spec. Conf. (PESC)*, pages 623–629, 1993.
- [123] S. Buso, S. Fasolo, and P. Mattavelli. Uninterruptible power supply multi-loop control employing digital predictive voltage and current regulators. *IEEE Trans. Industry Applications*, 37(6):1846–1854, Nov. 2001.
- [124] R. O. Caceres and I. Barbi. A boost dc-ac converter:analysis,design and experimentation. *IEEE Trans. Power Electron.*, 14(1):134–141, Jan.. 1999.
- [125] Praveen Mediseti. *Real Time Simulation and Hardware-in-loop Testing of a hybrid Electric Vehicle Control System*. PhD thesis, The University of Akron, 2007.
- [126] H. Komurcugil. Rotating-line-based sliding-mode control for single-phase UPS inverters . *iee*, 59(10):3719–3726, Oct 2014.
- [127] Z. Yao, L. Xiao, and Y. Yan. Seamless transfer of single-phase grid-interactive inverters between grid-connected and stand-alone modes. *IEEE Trans. Power Electron.*, 25(6):1597–1603, Jun. 2010.
- [128] K. H. Ahmed, S. J. Finney, and B. W. William. Passive filter design for three-phase inverter interfacing in distributed generation. In *Compatibility in power Electronics, CPE'07*, pages 1–9, 2007.
- [129] M. Liserre, F. Blaabjerg, and S. Hansen. Design and control of an *LCL*-filter-based three-phase active rectifier. *IEEE Trans. Industry Applications*, 41(6):1281–1291, Oct. 2005.
- [130] J. Bauer. Single-phase voltage source inverter photovoltaic application. *Acta Polytechnica*, 50(4):7–11, Oct. 2010.
- [131] J. Guerrero, J. Vasquez, J. Matas, M. Castilla, and L. Vicuna. Control strategy for flexible microgrid based on parallel line-interactive ups systems. *IEEE Trans. Ind. Electron.*, 56(3):726–736, Mar. 2009.
- [132] T. Vu Tran, T. Chun, H. Lee, H. Kim, and E. Nho. Pll-based seamless transfer control between grid-connected and islanding modes in grid-connected inverters. *IEEE Trans. Power Electron.*, 29(10):5218–5228, Oct 2014.
- [133] Q. C. Zhong and G. Weiss. Robust droop controller for accurate proportional load sharing among inverters operated in parallel. *IEEE Trans. Ind. Electron.*, 60(4):1281–1290, Apr 2013.

- 
- [134] M. Prodanovic and T. Green. High-quality power generation through distributed control of a power park microgrid. *IEEE Trans. Ind. Electron.*, 53(5):1471–1482, Oct. 2006.
- [135] G. Weiss, Q. C. Zhong, T. Green, and J. Liang. H repetitive control of dc-ac converters in microgrids. *IEEE Trans. Power Electron.*, 19(1):219–230, Apr 2004.
- [136] T. Hornik and Q.-C. Zhong. H repetitive voltage control of grid-connected inverters with frequency adaptive mechanism. In *Proc. IET Power Electron.*, pages 925–935, 2010.
- [137] J. Dannehl, C. Wessels, and F. W. Fuchs. Limitations of voltage-oriented pi current control of grid-connected pwm rectifiers with lcl filters. *IEEE Trans. Ind. Electron.*, 56(2):380–388, Feb. 20013.
- [138] D. N. Zmood and D. G. Holmes. Stationary frame current regulation of pwm inverters with zero steady-state error. *IEEE Trans. Power Electron.*, 18(3):815–822, May 2003.
- [139] K. Zhang, Y. Kang, J. Xiong, and J. Chen. Deadbeat control of pwm inverter with repetitive disturbance prediction. In *Proc. IEEE 14th annu. Power Electron. Conf. and expo. (APEC)*, pages 1028–1031, Mar. 2009.
- [140] P. Mattavelli and F. P. Marafao. Repetitive-based control for selective harmonic compensation in active power filters. *IEEE Trans. Ind. Electron.*, 51(5):1018–1024, Oct. 2004.
- [141] F. Fuchs, J. Dannehl, and F. W. Fuchs. Discrete sliding mode current control of grid-connected three-phase pwm converters with lcl filter. *IEEE Trans. Ind. Electron.*, 18(3):784–792, May 2003.
- [142] C. Bao, X. Ruan, X. Wang, W. Li, D. Pan, and K. Weng. Step-by-step controller design for lcl-type grid-connected inverter with capacitor–current–feedback active-damping. *IEEE Trans. Power Electron.*, 29(3):1239–1253, Mar. 2014.
- [143] J.B. Copetti and F. Chenlo. A general battery model for pv system simulation. *Journal of Power Sources*, 47:109–118, 1994.
- [144] O. Tremblay and L.-A. Dessaint. Experimental validation of a battery dynamic model for ev applications. *World Electric Vehicle Journal*, 3:2032–6653, 2009.
- [145] N. S. Jayalakshmi, D. N. Gaonkar, A. Balan, P. Patil, and S. A. Raza. Dynamic modeling and performance study of a stand-alone photovoltaic system with battery supplying dynamic load. *International Journal of Renewable Energy Research*, 4(3):635–640, May. 2014.
- [146] H. R. Karshenas, H. Daneshpajoo, A. Safaei, P. Jain, and A. Bakhshai. Bidirectional dc-dc converters for energy storage systems. In *Energy Storage in the Emerging Era of Smart Grids*, pages 161–177, 2015.
- [147] D. V. de la Fuente, C. L. T Rodriguez, G. Garcera, E. Figueres, and R.O. Gonzalez. Photovoltaic power system with battery backup with grid-connection and islanded operation capabilities. *IEEE Trans. Ind. Electron.*, 60(4):1571–1581, Apr. 2013.

- [148] T. Suntio, J. Lempien, K. Hynynen, and P. Silventoinen. Modeling and analysis of hysteretic current mode control inverter. In *Proc. IEEE APEC, Dallas USA*, pages 395–401, 2004.
- [149] Remus Teodorescu, Marco Liserre, and Pedro Rodriguez. *Grid converters for photovoltaic and wind power systems*. John Wiley & Sons, 2011.

# Dissemination

## Journal

1. S.Maity and Pradeep Kumar Sahu,"Modeling and Analysis of a Fast and Robust Module-Integrated Analog Photovoltaic MPP Tracker", in IEEE Transactions on Power Electronics, vol. 31, no. 1, pp. 280-291, Jan. 2016.
2. Pradeep Kumar Sahu and S.Maity, "Power Quality Improvement of a Grid-Connected PV System by Fixed Frequency Sliding Mode Control," in IEEE Transactions on Power Electronics. (Submitted)

## Conference

1. P. Shaw, Pradeep Kumar Sahu and S. Maity, "Modeling and Control of a Battery Connected Standalone Photovoltaic System", IEEE 1st International Conference on Power Electronics, Intelligent Control and Energy Systems (ICPEICES-2016), at DTU, New Delhi, INDIA, 4-6 Jul. 2016.
2. Pradeep Kumar Sahu and S. Maity, "Modeling and Control of Grid-Connected DC/AC Converters for Single-Phase Micro-inverter Application." In 2015 Annual IEEE India Conference (INDICON) (pp. 1-6). IEEE.
3. Pradeep Kumar Sahu, P. Shaw, and S. Maity, "Power Quality Improvement of a Grid-Connected Inverter By Fixed Frequency Sliding Mode Control." (INDICON). In 2015 Annual IEEE India Conference (INDICON). IEEE
4. Pradeep Kumar Sahu and S. Maity, "Dynamic performance enhancement of voltage source inverter by constant-frequency hysteretic current controller." In Technology Symposium (TechSym), 2014 IEEE, pp. 193-198, Kharagpur, India.(**Best paper awarded**)
5. Pradeep Kumar Sahu, S. Maity, and R. K. Mahakhuda, "A fixed switching frequency sliding mode control for single-phase voltage source inverter," in Circuit, Power and Computing Technologies (ICCPCT), 2014, pp. 1006-1010, India.

# CURRICULUM VITAE

**PRADEEP KUMAR SAHU**

*pksahu.nitrkl@gmail.com,*

*pksahu.3020@gmail.com,*

Mobile No. – +91-9437423474

Address:

At - Phase-4,

Po - Dumduma,

Bhubaneswar-751019.



## CAREER OBJECTIVE

I aim to find interesting research opportunities with specific application to areas in which my contributions will make a difference to the quality of life of real people.

## PERSONAL DETAILS

- ◇ *Date of Birth* – - 10/06/1977
- ◇ *Father's Name* – Late Dr. Deenabandhu Sahu
- ◇ *Nationality* – Indian
- ◇ *Marital Status* – Married
- ◇ *Languages Known* – English, Hindi, Odia